UNIVERSITY OF CALIFORNIA,

IRVINE

Hippocampal Circuit Connectivity Alterations in Alzheimer's Disease Model Mice

DISSERTATION

submitted in partial satisfaction of the requirements

for the degree of

DOCTOR OF PHILOSOPHY

in Biomedical Engineering

by

Qiao Ye

Dissertation Committee:

Professor Xiangmin Xu, Chair

Professor Zoran Nenadic

Professor Kim Green

2024

DEDICATION

To

my grandparents,

my parents,

my fiancé,

and

all my family and friends

in recognition of their unwavering love, encouragement, and support

Per aspera ad astra

TABLE OF CONTENTS

Page

LIST OF FIGURES

Page

LIST OF TABLES

Page

ACKNOWLEDGEMENTS

First and foremost, I would like to express my sincerest gratitude to my advisor, Dr. Xiangmin Xu. It has been an extraordinary experience working with you. Your steadfast support, insightful guidance, and unwavering encouragement have been crucial to completing my PhD journey. I am truly thankful for the vast platform provided for me to explore the neuroscience field. Having profound vision, dedication to scientific research, and extraordinary work ethic, you have always been a role model for me!

I would like to extend my heartfelt thanks to the professors I worked with during this journey. Thank my dissertation and advancement committee members, Dr. Zoran Nenadic, Dr. Kim Green, Dr. Douglas Nitz, and Dr. Qing Nie. Your constructive feedback and valuable suggestions have been crucial in shaping this work. I am sincerely thankful to Dr. Nitz, for your guidance in spatial learning and memory behavior experiments. I would like to also express my deep gratitude to Dr. Todd Holmes, for your generously helping improve my scientific writing skills and bringing insights to my research. Thank Dr. Zhaoxia Yu for your guidance on statistical analysis. Thank Dr. Zhongping Chen for your help on the optical imaging. Thank Dr. Orkide Koyuncu for your help with the virus study. Thank Dr. Bogdan Bintu for your generous help with the ongoing spatial transcriptomic study.

I am also deeply appreciative of my lab members and colleagues. The support and encouragement from everyone in the big Xu lab family and the CNCM center have made the journey enjoyable. I would like to thank Dr. Zhiqun Tan for your patient guidance on AD project and spatial transcriptomic project. Thank Dr. Liqi Tong for your insightful discussion. Thank Dr. Yanjun Sun for your inspiring advice, generous help and encouragement. Thank Dr. Steven Greico for teaching me techniques, and your fun and stimulating discussions. Thank Dr. Hai Zhang for your help with the in vivo imaging experiments and for teaching me many smart techniques. Thank Dr. Eric Velasquez for your help with electrophysiology experiments, mouse colony, and many insightful ideas. Thank Dr. Alexis Bouin and Ms. Michele Wu for your kind help in virus production. Thank Dr. Carlos Rodriguez for your help with the AD project. Thank Dr. Xin Qiao for your help with electrophysiology experiments. Thank Dr. Kevin Johnston for your help with imaging data analysis. Thank Dr. Geng Pan for your insightful discussion on the tracing project. Thank Dr. Sujan Das for your help with the spatial transcriptomic project.

I would also like to thank my graduate student lab mates and peers. Thank Dr. Xiaoxiao Lin for being extremely supportive and teaching me all the experimental techniques, and I'm so grateful for your steadfast encouragement. Thank Dr. Lujia Chen for your help with MATLAB analysis and for patiently teaching me coding. Thank Ms. Pan Gao for your generous help with the tracing project and for teaching me whole-brain imaging techniques. Thank Mr. Wenhao Cao for the interesting and inspiring discussions on my projects. Thank Mr. Bereket Berackey for your help with coding. Thank Mr. Max Garduño for the discussion on AD projects. Thank Mr. Mingyu Du for the interesting discussions. Thank our lab manager Ms. Ginny Wu for teaching me rabies virus production, and for always being super supportive. Thank Ms. Pei Tan for the help with the spatial transcriptomic project. I would like to extend my special gratitude to Ms. Gocylen Gast and Ms. Xilin Su, and all the undergraduate students I have worked closely with on my PhD projects. This work would not been possible without your help. Thank Ms. Jingyi Wang from Dr. Zhongping Chen's lab for your help and collaboration with the two-photon imaging project. Thank Ms. Mahsa Nafisi and Mr. Samuel Park from Bintu lab for your generous help with the spatial transcriptomic project. Thank all the other Xu lab members and colleagues for your support.

I am grateful to my friends in Irvine and other places in the world, your friendship and support have been invaluable to me. Thank Dr. Yuntian Xue and Dr. Haoxin Zhang for your encouragement and for making my life in Irvine more colorful. Thank Dr. Zhehao Cheng and Dr. Xu Zhang for your encouragement.

Finally, I owe my deepest gratitude to my family. To my parents, Mr. Zhaohui Ye and Ms. Xiaohua Xu, your endless love, patience, and sacrifices have made this journey possible. Thank you for always encouraging me and giving me confidence. To my fiancé, Dr. Xuance Jiang, thank you for being there through the highs and lows, and for always believing and encouraging me, and I am forever grateful for your presence in my life.

Chapter 1 and Chapter 4 of this dissertation are adopted from a manuscript in preparation.

Chapter 2 is a reprint of the material as it appears in "Hippocampal neural circuit connectivity alterations in an Alzheimer's disease mouse model revealed by monosynaptic rabies virus tracing" in Neurobiology of Disease, used with permission from Elsevier, Inc. (CC BY 4.0). Qiao Ye performed viral tracing experiments. Qiao Ye, Gocylen Gast, and Xilin Su performed histology studies and data quantification. Qiao Ye, Todd C. Holmes, and Xiangmin Xu analyzed and interpreted data. Qiao Ye, Todd C. Holmes, and Xiangmin Xu wrote the manuscript with help and input from other authors. Xiangmin Xu directed and supervised research which forms the basis for the dissertation.

Chapter 3 is a reprint of the material as it appears in "Monosynaptic rabies tracing reveals sex and age-dependent dorsal subiculum connectivity alterations in an Alzheimer's disease mouse model" in Journal of Neuroscience, used with permission from the Society for Neuroscience (CC BY 4.0). Qiao Ye and Xiangmin Xu designed research; Qiao Ye, Gocylen Gast, Erik George Wilfley, Hahn Huynh, and Chelsea Hays performed research; Qiao Ye, Todd C. Holmes, and Xiangmin Xu analyzed data; Qiao Ye, Todd C. Holmes, and Xiangmin Xu wrote the paper. Xiangmin Xu directed and supervised research which forms the basis for the dissertation.

This work was supported by National Institutes of Health grants RF1AG065675, RF1MH120020, and S10MH124715 to X.X.. Todd C. Holmes is funded by R35 GM127102.

VITA

Qiao Ye

EDUCATION

2018 B.S. in Biological Sciences, Southern University of Science and Technology, China

Honors: *Summa Cum Laude*

2024 Ph.D. in Biomedical Engineering, University of California, Irvine, United States

FIELD OF STUDY

Alzheimer's Disease

Circuit Mapping

Rabies Virus Tracing

PUBLICATIONS

W Cao, Z Tan, B Berackey, J Nguyen, S Brown, B Lin, **Q Ye**, M Seiler, TC Holmes, X Xu*. An AAV capsid proposed as microglia-targeting directs genetic expression in forebrain excitatory Neurons. ***Under review***, 2024.

E Velazquez-Rivera, O Dey, NS Kim, W Cao, **Q Ye**, H Zhang, JT Ting, TC Holmes, B Ren, X Xu*. Specific targeting of brain endothelial cells using enhancer-AAV vectors. ***Under review***, 2024.

Q Ye, G Gast, TC Holmes, X Xu*. A circuit focus on neural mechanisms in Alzheimer's disease mouse models using new viral mapping tools. ***In preparation***, 2024.

J Wang, **Q Ye**, L Chou, S Qiu, X Xu, Z Chen*. Miniaturized head-mount Doppler optical coherence tomography scope for freely moving mouse. ***ACS Photonics,*** 2024. https://doi.org/10.1021/acsphotonics.4c00856

Q Ye, G Gast, E Wilfley, H Huynh, C Hays, TC Holmes, X Xu*. Monosynaptic rabies tracing reveals sex and age-dependent dorsal subiculum connectivity alterations in an Alzheimer's disease mouse model. ***Journal of Neuroscience***, 2024. https://doi.org/10.1523/JNEUROSCI.1796-23.2024

A Bouin, G Wu, OO Koyuncu, **Q Ye**, KY Kim, MY Wu, L Tong, L Chen, S Phan, MR Mackey, R Ramachandra, MH Ellisman, TC Holmes, BL Semler, X Xu*. New rabies viral resources for multi-scale neural circuit mapping. ***Mol Psychiatry***, 2024. https://10.1038/s41380-024-02451-6

L Chen, X Lin, **Q Ye**, Z Nenadic, TC Holmes, DA Nitz, X Xu*. Anatomical organization of temporally correlated neural calcium activity in the hippocampal CA1 region. ***iScience***, 2023. https://doi.org/10.1016/j.isci.2023.106 703

Q Ye, G Gast, X Su, T Saito, T Saido, TC Holmes, X Xu*. Hippocampal neural circuit connectivity alterations in an Alzheimer's disease mouse model revealed by monosynaptic rabies virus tracing. ***Neurobiology of Disease***, 2022 (cover article). https://doi.org/10.1016/j.nbd.2022.105820

X Lin, L Chen, D Baglietto-Vargas, P Kamalipour, **Q Ye**, F LaFerla, DA Nitz, TC Holmes, X Xu*. Spatial coding defects of hippocampal neural ensemble calcium activities in the 3xTg-AD Alzheimer's disease mouse model. ***Neurobiology of Disease***, 2022 (cover article). https://doi.org/10.1016/j.nbd.2021.105562

CONFERENCE PROCEEDING AND POSTER PRESENTATIONS

Q Ye, G Gast, E Wilfley, H Huynh, C Hays, TC Holmes, X Xu*. Monosynaptic rabies tracing reveals subiculum connectivity alterations in Alzheimer's Disease. ***International Association of Biomedical Sciences Forum***, Irvine, 2023.

Q Ye, G Gast, E Wilfley, H Huynh, C Hays, TC Holmes, X Xu*. Monosynaptic Rabies Tracing Reveals Subiculum Connectivity Alterations in Alzheimer's Disease. ***Society for Neuroscience***, Washington D.C., 2023.

G Wu, A Bouin, OO Koyuncu, **Q Ye**, KY Kim, J H.C. Nguyen, MY Wu, L Tong, L Chen, S Phan, MR Mackey, R Ramachandra, MH Ellisman, TC Holmes, BL Semler, X Xu*. ***Society for Neuroscience***, Washington D.C., 2023

Q Ye, G Gast, E Wilfley, H Huynh, C Hays, TC Holmes, X Xu*. Monosynaptic Rabies Tracing Reveals Subiculum Connectivity Alterations in Alzheimer's Disease. ***14th Annual REMIND Emerging Scientists Symposium***, University of California Irvine, 2023.

Q Ye, G Gast, E Wilfley, H Huynh, C Hays, TC Holmes, X Xu*. Monosynaptic Rabies Tracing Reveals Subiculum Connectivity Alterations in Alzheimer's Disease. ***Center for Neural Circuit Mapping Conference***, University of California Irvine, 2023.

Q Ye, G Gast, X Su, T Saito, T Saido, TC Holmes, X Xu*. Hippocampal neural circuit connectivity alterations in an Alzheimer's Disease mouse model revealed by monosynaptic rabies virus tracing. ***Society for Neuroscience***, San Diego, 2022.

Q Ye, G Gast, X Su, T Saito, T Saido, TC Holmes, X Xu*. Hippocampal neural circuit connectivity alterations in an Alzheimer's Disease mouse model revealed by monosynaptic rabies virus tracing. ***13th Annual REMIND Emerging Scientists Symposium***, University of California Irvine, 2022.

Q Ye, G Gast, E Wilfley, H Huynh, C Hays, TC Holmes, X Xu*. Hippocampal neural circuit connectivity alterations in an Alzheimer's Disease mouse model revealed by monosynaptic rabies virus tracing. ***Center for Neural Circuit Mapping Conference***, University of California Irvine, 2022.

ABSTRACT OF THE DISSERTATION

Hippocampal Circuit Connectivity Alterations in Alzheimer's Disease Model Mice

by

Qiao Ye

Doctor of Philosophy in Biomedical Engineering

University of California, Irvine, 2024

Professor Xiangmin Xu, Chair

Alzheimer's disease (AD) is a progressive neurodegenerative disorder with a growing major health impact, particularly in countries with aging populations. Traditional therapeutic approaches have been taken towards treating AD by focusing on neurochemical and neuropathological mechanisms. The examination of neural circuit mechanisms in AD mouse models is a recent focus for identifying new AD treatment strategies. Accumulating evidence shows that there are neural circuit-level maladaptive alterations in AD brains. New viral-genetic technologies facilitate quantitative mapping of cell-type-specific neural circuit connections in AD mouse models. Monosynaptic rabies virus mapping reveals age-progressive changes in both long-range and local hippocampal neural circuit connections that occur in AD mouse models – and provides neural circuit-based explanations for human AD behavioral defects. The recent developments in concepts and technology present new opportunities for studying AD pathogenesis at the neural circuit level. In Chapter 1, I provide a literature overview of new technical advancements in neural circuit mapping, describe both conventional neural tracers and state-of-the-art virus-based tracers, and discuss relevant applications using the novel viral-genetic tracers. In Chapter 2, I report our investigation of neural circuit connectivity alterations of hippocampal CA1 excitatory neurons in AD model mice. I focus on the hippocampus as it is one of the most affected brain regions in AD. I applied genetically targeted monosynaptic rabies viral

tracing to map the neural circuit connectivity of CA1 excitatory neurons in age-matched APP-KI model mice versus wild-type (WT) control mice. Our quantitative analysis of neural circuit connections reveals that compared to WT mice, APP-KI mice show age-progressive and sex-dependent hippocampal CA1 connectivity alterations. Unexpectedly, AD mice exhibit CA1 excitatory neuron input shift with hippocampal CA3 in AD mice. Moreover, aged female AD mice show significantly reduced subiculum to CA1 projections. This study is the first to characterize hippocampal CA1 neural circuit changes in AD model mice using monosynaptic rabies viral tracing. In Chapter 3, I report our study of using monosynaptic rabies virus to map the neural circuit connectivity of the subiculum excitatory neurons in age-matched, gender-balanced control and 5xFAD mice. The subiculum is a critical brain region for relaying and integrating hippocampal and cortical information, and is among the most vulnerable brain regions in AD. My study shows that the neural connectivity of the subiculum exhibits a significant sex- and age-dependent differential pattern in the 5xFAD mice. I find an unexpected increase in visual cortex input connectivity to the subiculum in aged 5xFAD mice. Our new findings are supported by human AD literature and can help to identify potential new therapeutic circuit targets for AD treatments. Overall, the studies presented in this dissertation provide new insights into neural circuit mechanisms underlying AD pathogenesis and support the notion that neural circuit disruptions are a prominent feature of AD.

INTRODUCTION

Alzheimer's disease (AD) is a common and severe neurodegenerative disease. In the United States alone, AD is projected to affect 14 million people in the next 25 years (Matthews et al., 2019). AD develops in an age-dependent fashion, silently over decades before the cognitive symptoms appear in advanced stages. Since Dr. Alois Alzheimer's initial description, extensive effort has been dedicated to unraveling AD pathogenesis and the search for potential treatments. The pathological hallmarks of AD include amyloid-beta (Aβ) deposition and neurofibrillary tangles of tau protein. For the past 40 years, AD research has primarily focused on these pathological features, including the appearance of protein aggregates composed of Aβ and tau, and the loss of cholinergic neurons in AD. This is based on the idea that if the pathological features are treated, the disease process will be ameliorated. Despite intensive drug development efforts guided by these observations, treatments targeting Aβ formation and cholinergic signaling have been disappointing. We still have no cures for AD, and we have no effective drugs that alleviate cognitive impairments found in AD patients. These failures suggest that we need to look for other disease mechanisms and new treatment options.

Recent studies show a promising new avenue for understanding AD: alterations in neural circuit connectivity in AD. The mammalian central nervous system is a vast network of interconnected regions that coordinate brain activity to carry out different functions. We can consider three levels of brain circuit connections: global-scale, mesoscale, and local/micro-scales. While it has been long known that brain atrophy may occur in AD patients, increasing evidence shows that the brain circuits are impacted by AD at all three levels. Interestingly, studies from human patients and AD mouse models indicate that circuit disruptions occur before the onset of symptoms (Harris et al., 2020). In support of this idea, longitudinal functional magnetic resonance imaging (fMRI) reveals significant changes in global-scale functional connectivity in AD patients (Dautricourt et al., 2021; Kundu et al., 2019; Sendi et al., 2020). Moreover, chemical tracer DiI-

based retrograde neural circuit tracing of the hippocampus in the 5xFAD mouse model demonstrates decreased hippocampal inputs from various brain regions (Jeon et al., 2018). This result indicates that quantitative circuit mapping approaches are merited for examining hippocampal circuit connectivity in AD mouse models.

One of the important aspects of the observations from AD mouse models and human patients is that neural circuit defects may precede behavioral symptoms; thus neural circuits may present a more amenable target for AD therapeutic interventions. It is reasonable to speculate that by the time symptoms appear after years of neural circuit losses, it may be too late for intervention. My dissertation work focuses on the new methods for mapping brain networks and how the neural circuit connections are impacted by AD in mouse models. We find points of convergence of specific circuit defects in mouse AD models that are consistent with poorly understood aspects of human AD such as sex differences in pathology, age of onset, and relative severity of behavioral deficits. I use state-of-the-art viral genetic tools to examine the cell-type specific circuit connectivity alterations in the hippocampal formation, a brain region that is critically impacted early in the disease process of AD.

In Chapter 1, I review the development of neural circuit tracers, from conventional chemical-based tracers to modern viral genetic tracers. The advancement of these tracers is instrumental to the studies of neural circuit connections that help to expand our understanding of the brain circuit organization and function in health and disease. The hippocampal formation is an essential region in the brain for learning and memory, and is critically impacted in AD - loss of neurons in the hippocampal formation, including the entorhinal cortex are some of the earliest detected features of AD (Braak et al., 1993). Therefore, utilizing novel viral genetic tools to map the circuit connectivity of hippocampal formation is of great importance.

A major circuit feature of the hippocampus is the excitatory trisynaptic circuit involving projections from granule cells in the dentate gyrus to pyramidal neurons in the CA3 and then to

pyramidal neurons in the CA1 (Andersen et al., 1971). The CA1 has glutamatergic pyramidal cells and GABAergic interneurons; and is anatomically divided into layers consisting of the stratum oriens, stratum pyramidale, stratum radiatum, and stratum lacunosum-moleculare (De No, 1933; De Nó, 1934; Ramón y Cajal, 1893). The stratum pyramidale (pyramidal layer) contains the somas of pyramidal neurons and is divided into a sparse deep sublayer and a thicker more compacted superficial sublayer (Dong et al., 2009).

The hippocampal CA1 has major inputs from brain regions both inside and outside the trisynaptic hippocampal pathway. The direct monosynaptic inputs dimensionally vary when moving between the dorsal to ventral CA1 (dCA1 and vCA1, respectively). Along the dorsoventral axis, the density of inputs to the dCA1 decreases while the density of inputs increases to the vCA1 (Tao et al., 2021). Based on monosynaptic rabies virus tracing, the major inputs to the dCA1 are from the ipsilateral CA3 and CA2 pyramidal layers, ipsilateral CA1 oriens layer, medial septum and diagonal band (MS-DB), and subiculum (Sun et al., 2014; Ye et al., 2022). Overall, the dCA1 has a higher number of inputs from the CA2 and CA3 while the vCA1 has stronger inputs from the CA3 and entorhinal cortex (ENT) (Tao et al., 2021). Regarding other extrahippocampal inputs, both dorsal and ventral CA1 have inputs from the hypothalamus, thalamus, striatum, and pallidum. Inputs from the olfactory cortex (OLF), amygdala, nucleus of reuniens (RE), and paraventricular nucleus of the thalamus (PVT) are found only in the vCA1, while the dCA1 has inputs from the ectorhinal cortex (ECT). This dichotomy merits further exploration (Tao et al., 2021). The strengths of these inputs to CA1 neurons (excitatory or inhibitory) are dependent on specific pathways and cell types (Sun et al., 2014). The vCA1 also contains neurons that project to regions of the brain associated with regulating the stress axis and approach-avoidance behavior (Gergues et al., 2020). These structural connectomic findings imply functional roles and encourage researchers to further evaluate these circuits. The CA1, having inputs from the CA3 and outputs to the subiculum leading out into the cortex, plays an important role in the

hippocampal function of encoding memory and learning (Amaral and Witter, 1989; Tsien et al., 1996).

The subiculum is an important output of the trisynaptic circuit in the hippocampal formation. Situated between the CA1 and other cortices, its dorsal and ventral regions have been shown to differ in their connectivity, cell types, and functions. Regarding the dorsal subiculum (dSUB), previous studies found that neurons sharing specific sublocations project to single target areas, implying functional connectivity (Gigg, 2006; Naber and Witter, 1998; Sharp and Green, 1994). Particularly, spatial information is delivered to and projected from the subiculum from and to distinct subpopulations (Gigg, 2006). However, recent studies, utilizing retrograde and anterograde tracing, revealed that the dSUB has efferents and afferents to and from multiple brain regions (Cembrowski et al., 2018; Kitanishi et al., 2021; Roy et al., 2017; Sun et al., 2019). Inputs to the dSUB include the dorsal CA1, parasubiculum, nucleus of the diagonal band, retrosplenial agranular cortex, entorhinal cortex, thalamic nuclei, and nucleus accumbens shell. Major outputs consist of the retrosplenial agranular cortex, medial EC layer V, postrhinal cortex, mammillary bodies, prefrontal cortex, and nucleus accumbens. Excitatory neurons within the dSUB are classified into two distinct subtypes based on their firing patterns: bursting and non-bursting cells (O'Mara, 2005; Roy et al., 2017; Sharp and Green, 1994; Taube, 1993). These two classes of dSUB neurons may have distinct morphology, topography, projections, and roles in behavior (O'Mara, 2005; Roy et al., 2017; Stewart, 1997). Spatial cells are intensely studied and are important cell types in the dSUB. Place, grid, boundary vector, head direction, object vector trace, and spatial geometry-related cells all play important roles in spatial recognition that can assist in proper movement and understanding of the space (Lever et al., 2009; Olson et al., 2017; Poulter et al., 2021; Sharp and Green, 1994; Sun et al., 2024). In contrast, excitatory neurons from the ventral subiculum (vSUB) project to key regions in the brain's reward system such as the entorhinal cortex, nucleus accumbens, prefrontal cortex, amygdala, and hypothalamus

(Groenewegen et al., 1987; Jay and Witter, 1991; Kishi et al., 2000). The vSUB also modulates stress through the hypothalamo-pituitary-adrenocortical (HPA) axis mainly through glutamate-GABAergic inhibitory connections to neurons in the hypothalamus and basal forebrain which in turn project to the paraventricular nucleus (Herman and Mueller, 2006). In summary, the subiculum plays important roles in connecting the hippocampus to the rest of the brain, and modulating spatial navigation, reward, and emotion.

AD has been shown to affect the anatomy and functionality of CA1 and SUB neurons. In human brains, MRI images of AD patients show atrophy of multiple layers of the CA1, particularly the pyramidal, stratum radiatum, and stratum lacunosum-moleculare layers (Blazquez-Llorca et al., 2011; Kerchner et al., 2012). The firing rates of CA1 neurons are also affected in AD models. How does this occur mechanistically? There is a tantalizing link between AD neuropathological protein chemistry and aberrant electrical activity. Soluble Aβ dimers induce hyperactivity even preceding Aβ plaque formation in young AD model mice and the neurons continue their hyperactivity in later stages near plaques (Brorson et al., 1995; Busche et al., 2008; Busche and Konnerth, 2016), thus providing a possible functional link between pathology and function in AD.

Based on this evidence, we hypothesize that age-related changes occur in both long-range and local hippocampal neural circuit connectivity in AD. Recent advancements in viral-genetic technologies offer new opportunities for semi-quantitative mapping of cell-type-specific neural circuit connections in AD mouse models.

In Chapter 2, I report our investigation utilizing a newly developed monosynaptic rabies tracing method to map hippocampal neural circuits in AD model mice to assess alterations in local and global circuit connectivity to hippocampal CA1 excitatory neurons in the single amyloid precursor protein knock-in (APP-KI) AD mouse model. To determine age-related AD progression, we measured circuit connectivity in age-matched littermate control and AD model mice at two different ages (3-4 vs. 10-11 months old). We quantitatively mapped the connectivity strengths of

neural circuit inputs to hippocampal CA1 excitatory neurons from brain regions including hippocampal subregions, medial septum, subiculum, and entorhinal cortex, comparing different age groups and genotypes. We focused on this brain region due to its clear relationship with learning and memory and because the hippocampal formation shows significant neuropathological changes in human AD. Our results reveal alterations in the circuit connectivity of hippocampal CA1 in AD model mice. Overall, we found weaker extrinsic connectivity CA1 input strengths in AD model mice compared to control mice, including sex differences with reduced subiculum to CA1 inputs in aged female AD mice compared to aged male AD mice. Unexpectedly, we observed a shift in connectivity patterns, with an increased proportion of inputs from the CA3 region to CA1 excitatory neurons when comparing young and old AD model mice, as well as old wild-type mice and old AD model mice. These unexpected shifts in CA3-CA1 input proportions in this AD mouse model suggest the possibility of compensatory circuit increases in response to connectivity losses in other parts of the hippocampal circuits. We expect that this work will provide new insights into the neural circuit mechanisms of AD pathogenesis.

In Chapter 3, I report our study of investigating subiculum neural circuit connections in AD model mice. The subiculum, a structure within the hippocampal formation, is one of the earliest brain regions affected by Alzheimer's disease (AD). To expand our understanding of AD's circuit-based mechanisms, I mapped synaptic circuit inputs to the dorsal SUB using monosynaptic rabies tracing in the 5xFAD mouse model. This study involved quantitatively comparing the circuit connectivity of SUB excitatory neurons in age-matched controls and 5xFAD mice of different ages and both sexes. The input-mapped brain regions included hippocampal subregions (CA1, CA2, CA3), medial septum and diagonal band (MS-DB), retrosplenial cortex (RSC), SUB, post subiculum (postSUB), visual cortex (Vis), auditory cortex (Aud), somatosensory cortex (SS), entorhinal cortex (EC), thalamus, perirhinal cortex (Prh), ectorhinal cortex (Ect), and temporal association cortex (TeA). Our findings reveal sex- and age-dependent changes in the connectivity

strengths and patterns of SUB presynaptic inputs from hippocampal subregions and other brain regions in 5xFAD mice compared to control mice. Significant sex differences in SUB inputs were observed in 5xFAD mice for CA1, CA2, CA3, postSUB, Prh, LEC, and MEC, all of which are critical areas for learning and memory. Notably, significant changes were found at different ages for visual cortical inputs to SUB. Although visual function is not typically considered defective in AD, these specific connectivity changes suggest altered visual circuitry contributing to learning and memory deficits. This study provides new insights into SUB-directed neural circuit mechanisms during AD progression and supports the notion that neural circuit disruptions are a prominent feature of AD.

In Chapter 4, I provide concluding remarks on my dissertation research. My work has helped to support a neural circuit-level perspective on Alzheimer's disease (AD) neuropathology and underscores the significance of using new viral genetic tracing techniques in unraveling neuronal circuit alterations. My studies presented in this dissertation provide new insights into neural circuit mechanisms underlying AD pathogenesis and support the notion that neural circuit disruptions are a prominent feature of AD.

References

Amaral, D.G., and Witter, M.P. (1989). The three-dimensional organization of the hippocampal formation: a review of anatomical data. Neuroscience *31*, 571-591.

Andersen, P., Bliss, T.V., and Skrede, K.K. (1971). Lamellar organization of hippocampal pathways. Experimental brain research *13*, 222-238.

Blazquez-Llorca, L., Garcia-Marin, V., Merino-Serrais, P., Avila, J., and DeFelipe, J. (2011). Abnormal tau phosphorylation in the thorny excrescences of CA3 hippocampal neurons in patients with Alzheimer's disease. J Alzheimers Dis *26*, 683-698.

Braak, H., Braak, E., and Bohl, J. (1993). Staging of Alzheimer-related cortical destruction. Eur Neurol *33*, 403-408.

Brorson, J.R., Bindokas, V.P., Iwama, T., Marcuccilli, C.J., Chisholm, J.C., and Miller, R.J. (1995). The Ca2+ influx induced by beta-amyloid peptide 25-35 in cultured hippocampal neurons results from network excitation. J Neurobiol *26*, 325-338.

Busche, M.A., Eichhoff, G., Adelsberger, H., Abramowski, D., Wiederhold, K.H., Haass, C., Staufenbiel, M., Konnerth, A., and Garaschuk, O. (2008). Clusters of hyperactive neurons near amyloid plaques in a mouse model of Alzheimer's disease. Science *321*, 1686-1689.

Busche, M.A., and Konnerth, A. (2016). Impairments of neural circuit function in Alzheimer's disease. Philos Trans R Soc Lond B Biol Sci *371*.

Cembrowski, M.S., Phillips, M.G., DiLisio, S.F., Shields, B.C., Winnubst, J., Chandrashekar, J., Bas, E., and Spruston, N. (2018). Dissociable Structural and Functional Hippocampal Outputs via Distinct Subiculum Cell Classes. Cell *173*, 1280-1292 e1218.

Dautricourt, S., de Flores, R., Landeau, B., Poisnel, G., Vanhoutte, M., Delcroix, N., Eustache, F., Vivien, D., de la Sayette, V., and Chetelat, G. (2021). Longitudinal Changes in Hippocampal Network Connectivity in Alzheimer's Disease. Ann Neurol *90*, 391-406.

De No, L. (1933). Studies on the structure of the cerebral cortex. J Psychol Neurol *45*, 381.

De Nó, R.L. (1934). Studies on the structure of the cerebral cortex XI Continuation of the study of the ammonic system. Journal fur Psychologie und Neurologie *46*, 113-177.

Dong, H.W., Swanson, L.W., Chen, L., Fanselow, M.S., and Toga, A.W. (2009). Genomic-anatomic evidence for distinct functional domains in hippocampal field CA1. Proceedings of the National Academy of Sciences of the United States of America *106*, 11794-11799.

Gergues, M.M., Han, K.J., Choi, H.S., Brown, B., Clausing, K.J., Turner, V.S., Vainchtein, I.D., Molofsky, A.V., and Kheirbek, M.A. (2020). Circuit and molecular architecture of a ventral hippocampal network. Nature neuroscience *23*, 1444-1452.

Gigg, J. (2006). Constraints on hippocampal processing imposed by the connectivity between CA1, subiculum and subicular targets. Behav Brain Res *174*, 265-271.

Groenewegen, H.J., Vermeulen-Van der Zee, E., te Kortschot, A., and Witter, M.P. (1987). Organization of the projections from the subiculum to the ventral striatum in the rat. A study using anterograde transport of Phaseolus vulgaris leucoagglutinin. Neuroscience *23*, 103-120.

Harris, S.S., Wolf, F., De Strooper, B., and Busche, M.A. (2020). Tipping the Scales: Peptide-Dependent Dysregulation of Neural Circuit Dynamics in Alzheimer's Disease. Neuron *107*, 417-435.

Herman, J.P., and Mueller, N.K. (2006). Role of the ventral subiculum in stress integration. Behav Brain Res *174*, 215-224.

Jay, T.M., and Witter, M.P. (1991). Distribution of hippocampal CA1 and subicular efferents in the prefrontal cortex of the rat studied by means of anterograde transport of Phaseolus vulgaris-leucoagglutinin. The Journal of comparative neurology *313*, 574-586.

Jeon, S.G., Kim, Y.J., Kim, K.A., Mook-Jung, I., and Moon, M. (2018). Visualization of Altered Hippocampal Connectivity in an Animal Model of Alzheimer's Disease. Mol Neurobiol *55*, 7886-7899.

Kerchner, G.A., Deutsch, G.K., Zeineh, M., Dougherty, R.F., Saranathan, M., and Rutt, B.K. (2012). Hippocampal CA1 apical neuropil atrophy and memory performance in Alzheimer's disease. Neuroimage *63*, 194-202.
Kishi, T., Tsumori, T., Ono, K., Yokota, S., Ishino, H., and Yasui, Y. (2000). Topographical organization of projections from the subiculum to the hypothalamus in the rat. The Journal of comparative neurology *419*, 205-222.
Kitanishi, T., Umaba, R., and Mizuseki, K. (2021). Robust information routing by dorsal subiculum neurons. Sci Adv *7*.
Kundu, S., Lukemire, J., Wang, Y., Guo, Y., and Alzheimer's Disease Neuroimaging, I. (2019). A Novel Joint Brain Network Analysis Using Longitudinal Alzheimer's Disease Data. Sci Rep *9*, 19589.
Lever, C., Burton, S., Jeewajee, A., O'Keefe, J., and Burgess, N. (2009). Boundary vector cells in the subiculum of the hippocampal formation. J Neurosci *29*, 9771-9777.
Matthews, K.A., Xu, W., Gaglioti, A.H., Holt, J.B., Croft, J.B., Mack, D., and McGuire, L.C. (2019). Racial and ethnic estimates of Alzheimer's disease and related dementias in the United States (2015-2060) in adults aged >/=65 years. Alzheimers Dement *15*, 17-24.
Naber, P.A., and Witter, M.P. (1998). Subicular efferents are organized mostly as parallel projections: a double-labeling, retrograde-tracing study in the rat. The Journal of comparative neurology *393*, 284-297.
O'Mara, S. (2005). The subiculum: what it does, what it might do, and what neuroanatomy has yet to tell us. J Anat *207*, 271-282.
Olson, J.M., Tongprasearth, K., and Nitz, D.A. (2017). Subiculum neurons map the current axis of travel. Nat Neurosci *20*, 170-172.
Poulter, S., Lee, S.A., Dachtler, J., Wills, T.J., and Lever, C. (2021). Vector trace cells in the subiculum of the hippocampal formation. Nat Neurosci *24*, 266-275.
Ramón y Cajal, S. (1893). Neue Darstellung vom histologischen Bau des Centralnervensystems. (No Title).
Roy, D.S., Kitamura, T., Okuyama, T., Ogawa, S.K., Sun, C., Obata, Y., Yoshiki, A., and Tonegawa, S. (2017). Distinct Neural Circuits for the Formation and Retrieval of Episodic Memories. Cell *170*, 1000-1012 e1019.
Sendi, M.S.E., Zendehrouh, E., Miller, R.L., Fu, Z., Du, Y., Liu, J., Mormino, E.C., Salat, D.H., and Calhoun, V.D. (2020). Alzheimer's Disease Projection From Normal to Mild Dementia Reflected in Functional Network Connectivity: A Longitudinal Study. Front Neural Circuits *14*, 593263.
Sharp, P.E., and Green, C. (1994). Spatial correlates of firing patterns of single cells in the subiculum of the freely moving rat. The Journal of neuroscience : the official journal of the Society for Neuroscience *14*, 2339-2356.
Stewart, M. (1997). Antidromic and orthodromic responses by subicular neurons in rat brain slices. Brain research *769*, 71-85.
Sun, Y., Jin, S., Lin, X., Chen, L., Qiao, X., Jiang, L., Zhou, P., Johnston, K.G., Golshani, P., Nie, Q.*, et al.* (2019). CA1-projecting subiculum neurons facilitate object-place learning. Nat Neurosci *22*, 1857-1870.
Sun, Y., Nguyen, A.Q., Nguyen, J.P., Le, L., Saur, D., Choi, J., Callaway, E.M., and Xu, X. (2014). Cell-type-specific circuit connectivity of hippocampal CA1 revealed through Cre-dependent rabies tracing. Cell reports *7*, 269-280.
Sun, Y., Nitz, D.A., Xu, X., and Giocomo, L.M. (2024). Subicular neurons encode concave and convex geometries. Nature.
Tao, S., Wang, Y., Peng, J., Zhao, Y., He, X., Yu, X., Liu, Q., Jin, S., and Xu, F. (2021). Whole-Brain Mapping the Direct Inputs of Dorsal and Ventral CA1 Projection Neurons. Front Neural Circuits *15*, 643230.
Taube, J.S. (1993). Electrophysiological properties of neurons in the rat subiculum in vitro. Experimental brain research *96*, 304-318.

Tsien, J.Z., Huerta, P.T., and Tonegawa, S. (1996). The essential role of hippocampal CA1 NMDA receptor-dependent synaptic plasticity in spatial memory. Cell *87*, 1327-1338.
Ye, Q., Gast, G., Su, X., Saito, T., Saido, T.C., Holmes, T.C., and Xu, X. (2022). Hippocampal neural circuit connectivity alterations in an Alzheimer's disease mouse model revealed by monosynaptic rabies virus tracing. Neurobiol Dis *172*, 105820.

Chapter 1: New Technical Advancements in Neural Circuit Mapping

Here I provide an overview of new technical advancements in neural circuit mapping by focusing on describing both conventional neural tracers and state-of-the-art virus-based tracers. I also discuss their relevant applications in mapping the brain circuit organization and function in health and disease.

Conventional tracers

Prior to the use of viral genetic tracers, conventional chemical tracers were widely used to uncover the connections in the nervous system. Starting from the 1970s, Horseradish peroxidase (HRP) has been used to retrogradely label neurons. The inadequate uptake through passive endocytosis requires HRP conjugation with plant lectin wheat germ agglutinin (WGA) or cholera toxin subunit B (CTb) for signal amplification (Kobbert et al., 2000; Kristensson and Olsson, 1971; LaVail and LaVail, 1972; Staines et al., 1980; Trojanowski et al., 1981, 1982; Vercelli et al., 2000). These conjugations boost uptake and allow HRP to be identified more readily by fluorophores and immunohistochemistry (IHC) using light microscopy. However, one drawback of HRP conjugate is that the transport is not unidirectional (van der Want et al., 1997).

CTb remains a valuable conventional retrograde tracer (Ericson and Blomqvist, 1988; Luppi et al., 1990; Luppi et al., 1987; Stoeckel et al., 1977). It has low toxicity, binds to cell surface receptors, and can be identified through IHC, MRI labeling, or, most commonly, fluorescent conjugation (Conte et al., 2009; Wu et al., 2011). Fluorescently conjugated CTb exhibits the benefits of a strong signal and a quick incubation time of within ~3-7 days (Cui et al., 2022). Similar to HRP, CTb has also been shown to display anterograde traveling (Angelucci et al., 1996).

The synthetic retrograde tracer, Hydroxystilbamidine (FluoroGold™) exhibits very strong labeling that can be further enhanced with antibody staining and can be measured using fluorescent light microscopy. FluoroGold™ enters neurons through fluid phase endocytosis (Kobbert et al., 2000; Lanciego and Wouterlood, 2011). It is useful for long-term experiments

because the staining is long-lasting, and the signal persists for up to a year. However, FluoroGold™ cannot be targeted to specific cell types.

Fluorescent dyes such as DiI (red) and DiO (green) are often used in circuit tracing, and they travel both retrogradely and anterogradely. They produce balanced staining due to their lipophilic nature which allows them to spread evenly over long periods of time after injection (Boon et al., 2019; Kobbert et al., 2000; Thanos et al., 1992; Trivino-Paredes et al., 2019). Additionally, fluorescent latex microspheres 30-90 nm diameter (Retrobeads™) are one of the few conventional tracers that are solely retrograde. Their color retains its brightness and is nontoxic, making them viable for long-term experiments (Katz et al., 1984; Katz and Iarovici, 1990).

A popular anterograde conventional tracer is Phaseolus vulgaris-leucoagglutinin (PHA-L) (Gerfen and Sawchenko, 1984). Enhanced by IHC, PHA-L intricately labels neuronal axon terminal boutons, entering neurons by binding to carbohydrates on the cell surface (Lanciego and Wouterlood, 2011; Wouterlood et al., 2014). The post-injection incubation time typically ranges between 10-20 days (Vercelli et al., 2000). Dextran-amines (DAs) are bidirectional tracers, and while they may produce extensively detailed staining signals through diffusion, their direction of connectivity is unclear (Fritzsch, 1993; Glover et al., 1986; Kobbert et al., 2000; Lanciego and Wouterlood, 2011; Schmued et al., 1990; Wouterlood et al., 2014; Zhang et al., 2017). DAs are visible following the conjugation enhancement with fluorophores, biotinylation, and tetramethylrhodamine (TRITC)-conjugation (Dempsey et al., 2015; Noseda et al., 2010).

Conventional chemical tracers produce less specific labeling compared to novel viral tracers: they are 1) not cell-type specific, 2) nor are they quantitative. Most chemical tracers have some bi-directional labeling (Angelucci et al., 1996; Fritzsch, 1993; Glover, 1995; Luppi et al., 1987; Noseda et al., 2010; Schmued et al., 1990; Zhang et al., 2017). Chemical tracers are also biased for distant long-range connections because of the strong labeling at the injection site that obscures nearby labeled neurons due to local dye saturation at the injection site (Dempsey et al., 2017; Henriksen et al., 2016; Oh et al., 2014; van den Heuvel et al., 2016).

Viral-genetic neural tracers

Rabies virus

Over the past few decades, scientists have developed multiple viral tracers that can be applied to target specific cell groups in order to study neural circuit connections. These newer tracers can be categorized as anterograde or retrograde tracers depending on whether they label the postsynaptic or presynaptic neurons, respectively – these desirable features are based on the careful selection of viral variants that exhibit strict directional properties. Different classes of neurotrophic viruses have been modified for viral-based circuit labeling technologies. A currently popular viral labeling approach is based on modified rabies virus variants. Rabies viruses are intrinsically neurotrophic and can evade immune detection by "hiding out" in the brain. Wild rabies viruses infect the central nervous system and travel trans-synaptically in a retrograde direction. Rabies has a single-stranded, negative sense, unsegmented RNA genome that encodes for five proteins (Rupprecht, 1996). Rabies virus variants have been engineered to exhibit retrograde monosynaptic tracing properties, thus the labeling is highly directional and is limited to direct mono-synaptic inputs to target neurons. The first generation of genetically-engineered monosynaptic rabies is based on an attenuated vaccine strain: the SAD-B19 strain. The monosynaptic traveling is achieved by the deletion of the Glycoprotein (G) gene and the use of pseudotyping to facilitate monosynaptic viral spread and cell-type-specific targeting (Etessami et al., 2000; Mebatsion et al., 1996; Wickersham et al., 2007b). Specifically, G is an envelope protein that acts as a key to allow the virus to infect presynaptic neurons through their terminals. The G is exposed on the surface of the host cell when the virus buds out (Finke and Conzelmann, 2005; Morimoto et al., 2000). Deleting the gene for G creates Glycoprotein-deleted rabies viruses (RVΔ*G*) that cannot reproduce G in host neurons. This eliminates the ability of the virus to further infect neurons (Etessami et al., 2000).

To control tracing in mammalian brains, the avian sarcoma leukosis virus type A envelope protein (EnvA) is commonly pseudotyped with RVΔ*G* creating EnvA+RVΔG (Young et al., 1993).

To infect cells, EnvA binds to the tumor virus receptor A (TVA) which otherwise is not expressed in mammals. This confers specificity by only targeting TVA-expressing neurons (Osakada and Callaway, 2013; Wickersham et al., 2007b). While there are different ways to confer target specificity in neurons, the majority of these approaches revolve around targeting cells to express TVA in a Cre-dependent manner, using molecular genetics. This is typically achieved by using a mouse line that expresses Cre recombinase in a desired cell type and then crossing it with a mouse line that facilitates Cre-dependent expression of TVA and G (Bourane et al., 2015; Li et al., 2013). Alternative methods utilize helper viruses, with or without Cre driver mouse lines (Wall et al., 2010). With a Cre driver line, a helper virus expresses TVA and G in Cre+ cells. If a Cre driver line is not used, a combination of helper AAV viruses is needed to direct the expression of Cre (Ye et al., 2022). One helper virus directs Cre expression to target neurons using a cell-type selective promoter. The second helper virus carries the genetic payload to express TVA and G. Neurons infected with a helper virus and EnvA+RVΔG are classified as starter cells, and all single RV-labeled neurons are inputs to these starter neurons. Together, these methods restrict RVΔ*G* monosynaptic spread. The Cre-dependent RV can also be combined with the retrograde canine-adeno virus (CAV) 2 to map the input-output circuits as TRIO (for tracing the relationship between input and output) and cell-type-specific TRIO (cTRIO) systems (Schwarz et al., 2015).

The genetically-engineered RV can be integrated with a series of reporters for *in vivo* functional studies, such as fluorescent proteins, calcium indicators, and synaptic markers (Bouin et al., 2024). For circuit mapping, fluorescent protein genes are inserted into the helper and rabies virus genome. For example, green fluorescent protein can be used to distinguish neurons infected with the helper virus, and red fluorescent reporter for rabies-infected neurons. Input neurons will appear red, while starter neurons, containing both green and red fluorescent markers, appear yellow (Ye et al., 2022). Since both the starter neurons and the presynaptic input neurons can be clearly labeled, imaged, and quantified, the cell-type specific rabies virus strategy adds a powerful new benefit: quantitative labeling.

Quantification and statistical comparisons of rabies tracing results offer a promising platform for precisely measuring neural circuit connection strengths. This is a critically important feature for studying circuit connections in AD, because it allows us to determine whether the degree of connectivity of a complex neural circuit is altered in AD (Ye et al., 2022). While we may tacitly be biased that AD lowers circuit connectivity, we have to consider the formal possibility that some circuit connections are actually upregulated through compensatory processes during the different stages of the disease. These results are just as informative. The neural circuit connectivity strengths are described as connectivity strength index (CSI) and proportion of inputs (PI), respectively. The CSI is defined as the division of the number of input-mapped presynaptic rabies-labeled neurons within a brain region over the number of starter neurons; whereas the PI is defined as the proportion of input-mapped neurons within a subregion divided by the total number of rabies-labeled neurons across the entire brain. Therefore, the CSI is an absolute measurement of the connectivity, whereas PI reflects the proportional distribution of these inputs. These quantitative connectivity measurements can be extremely useful especially when applied to disease models such as AD. The circuit connectivity of interest can be quantitatively compared in age, gender-matched AD model mice and wild type (WT) controls. Understanding how the number and strength of inputs change can deepen our knowledge of the mechanisms behind the disease and guide future possible interventions. As function follows structure, we may investigate in the future if changes in neural circuitry caused by AD are responsible for specific behavioral defects.

There are still technological issues concerning viruses as circuit mapping tools that need to be worked out. Viral tracers have innate toxicity and tropism. While RVΔG has removed the capability to exit and infect new cells, RVΔG-modified rabies viruses continue to replicate within the already infected cells. While this confers high expression of desirable transgenes such as fluorescent markers, it also leads to high cytotoxicity. High toxicity eventually causes cell death around two weeks after infection. Unfortunately, this shortens the period available for experiments

and imposes strict limits on functional studies such as imaging, recording, and behavioral analysis (Wickersham et al., 2007a). Thus, further attenuation of modified virus toxicity is an important goal. A different strain of rabies virus-CVS N2c strain allows rabies-infected neurons to survive for a longer time (Reardon et al., 2016). Moreover, the deletion of a second gene that codes for the viral polymerase has been shown to reduce the cytotoxicity of the SAD strain (Chatterjee et al., 2018). Without the viral polymerase, the ΔGL virus can only express minimal amounts of recombinases from its transgenic payload to activate Cre- or Flp-dependent reporter gene expression while preserving the infected neuron health state. A more recent innovation from the same group is the addition of molecular controls that suppress the viral expression after initial viral replication using doxycycline in a Tet-off system, the ΔGL virus-infected neurons survived over 12 weeks (Jin et al., 2024). Another recent innovation involves the development of a polysynaptic rabies tracing approach that uses transgenic GT mice, which expresses both G and TVA. This approach results in low animal toxicity, which allows for long-term whole-body tracing experiments (Song et al., 2023).

Herpes Simplex Virus

Besides the monosynaptic rabies virus, other viral tracers have been actively developed for neural tracing studies. The herpes simplex virus (HSV-1), particularly the H129 strain, is a wild-type virus that has been extensively modified to optimize viral tracing. Wild type H129 travels trans-synaptically mostly in the anterograde direction, while sometimes showing retrograde spread through axon terminal invasion (Wojaczynski et al., 2015; Yang et al., 2022). Modification of its genome to be dependent on Cre-recombinase to replicate and express transgenes such as fluorescent markers in conjunction with a Cre mouse line or Cre helper virus has made H129 a useful anterograde viral tracer used for the past decades (Labetoulle et al., 2000; Lo and Anderson, 2011; Sun et al., 1996). HSV-1 has also been modified for monosynaptic tracing by the creation of H129-ΔTK-tdT (Zeng et al., 2017). The thymidine kinase (TK) is essential for viral

replication. Deletion of TK limits H129 replication and spread to connecting neurons. This property can be exploited by targeted expression of TK through transgenes delivery via helper viruses to neurons of interest. More recently, the H129 strain has been optimized for stronger fluorescent intensity and higher anterograde spreading by deleting glycoprotein K (gK) (Yang et al., 2022). However, the current H129 strain still shows relatively high cytotoxicity, which requires further extensive research on virus attenuation.

Adeno-associated virus

The adeno-associated virus (AAV) is a popular viral tracer modified to be used on its own or in conjunction with other viral tracers as a helper virus. AAV1 and AAV9 are useful serotypes used for trans-synaptic anterograde and transgene expression in postsynaptic neurons when combined with Cre-recombinase (Zingg et al., 2017). However, these viruses exhibit partial retrograde labeling – and this may confound results (Castle et al., 2016; Rothermel et al., 2013). With the directed evolution-guided virus capsid selection, rAAV2-retro shows promising retrograde capacity (Tervo et al., 2016). rAAV2-retro is taken up through the synapses at the injection site and travels retrogradely from the axon terminal to the cell body. The strong upsides to rAAV2-retro include low toxicity, small injection volumes, and similar results as compared to conventional tracers such as fluorogold (Sun et al., 2019; Tervo et al., 2016). More recently, an AAV2-based anterograde tracer system: Trans-Seq was developed. It combines WGA with mCherry fluorescent marker, as well as single-cell RNA sequencing to profile postsynaptic cells. This system shows promising results (Tsai et al., 2022).

Yellow fever virus

Yellow fever virus (YFV) has emerged recently as a powerful tool for viral circuit tracing. YFV travels in the anterograde direction and can be modified to travel monosynaptically or polysynaptically. The YFV tracer was developed by modifying YFV-17D, a live attenuated vaccine

that exhibits relatively low intrinsic toxicity (Li et al., 2021). The NS1 in the YFV genome is essential for virus replication (Das et al., 2016). Initial deletion of the NS1 YFV$^{\triangle NS1}$ leads to adequate postsynaptic labeling. However, evidence shows that the virus begins to travel retrogradely if it is incubated for ~12 days. Therefore, the virus has been further modified to respond to doxycycline (Dox)-controlled Tet-On or Tet-Off systems, thus allowing for calibration of transient replication by controlling the production of NS1. This can be achieved by helper AAV virus injection, which allows for NS1 to be produced only when Dox is delivered (Tet-On) or absent (Tet-Off). When used in conjunction with NS1-deleted YFV (YFV$^{\triangle NS1}$), it controls the replication of the virus. This allows for a short-term and controlled replication, thereby preventing damage caused to infected neurons by excessive replication and highly reducing the toxicity of YFV. Combined with the Cre system, YFV$^{\triangle NS1\text{-}Cre}$ is genetically expressed in postsynaptic neurons for *in vivo* calcium imaging in freely behaving mice. Deleting the gene for CME, a structural protein, makes YFV$^{\triangle CME}$ a candidate for use in monosynaptic tracing. The combination of these gene deletions makes YFV$^{\triangle CMENS1\text{-}Cre}$ monosynaptic, less toxic, and exclusively anterograde – and the system shows great promise for further development and modification.

Summary

These newly developed technological advancements present new opportunities for cell-type-specific and pathway-specific neural circuit mapping in AD-directed brain research. In the context of my dissertation research, I focus on using helper AAVs and monosynaptic rabies virus to quantitatively map the input connections of hippocampal CA1 and SUB regions in control and AD model mice.

References

Angelucci, A., Clasca, F., and Sur, M. (1996). Anterograde axonal tracing with the subunit B of cholera toxin: a highly sensitive immunohistochemical protocol for revealing fine axonal morphology in adult and neonatal brains. Journal of neuroscience methods *65*, 101-112.

Boon, J., Clarke, E., Kessaris, N., Goffinet, A., Molnar, Z., and Hoerder-Suabedissen, A. (2019). Long-range projections from sparse populations of GABAergic neurons in murine subplate. The Journal of comparative neurology *527*, 1610-1620.

Bouin, A., Wu, G., Koyuncu, O.O., Ye, Q., Kim, K.Y., Wu, M.Y., Tong, L., Chen, L., Phan, S., Mackey, M.R.*, et al.* (2024). New rabies viral resources for multi-scale neural circuit mapping. Mol Psychiatry.

Bourane, S., Grossmann, K.S., Britz, O., Dalet, A., Del Barrio, M.G., Stam, F.J., Garcia-Campmany, L., Koch, S., and Goulding, M. (2015). Identification of a spinal circuit for light touch and fine motor control. Cell *160*, 503-515.

Castle, M.J., Turunen, H.T., Vandenberghe, L.H., and Wolfe, J.H. (2016). Controlling AAV Tropism in the Nervous System with Natural and Engineered Capsids. Methods Mol Biol *1382*, 133-149.

Chatterjee, S., Sullivan, H.A., MacLennan, B.J., Xu, R., Hou, Y., Lavin, T.K., Lea, N.E., Michalski, J.E., Babcock, K.R., Dietrich, S.*, et al.* (2018). Nontoxic, double-deletion-mutant rabies viral vectors for retrograde targeting of projection neurons. Nat Neurosci *21*, 638-646.

Conte, W.L., Kamishina, H., and Reep, R.L. (2009). Multiple neuroanatomical tract-tracing using fluorescent Alexa Fluor conjugates of cholera toxin subunit B in rats. Nat Protoc *4*, 1157-1166.

Cui, J.J., Wang, J., Xu, D.S., Wu, S., Guo, Y.T., Su, Y.X., Liu, Y.H., Wang, Y.Q., Jing, X.H., and Bai, W.Z. (2022). Alexa Fluor 488-conjugated cholera toxin subunit B optimally labels neurons 3-7 days after injection into the rat gastrocnemius muscle. Neural Regen Res *17*, 2316-2320.

Das, A.T., Tenenbaum, L., and Berkhout, B. (2016). Tet-On Systems For Doxycycline-inducible Gene Expression. Curr Gene Ther *16*, 156-167.

Dempsey, B., Le, S., Turner, A., Bokiniec, P., Ramadas, R., Bjaalie, J.G., Menuet, C., Neve, R., Allen, A.M., Goodchild, A.K.*, et al.* (2017). Mapping and Analysis of the Connectome of Sympathetic Premotor Neurons in the Rostral Ventrolateral Medulla of the Rat Using a Volumetric Brain Atlas. Front Neural Circuits *11*, 9.

Dempsey, B., Turner, A.J., Le, S., Sun, Q.J., Bou Farah, L., Allen, A.M., Goodchild, A.K., and McMullan, S. (2015). Recording, labeling, and transfection of single neurons in deep brain structures. Physiol Rep *3*.

Ericson, H., and Blomqvist, A. (1988). Tracing of neuronal connections with cholera toxin subunit B: light and electron microscopic immunohistochemistry using monoclonal antibodies. Journal of neuroscience methods *24*, 225-235.

Etessami, R., Conzelmann, K.K., Fadai-Ghotbi, B., Natelson, B., Tsiang, H., and Ceccaldi, P.E. (2000). Spread and pathogenic characteristics of a G-deficient rabies virus recombinant: an in vitro and in vivo study. J Gen Virol *81*, 2147-2153.

Finke, S., and Conzelmann, K.K. (2005). Replication strategies of rabies virus. Virus Res *111*, 120-131.

Fritzsch, B. (1993). Fast axonal diffusion of 3000 molecular weight dextran amines. J Neurosci Methods *50*, 95-103.

Gerfen, C.R., and Sawchenko, P.E. (1984). An anterograde neuroanatomical tracing method that shows the detailed morphology of neurons, their axons and terminals: immunohistochemical localization of an axonally transported plant lectin, Phaseolus vulgaris leucoagglutinin (PHA-L). Brain Res *290*, 219-238.

Glover, J. (1995). Retrograde and anterograde axonal tracing with fluorescent dextran-amines in the embryonic nervous system. Neurosci Prot *30*, 1-13.
Glover, J.C., Petursdottir, G., and Jansen, J.K. (1986). Fluorescent dextran-amines used as axonal tracers in the nervous system of the chicken embryo. Journal of neuroscience methods *18*, 243-254.
Henriksen, S., Pang, R., and Wronkiewicz, M. (2016). A simple generative model of the mouse mesoscale connectome. Elife *5*, e12366.
Jin, L., Sullivan, H.A., Zhu, M., Lavin, T.K., Matsuyama, M., Fu, X., Lea, N.E., Xu, R., Hou, Y., Rutigliani, L.*, et al.* (2024). Long-term labeling and imaging of synaptically connected neuronal networks in vivo using double-deletion-mutant rabies viruses. Nature neuroscience *27*, 373-383.
Katz, L.C., Burkhalter, A., and Dreyer, W.J. (1984). Fluorescent latex microspheres as a retrograde neuronal marker for in vivo and in vitro studies of visual cortex. Nature *310*, 498-500.
Katz, L.C., and Iarovici, D.M. (1990). Green fluorescent latex microspheres: a new retrograde tracer. Neuroscience *34*, 511-520.
Kobbert, C., Apps, R., Bechmann, I., Lanciego, J.L., Mey, J., and Thanos, S. (2000). Current concepts in neuroanatomical tracing. Prog Neurobiol *62*, 327-351.
Kristensson, K., and Olsson, Y. (1971). Retrograde axonal transport of protein. Brain research *29*, 363-365.
Labetoulle, M., Kucera, P., Ugolini, G., Lafay, F., Frau, E., Offret, H., and Flamand, A. (2000). Neuronal pathways for the propagation of herpes simplex virus type 1 from one retina to the other in a murine model. J Gen Virol *81*, 1201-1210.
Lanciego, J.L., and Wouterlood, F.G. (2011). A half century of experimental neuroanatomical tracing. J Chem Neuroanat *42*, 157-183.
LaVail, J.H., and LaVail, M.M. (1972). Retrograde axonal transport in the central nervous system. Science *176*, 1416-1417.
Li, E., Guo, J., Oh, S.J., Luo, Y., Oliveros, H.C., Du, W., Arano, R., Kim, Y., Chen, Y.T., Eitson, J.*, et al.* (2021). Anterograde transneuronal tracing and genetic control with engineered yellow fever vaccine YFV-17D. Nat Methods *18*, 1542-1551.
Li, Y., Stam, F.J., Aimone, J.B., Goulding, M., Callaway, E.M., and Gage, F.H. (2013). Molecular layer perforant path-associated cells contribute to feed-forward inhibition in the adult dentate gyrus. Proceedings of the National Academy of Sciences of the United States of America *110*, 9106-9111.
Lo, L., and Anderson, D.J. (2011). A Cre-dependent, anterograde transsynaptic viral tracer for mapping output pathways of genetically marked neurons. Neuron *72*, 938-950.
Luppi, P.H., Fort, P., and Jouvet, M. (1990). Iontophoretic application of unconjugated cholera toxin B subunit (CTb) combined with immunohistochemistry of neurochemical substances: a method for transmitter identification of retrogradely labeled neurons. Brain research *534*, 209-224.
Luppi, P.H., Sakai, K., Salvert, D., Fort, P., and Jouvet, M. (1987). Peptidergic hypothalamic afferents to the cat nucleus raphe pallidus as revealed by a double immunostaining technique using unconjugated cholera toxin as a retrograde tracer. Brain research *402*, 339-345.
Mebatsion, T., Konig, M., and Conzelmann, K.K. (1996). Budding of rabies virus particles in the absence of the spike glycoprotein. Cell *84*, 941-951.
Morimoto, K., Foley, H.D., McGettigan, J.P., Schnell, M.J., and Dietzschold, B. (2000). Reinvestigation of the role of the rabies virus glycoprotein in viral pathogenesis using a reverse genetics approach. J Neurovirol *6*, 373-381.
Noseda, R., Kainz, V., Jakubowski, M., Gooley, J.J., Saper, C.B., Digre, K., and Burstein, R. (2010). A neural mechanism for exacerbation of headache by light. Nat Neurosci *13*, 239-245.
Oh, S.W., Harris, J.A., Ng, L., Winslow, B., Cain, N., Mihalas, S., Wang, Q., Lau, C., Kuan, L., Henry, A.M.*, et al.* (2014). A mesoscale connectome of the mouse brain. Nature *508*, 207-214.
Osakada, F., and Callaway, E.M. (2013). Design and generation of recombinant rabies virus vectors. Nat Protoc *8*, 1583-1601.

Reardon, T.R., Murray, A.J., Turi, G.F., Wirblich, C., Croce, K.R., Schnell, M.J., Jessell, T.M., and Losonczy, A. (2016). Rabies Virus CVS-N2c(DeltaG) Strain Enhances Retrograde Synaptic Transfer and Neuronal Viability. Neuron *89*, 711-724.
Rothermel, M., Brunert, D., Zabawa, C., Diaz-Quesada, M., and Wachowiak, M. (2013). Transgene expression in target-defined neuron populations mediated by retrograde infection with adeno-associated viral vectors. The Journal of neuroscience : the official journal of the Society for Neuroscience *33*, 15195-15206.
Rupprecht, C.E. (1996). Rhabdoviruses: rabies virus. Medical microbiology *4*.
Schmued, L., Kyriakidis, K., and Heimer, L. (1990). In vivo anterograde and retrograde axonal transport of the fluorescent rhodamine-dextran-amine, Fluoro-Ruby, within the CNS. Brain Res *526*, 127-134.
Schwarz, L.A., Miyamichi, K., Gao, X.J., Beier, K.T., Weissbourd, B., DeLoach, K.E., Ren, J., Ibanes, S., Malenka, R.C., Kremer, E.J*., et al.* (2015). Viral-genetic tracing of the input-output organization of a central noradrenaline circuit. Nature *524*, 88-92.
Song, Y., Li, L., Ma, T., Zhang, B., Wang, J., Tang, X., Lu, Y., He, A., and Li, X. (2023). A Novel Mouse Model for Polysynaptic Retrograde Tracing and Rabies Pathological Research. Cell Mol Neurobiol *43*, 3743-3752.
Staines, W.A., Kimura, H., Fibiger, H.C., and McGeer, E.G. (1980). Peroxidase-labeled lectin as a neuroanatomical tracer: evaluation in a CNS pathway. Brain research *197*, 485-490.
Stoeckel, K., Schwab, M., and Thoenen, H. (1977). Role of gangliosides in the uptake and retrograde axonal transport of cholera and tetanus toxin as compared to nerve growth factor and wheat germ agglutinin. Brain research *132*, 273-285.
Sun, L., Tang, Y., Yan, K., Yu, J., Zou, Y., Xu, W., Xiao, K., Zhang, Z., Li, W., Wu, B*., et al.* (2019). Differences in neurotropism and neurotoxicity among retrograde viral tracers. Mol Neurodegener *14*, 8.
Sun, N., Cassell, M.D., and Perlman, S. (1996). Anterograde, transneuronal transport of herpes simplex virus type 1 strain H129 in the murine visual system. Journal of virology *70*, 5405-5413.
Tervo, D.G., Hwang, B.Y., Viswanathan, S., Gaj, T., Lavzin, M., Ritola, K.D., Lindo, S., Michael, S., Kuleshova, E., Ojala, D*., et al.* (2016). A Designer AAV Variant Permits Efficient Retrograde Access to Projection Neurons. Neuron *92*, 372-382.
Thanos, S., Vanselow, J., and Mey, J. (1992). Ganglion cells in the juvenile chick retina and their ability to regenerate axons in vitro. Exp Eye Res *54*, 377-391.
Trivino-Paredes, J.S., Nahirney, P.C., Pinar, C., Grandes, P., and Christie, B.R. (2019). Acute slice preparation for electrophysiology increases spine numbers equivalently in the male and female juvenile hippocampus: a DiI labeling study. J Neurophysiol *122*, 958-969.
Trojanowski, J.Q., Gonatas, J.O., and Gonatas, N.K. (1981). Conjugates of horseradish peroxidase (HRP) with cholera toxin and wheat germ agglutinin are superior to free HRP as orthogradely transported markers. Brain research *223*, 381-385.
Trojanowski, J.Q., Gonatas, J.O., and Gonatas, N.K. (1982). Horseradish peroxidase (HRP) conjugates of cholera toxin and lectins are more sensitive retrogradely transported markers than free HRP. Brain research *231*, 33-50.
Tsai, N.Y., Wang, F., Toma, K., Yin, C., Takatoh, J., Pai, E.L., Wu, K., Matcham, A.C., Yin, L., Dang, E.J*., et al.* (2022). Trans-Seq maps a selective mammalian retinotectal synapse instructed by Nephronectin. Nature neuroscience *25*, 659-674.
van den Heuvel, M.P., Bullmore, E.T., and Sporns, O. (2016). Comparative Connectomics. Trends Cogn Sci *20*, 345-361.
van der Want, J.J., Klooster, J., Cardozo, B.N., de Weerd, H., and Liem, R.S. (1997). Tract-tracing in the nervous system of vertebrates using horseradish peroxidase and its conjugates: tracers, chromogens and stabilization for light and electron microscopy. Brain Res Brain Res Protoc *1*, 269-279.

Vercelli, A., Repici, M., Garbossa, D., and Grimaldi, A. (2000). Recent techniques for tracing pathways in the central nervous system of developing and adult mammals. Brain research bulletin *51*, 11-28.
Wall, N.R., Wickersham, I.R., Cetin, A., De La Parra, M., and Callaway, E.M. (2010). Monosynaptic circuit tracing in vivo through Cre-dependent targeting and complementation of modified rabies virus. Proceedings of the National Academy of Sciences of the United States of America *107*, 21848-21853.
Wickersham, I.R., Finke, S., Conzelmann, K.K., and Callaway, E.M. (2007a). Retrograde neuronal tracing with a deletion-mutant rabies virus. Nat Methods *4*, 47-49.
Wickersham, I.R., Lyon, D.C., Barnard, R.J., Mori, T., Finke, S., Conzelmann, K.K., Young, J.A., and Callaway, E.M. (2007b). Monosynaptic restriction of transsynaptic tracing from single, genetically targeted neurons. Neuron *53*, 639-647.
Wojaczynski, G.J., Engel, E.A., Steren, K.E., Enquist, L.W., and Patrick Card, J. (2015). The neuroinvasive profiles of H129 (herpes simplex virus type 1) recombinants with putative anterograde-only transneuronal spread properties. Brain Struct Funct *220*, 1395-1420.
Wouterlood, F.G., Bloem, B., Mansvelder, H.D., Luchicchi, A., and Deisseroth, K. (2014). A fourth generation of neuroanatomical tracing techniques: exploiting the offspring of genetic engineering. Journal of neuroscience methods *235*, 331-348.
Wu, C.W., Vasalatiy, O., Liu, N., Wu, H., Cheal, S., Chen, D.Y., Koretsky, A.P., Griffiths, G.L., Tootell, R.B., and Ungerleider, L.G. (2011). Development of a MR-visible compound for tracing neuroanatomical connections in vivo. Neuron *70*, 229-243.
Yang, H., Xiong, F., Qin, H.B., Yu, Q.T., Sun, J.Y., Zhao, H.W., Li, D., Zhou, Y., Zhang, F.K., Zhu, X.W*., et al.* (2022). A novel H129-based anterograde monosynaptic tracer exhibits features of strong labeling intensity, high tracing efficiency, and reduced retrograde labeling. Mol Neurodegener *17*, 6.
Ye, Q., Gast, G., Su, X., Saito, T., Saido, T.C., Holmes, T.C., and Xu, X. (2022). Hippocampal neural circuit connectivity alterations in an Alzheimer's disease mouse model revealed by monosynaptic rabies virus tracing. Neurobiol Dis *172*, 105820.
Young, J.A., Bates, P., and Varmus, H.E. (1993). Isolation of a chicken gene that confers susceptibility to infection by subgroup A avian leukosis and sarcoma viruses. Journal of virology *67*, 1811-1816.
Zeng, W.B., Jiang, H.F., Gang, Y.D., Song, Y.G., Shen, Z.Z., Yang, H., Dong, X., Tian, Y.L., Ni, R.J., Liu, Y*., et al.* (2017). Anterograde monosynaptic transneuronal tracers derived from herpes simplex virus 1 strain H129. Mol Neurodegener *12*, 38.
Zhang, W., Xu, D., Cui, J., Jing, X., Xu, N., Liu, J., and Bai, W. (2017). Anterograde and retrograde tracing with high molecular weight biotinylated dextran amine through thalamocortical and corticothalamic pathways. Microsc Res Tech *80*, 260-266.
Zingg, B., Chou, X.L., Zhang, Z.G., Mesik, L., Liang, F., Tao, H.W., and Zhang, L.I. (2017). AAV-Mediated Anterograde Transsynaptic Tagging: Mapping Corticocollicular Input-Defined Neural Pathways for Defense Behaviors. Neuron *93*, 33-47.

Chapter 2: Hippocampal Neural Circuit Connectivity Alterations in an Alzheimer's Disease Mouse Model Revealed by Monosynaptic Rabies Virus Tracing

Abstract

Alzheimer's disease (AD) is a progressive neurodegenerative disorder with growing major health impacts, particularly in countries with aging populations. The examination of neural circuit mechanisms in AD mouse models is a recent focus for identifying new AD treatment strategies. We hypothesize that age-progressive changes of both long-range and local hippocampal neural circuit connectivity occur in AD. Recent advancements in viral-genetic technologies provide new opportunities for semi-quantitative mapping of cell-type-specific neural circuit connections in AD mouse models. We applied a recently developed monosynaptic rabies tracing method to hippocampal neural circuit mapping studies in AD model mice to determine how local and global circuit connectivity to hippocampal CA1 excitatory neurons may be altered in the single amyloid precursor protein knock-in (APP-KI) AD mouse model. To determine age-related AD progression, we measured circuit connectivity in age-matched littermate control and AD model mice at two different ages (3-4 vs. 10-11 months old). We semi-quantitatively mapped the connectivity strengths of neural circuit inputs to hippocampal CA1 excitatory neurons from brain regions including hippocampal subregions, medial septum, subiculum and entorhinal cortex, comparing different age groups and genotypes. We focused on this brain region because of its clear relationship with learning and memory and that the hippocampal formation shows clear neuropathological changes in human AD. Our results reveal alterations in the circuit connectivity of hippocampal CA1 in AD model mice. Overall, we find weaker extrinsic connectivity CA1 input strengths in AD model mice compared with control mice, including sex differences of reduced subiculum to CA1 inputs in aged female AD mice compared to aged male AD mice. Unexpectedly, we find a connectivity pattern shift with an increased proportion of inputs from the CA3 region to CA1 excitatory neurons when comparing young and old AD model mice, as well as old wild-type mice and old AD model mice. These unexpected shifts in CA3-CA1 input proportions in this AD mouse model suggest the possibility that compensatory circuit increases may occur in

response to connectivity losses in other parts of the hippocampal circuits. We expect that this work provides new insights into the neural circuit mechanisms of AD pathogenesis.

Introduction

Dementia and age-related cognitive decline are major health concerns worldwide. Alzheimer's disease (AD) is the most common form of age-progressive adult dementia. AD is characterized by distinguishable pathological features that include synaptic and neuronal loss, and age-progressive deterioration of cognitive function. In keeping with the original clinical observations of Alois Alzheimer, the longstanding focus in AD research has been the pathological accumulation of amyloid-beta (Aβ) protein fragments (Querfurth and LaFerla, 2010; Selkoe et al., 2004) and hyperphosphorylated tau protein (Kosik et al., 1986). Aβ results from aberrant cleavage of the amyloid precursor protein (APP) by β- and γ-secretases. Excessive Aβ production causes fibril aggregation that culminates in AD neuropathology (Hardy and Allsop, 1991; Hardy and Selkoe, 2002; Soria Lopez et al., 2019).

While the mechanistic basis of AD pathogenesis has been studied for many years, more recent evidence suggests that AD can be functionally characterized by the disruption of both long-range and local neural circuit connections (Busche et al., 2015; Geula, 1998; Harris et al., 2020; Jeon et al., 2018; Neuman et al., 2015; Palop et al., 2007; Palop and Mucke, 2010). Dil-based retrograde neural circuit tracing of the hippocampus (via bulk injection targeted in the dentate gyrus) in the 5xFAD mouse model qualitatively suggests decreased hippocampal connectivity between the medial septum and diagonal band (MS-DB), entorhinal cortex, auditory cortex, locus coeruleus, dorsal raphe, substantia nigra pars compacta, and olfactory bulb (Jeon et al., 2018). Hippocampal CA1, a brain region associated with spatial learning and memory, is one of the most vulnerable brain regions in AD (Andrade-Moraes et al., 2013; Hyman et al., 1990; Montero-Crespo et al., 2021; West et al., 2004). *In vivo* electrophysiological recordings in a single APP knock-in (APP-KI) AD mouse model reveals that hippocampal CA1 place cells exhibit spatial memory defects, including disrupted spatial remapping, due to deteriorated circuit connections between CA1 and entorhinal cortex (EC) in APP-KI mice (Jun et al., 2020). Miniscope-based calcium imaging of CA1 neurons in freely behaving triple-transgenic (3xTg) AD model mice shows spatial

encoding defects in CA1 circuit ensemble activities even preceding AD pathology and AD-related memory behavioral deficits (Lin et al., 2022).

In this study using monosynaptic rabies virus tracing, we measured local and global circuit connectivity to hippocampal CA1 excitatory neurons to test our hypothesis that these connections are altered in the single APP^{NL-G-F} KI AD mouse model (Saito et al., 2014). Recent advancements in viral-genetic-based retrograde tracing provide new opportunities for semi-quantitative mapping of cell-type-specific neural circuit connections (Sun et al., 2019; Sun et al., 2014; Wickersham et al., 2007; Xu et al., 2016). The genetically modified monosynaptic rabies virus tracing technique is useful for mapping the direct circuit inputs to specific types of neurons. We take advantage of the ability to target rabies infection to specific cell types using EnvA pseudotyping, and to limit trans-synaptic spread to direct inputs, by using glycoprotein gene-deleted (ΔG) rabies virus and transcomplementation. Specifically, ΔG rabies virus (deletion mutant) is pseudotyped with the avian sarcoma leucosis virus glycoprotein EnvA (EnvA RVΔG), which can only infect neurons that express avian tumor virus receptor A (TVA), an avian receptor protein that is absent in mammalian cells unless it is provided through secondary exogenous gene delivery. We use helper AAV to provide both TVA and rabies glycoprotein expression in CA1 excitatory cells. The deletion-mutant rabies virus (RVΔG) can then be transcomplemented with the rabies glycoprotein in the same TVA-expressing cells to enable its retrograde spread restricted to direct presynaptic neurons.

The mouse model used in this study is the APP^{NL-G-F} KI (knock-in) mouse line (Saito et al., 2014), with the knocked-in human APP gene with multiple mutations: Swedish (KM670/671NL), Beyreuther/Iberian (I716F) and Arctic mutations (E693G). There are interpretational advantages to using the knock-in approach: pathogenic Aβ levels are elevated in the APP^{NL-G-F} KI. Furthermore, potential APP overexpression artifacts are not an interpretational issue with this AD model mouse line. To examine age-related progression using APP^{NL-G-F} KI versus age-matched control mice, we studied littermate control wild-type mice that share the same genetic background and AD-like mice at two different ages (3-4 vs. 10-11 months old).

These ages were chosen based on previously established findings for behavioral performance defects and neuropathological features (Mehla et al., 2019; Saito et al., 2014). Our results show alterations in circuit connectivity of hippocampal CA1 in AD model mice, with overall weaker extrinsic connectivity strengths and connectivity pattern shifts in AD model mice compared with control mice.

Materials and Methods

Animals

All experiments were conducted according to the National Institutes of Health guidelines for animal care and use, and were approved by the University of California, Irvine Institutional Animal Care and Use Committee (IACUC, protocol #: AUP-20-002) and Institutional Biosafety Committee (IBC). To study the extrinsic CA1 excitatory circuit connections, the following two strains of mice were used: wild type (WT) C57BL/6J, the young group at age 3-4 months (n=7, 3 male, 4 female) and the old group at 8-11 months (n=10, 6 male, 4 female), and APP-knock in (APP-KI, strain APP^{NL-G-F}), the young group at 3-4 months (n=10, 5 male, 5 female) and the old group at 8-11 months (n=8, 5 male, 3 female). The mice had free access to food and water in their home cages with lights maintained on a 12-hour light/dark cycle. All personnel working with the rabies virus received rabies vaccinations and experiments were conducted under biosafety level (BSL) 2 conditions.

Viral injections

Mice were first anesthetized under 1-2% isoflurane for 10 minutes with a 0.8 L/min oxygen flow rate using an isoflurane tabletop unit (HME109, Highland Medical Equipment, Temecula, CA, USA). Their head fur was shaved, then mice were placed in a rodent stereotaxic frame (Leica

Angle Two™ for mouse, Leica Biosystems Inc., Buffalo Grove, IL, USA) and continuously anesthetized with isoflurane flow at 1%. After disinfection, a small incision was made in the skin, and the skull was exposed to show the landmarks of bregma and lambda. Guided by a digital atlas of the stereotaxic machine, a three-axis micromanipulator was used to locate the desired injection site relative to bregma and lambda. A small craniotomy was made above the injection site, exposing the dura.

A glass pipette (tip inner diameter, 20-30 μm) was loaded with virus solution, lowered to the target injection site, and the virus was delivered through picospritzer (Parker Hannifin, Hollis, NH, USA) pressure injection at the rate of 20-30 nl/min with a 10 ms pulse duration. After injection, the glass pipette remained at the injection site for 10 minutes and then was withdrawn at a constant slow speed to prevent the backflow of the virus. After mice were removed from the stereotaxic frame, their skin was sutured using tissue adhesive (3M Vetbond, St. Paul, MN, USA). Mice were injected with 5mg/kg Carprofen to mitigate pain and inflammation. Mice were put on a heating pad for 15 min and then back in their home cages. The virus was injected into the pyramidal layer of dorsal hippocampal CA1 using the following coordinates: anteroposterior (AP) -1.94 mm, mediolateral (ML) -1.40 mm, dorsoventral (DV) -1.35 mm, all values given relative to bregma.

To map the retrograde circuit connectivity of CA1, we used the following AAVs: AAV8-DIO-TC66T-2A-GFP-2A-oG (Salk Institute, CA, US, $5.06x10^{13}$ GC/ml) and AAV1-CaMKII-HI-eGFP-Cre-WPRE-SV40 (Addgene #105551, $1.76x10^{13}$ GC/ml). The AAV8-DIO-TC66T-2A-GFP-2A-oG was 1:4 diluted with phosphate-buffered saline (PBS). The diluted AAV was 1:1 mixed with AAV1-CaMKII-HI-eGFP-Cre-WPRE-SV40. This mixture was then further diluted at a 1:4 ratio with PBS. Finally, 0.1 μl of the diluted AAV mixture was injected into the hippocampal CA1 target region on day 1. After 17 days, the mice were injected with the rabies virus EnvA-SADΔG-RV-DsRed (lab-made, $2.1x10^{9}$ IU/ml, 0.4 μl) at the same injection site using pressure injection. Rabies virus was made locally at the Center for Neural Circuit Mapping Center (CNCM) of the University

of California, Irvine, with required cell lines and seeding viruses originally from Edward Callaway's group at the Salk Institute for Biological Studies. The rabies virus was allowed to replicate and retrogradely spread from targeted Cre+ cell types to directly connected presynaptic cells for 9 days before the mice were perfused for tissue processing.

Histology and Immunochemistry

The mice were perfused with 20 ml of PBS, followed by 40 ml PBS containing 4% paraformaldehyde (PFA) using a mini-pump with variable flow (United States Plastic Corp., US). The perfused brains were fixed in 4% PFA solution for 24 hours and then soaked in a 30% sucrose-PBS solution for another 24 hours at 4°C. Then the brains were frozen in dry ice and coronally sectioned at 30 µm thickness using a microtome (Leica SM2010R, Germany). One out of every three consecutive sections were mounted, coverslipped, and imaged. To examine the expression of amyloid-beta, two sections from each of five brains from each mouse group (10 sections in total for each mouse group) were stained with primary antibody 6E10 (Biolegend, Mouse, #803002,1:500 dilution, US), followed by Cy3 conjugated donkey anti-mouse secondary antibody (Jackson ImmunoResearch, 1:200 dilution, US). All sections were counterstained with 10 µM DAPI. Images were acquired by an automated fluorescent slide scanner (Olympus VS120-S6 slide scanner, Japan) using a 10x magnification objective. For higher resolution imaging, selected slices were imaged using a confocal microscope (Olympus FLUOVIEW FV3000, Japan) with a 40x magnification objective.

Data quantification and statistics

The amyloid plaque number and area and the CA1 area or field of view (FOV), were quantified unbiasedly using the 2-point circle measurement tool in Olympus VS-ASW software (Olympus, Japan). The plaque intensity was measured using the mean gray value measurement

tool in Fiji ImageJ. Two samples from each mouse brain were quantified. The two measurements were averaged for each brain for statistical comparison.

For rabies tracing experiments, we followed the established counting protocol in the previous publication (Sun et al., 2014). We first selected the brain section with the target region, CA1 to identify EGFP and DsRed doubled-labeled starter neurons that are restricted to CA1. All the starter cells were manually counted using the counting tool in Adobe Photoshop (Adobe, San Jose, CA, US). Next, we aligned the rest of the viral-infected brain sections with a standard Allen mouse brain atlas (http://atlas.brain-map.org/atlas) to determine the anatomical structures for the quantification of labeled cells in specified brain regions. No stereological measurement protocol was used; all labeled cells in each section of the brain section series (i.e., 1 out of every 3 sections was mounted for examination of virally labeled neurons in different brain structures) were counted. We operationally defined the input connectivity strength index (CSI) as the ratio of the number of presynaptic neurons in a brain region versus the number of starter neurons in the CA1 region. The CSI values allow us to quantitatively compare how input strengths from different brain regions to CA1 excitatory neurons. We calculated the proportion of inputs (PI) index as the ratio of the number of labeled presynaptic neurons in a brain region of interest versus the overall total labeled neurons in each case.

The anterior to posterior (AP) CSI distribution curve was plotted to show the input pattern across the AP axis within mouse brains. For each mouse, an input neuron value is counted for every brain slice, which corresponds to an AP number (relative to bregma) according to the standard Allen mouse brain atlas (http://atlas.brain-map.org/atlas). For all mice within the same age/genotype group, the CSI values were registered to similar AP numbers.

All data are presented as the mean ± SE. We applied appropriate statistical tests, and the data analysis was conducted using GraphPad Prism (GraphPad Software, San Diego, CA, USA) or MATLAB scripts. Statistical analysis methods included the Wilcoxon rank-sum test, paired Wilcoxon rank sum test, and linear mixed effects model (LME) (Yu et al., 2022). Alpha levels of

p≤0.05 were considered significant. Different levels of statistical significances are represented by * p<0.05, ** p<0.01, *** p<0.001, **** p<0.0001.

Results

Age-progressive amyloid-beta deposition in CA1 of APP-KI mice

To detect the level of Aβ plaques in age-matched APP-KI and WT mice, we stained coronal brain sections with the 6E10 Aβ monoclonal antibody (Kim et al., 1988) and performed plaque quantification (Fig.1). Two age groups of mice were selected, at 3-4 months old (young group), in which the plaque early formation can be detected in APP^{NL-G-F} KI mice, and at 10-11 months (old group), for which cognitive defects are observed in APP^{NL-G-F} KI mice at this age (Saito et al., 2014). Half brain sections with autofluorescence in the red channel reveal distinct plaque patterns in APP-KI young and old mice hippocampus and cortex, even in the absence of immunostaining (Fig.1A). Aβ antibody 6E10 immunostained CA1 images show extensive amyloid plaques in APP-KI mice at greater resolution (Fig. 1A). There are significantly more 6E10-stained plaques in APP-KI old brains relative to APP-KI young brains, consistent with the age-progressive nature of AD. In contrast, no 6E10-immunopositive plaques are detected in WT young and old mice. Quantitative plaque analysis of 6E10 staining shows that APP-KI old mice have both significantly higher plaque density and stronger plaque immunofluorescence intensity in hippocampal CA1 relative to young APP-KI mice (Fig. 1B and D; density, APP-KI young: 654.3±94.9, APP-KI old: 1339±81.3, Wilcoxon rank-sum test, $p=2.0x10^{-4}$; intensity, APP-KI young:1057 ±27.4, APP-KI old: 1254±18.9, linear mixed effects model, p= 0.045573). No significant differences in plaque size are detected between the two ages of APP-KI mice (Fig. 1C). These results show age-progressive Aβ pathology development in APP-KI mice, consistent with the earlier reports (Saito et al., 2014).

Monosynaptic rabies tracing in age-matched APP-KI and control mice and overall compromised brain-wide connectivity in APP-KI mice

We focused on mapping hippocampal CA1 excitatory neurons because these cells operate as place cells and are directly relevant to spatial mapping behaviors that are impaired during AD progression (Soltesz and Losonczy, 2018). To map the global and local neural circuit connections of CA1 excitatory neurons in AD mice, we performed Cre-dependent monosynaptic rabies tracing in age-matched young and old APP-KI and WT mice as shown schematically (Fig. 2A). The rabies tracing experiment was performed at 3-4 months and 10-11 months old as specified above (Fig. 1). A mixture of helper AAVs (AAV-DIO-TC66T-GFP-OG and AAV CaMKIIα -EGFP-Cre virus) was injected at the pyramidal layer of hippocampal CA1 in the left hemisphere of mouse brains for each age and genotype noted above. The Cre-dependent AAV helper (AAV-DIO-TC66T-GFP-oG) expresses TC66T, a variant of tumor virus receptor A (TVA) which acts as a high specific target that facilitates rabies infection, and optimized glycoprotein (oG), thus optimizing rabies virus infection (Miyamichi et al., 2013). The Cre recombinase under the CaMKIIα promoter AAV (AAV-CaMKIIα-EGFP-Cre) directs the expression of Cre recombinase to CaMKIIα positive excitatory neurons. The combination of DIO (double-floxed inverted open reading frame) and Cre provided by the two AAVs restrict TC66T and oG expression in CaMKIIα positive excitatory neurons. At 17 days after the primary AAV helper viral injection, the EnvA pseudotyped G deleted rabies virus (EnvA-SADΔG-DsRed) was delivered at the same injection site as the AAV injection (Fig. 2A) as guided by stereotaxis coordinates. Mouse brains were harvested 9 days after the second injection for sectioning and further histological processing. Following the monosynaptic rabies virus tracing from CA1 starter neurons, the input-mapped presynaptic neurons are primarily located in the MS-DB, hippocampal CA1, CA2, CA3, SUB, and entorhinal cortex (EC), as shown in the schematic (Fig. 2B). To compare potential connectivity differences between young WT and APP-KI mice, brain-wide coronal brain sections in WT young and APP-KI young mice were imaged and quantified. The overall numbers of presynaptic neurons were

quantified and normalized by the total starter neurons of each case; the resultant brain-wide overall connectivity was compared across the groups of mice. The expression of the rabies virus (EnvA-SADΔG-RV-DsRed) is visualized with DsRed, and the expression of the helper AAV is visualized with EGFP. While presynaptic neurons are only labeled with DsRed from the RV gene expression, the starter cells can be unambiguously identified by their EGFP and DsRed expression from both the helper AAV and ΔG-DsRed rabies virus (Figure 3A; Figure 4A). APP-KI young mice (n=10) show significantly weaker brain-wide overall connectivity relative to WT young mice (n=7) (WT young: 22.10±1.97, APP-KI young: 14.41±0.72, Wilcoxon rank-sum test, $p=2.0x10^{-3}$). Similarly, APP-KI old mice (n=8) also show weaker overall connectivity relative to WT old mice (n=10) (Fig. 2C) (WT old: 21.01±2.14, APP-KI old: 14.36±1.92, Wilcoxon rank-sum test, $p=3.40x10^{-2}$). Our data indicate that the CA1 excitatory neurons input connections in APP-KI mice show compromised brain-wide connectivity and they are overall weaker relative to those of age-matched WT mice.

Regional-specific tracing results in age-matched young and old WT and APP-KI mice

To map and compare regional-specific presynaptic inputs to CA1 excitatory cells in WT young, APP-KI young, WT old and APP-KI old mice, representative coronal sections of ipsilateral and contralateral hippocampal formations, injection sites and presynaptic inputs regions are imaged and quantified (WT young: Fig. 3A and B; APP-KI young: Fig. 3C and D; WT old: Fig. 4A and B; APP-KI old: Fig. 4C and D). Neurons labeled with both red (DsRed) and green (GFP) fluorescence signals represent the robust labeling of starter neurons (Fig. 3A and C, Fig. 4A and C, panel 3) and their numbers are used as the denominators for semi-quantitative connectivity strength measurements. Neurons labeled with DsRed only are the presynaptic inputs of starter neurons. For both WT and APP-KI mice, the prominent input regions to excitatory CA1 pyramidal neurons include the medial septum-diagonal band (MS-DB) complex, CA3 and CA2 pyramidal

(Py) layer, SUB, and EC (Fig. 3A and C, Fig. 4A and C, panel 1-10). Other CA1 excitatory neuron inputs include putative inhibitory interneurons located in the oriens (Or), radiatum (Rad) and lacunosum moleculare (Lmol) layer of hippocampal CA1, CA2 and CA3, as well as median raphe, paramedian raphe (MnR/PMnR), and sparse labeling in nucleus reuniens. The greatest input density comes from the ipsilateral side of the brain, but robust contralateral inputs can be detected from hippocampal subregions: CA1-3 (Fig. 3A and C, Fig. 4A and C).

To investigate the distribution of CA1 circuit inputs along the anterior-to-posterior axis in the brain for WT young, APP-KI young, WT old and APP-KI old, the input connectivity strengths index measurements of selected presynaptic input regions are plotted across AP locations of individual brain sections. The brain regions include MS-DB, SUB, EC, ipsilateral CA1 oriens layer, ipsilateral CA2 pyramidal layer and ipsilateral CA3 pyramidal layer (Fig. 3B and D, Fig. 4B and D). CA1 excitatory cells in the four groups of mice show an overall similar distribution pattern of regional inputs, with MS-DB accounting for the most anterior position, followed by the hippocampal formation, including CA1, CA2, CA3, SUB, and finally entorhinal cortex, moving progressively more posteriorly.

To semi-quantitatively compare the connectivity strength of CA1 excitatory neurons in age-matched WT and APP-KI mice, the presynaptic input neurons and starter neurons were identified and counted throughout each brain. To determine semi-quantitative normalized neural connectivity, the connectivity strength index (CSI) was calculated for each pair of connected brain subregions, represented by the number of neurons within a specific subregion over the total number of starter neurons in each case.

As seen in the plots of all four groups of mice tested, there is a sharp peak of CA3 input strength in the CA3 locations anterior to the CA1 injection site, as the anatomical structure of CA3 starts more anterior as compared to CA1 (Fig. 3B and D, Fig. 4B and D). Among these regions, the ipsilateral CA3 Py layer provides the greatest number of inputs, as shown by the largest area-under-curve. However, there is a significant decrease in area-under-curve for both MS-DB (WT

young vs APP-KI young, p=0.0002; WT old vs APP-KI old, p=0.0001; paired Wilcoxon rank sum test) and ipsilateral CA1 Oriens inputs (WT young vs APP-KI young, p<0.00001; WT old vs APP-KI old, p=0.0012; paired Wilcoxon rank sum test) inputs in APP-KI mice compared to WT mice for both age groups.

As expected, the majority of CA1 retrograde connections originate within the hippocampal formation. Overall, ipsilateral hippocampal inputs are much more abundant relative to contralateral inputs (Fig. 5; Tables 2.1 and 2.2). For all contralateral inputs, the contralateral CA3 pyramidal layer has the highest density of inputs, indicating a strong commissural CA3 to CA1 pathway. Detailed statistical comparisons between the four groups of mice reveal significant CSI differences (Fig. 4, Tables 2.1 and 2.2). Comparing age-matched WT and APP-KI mice, ipsilateral CA1 Or, ipsilateral CA2 Py, ipsilateral CA2 Or and MS-DB of the APP-KI young group all show significantly weaker input connections to excitatory CA1 neurons relative to the WT young group (Fig. 5A) (Wilcoxon rank-sum test, $p=4.11x10^{-4}$, $p=4.11x10^{-4}$, $p=1.36x10^{-2}$, $p=1.03x10^{-4}$, respectively). The CSI values of WT young group are 1.281±0.172 (CA1_Or_ipsi), 1.329 ±0.086 (CA2_Py_ipsi), 0.107±0.029 (CA2_Or_ipsi), 1.011±0.087 (MS-DB); the CSI values of APP-KI young group are 0.626 ±0.041 (CA1_Or_ipsi), 0.763±0.062 (CA2_Py_ipsi), 0.037±0.007 (CA2_Or_ipsi), 0.640±0.024 (MS-DB). For comparison between the two old age groups, APP-KI old mice show significantly smaller CSI values in contralateral CA1 Py, contralateral CA2 Py and MS-DB compared to WT old mice (Fig. 5B) (Wilcoxon rank-sum test, $p=2.64x10^{-2}$, $p=1.17x10^{-2}$, $p=1.55x10^{-2}$, respectively). The CSI values of WT old group are 0.211±0.073 (CA1_Py_contra), 0.206±0.040 (CA2_Py_contra), 1.220±0.180 (MS-DB); the CSI values of APP-KI old group are 0.031±0.012 (CA1_Py_contra), 0.076±0.013 (CA2_Py_contra), 0.638±0.090 (MS-DB). In terms of comparison within the same genotype but at different ages, WT young and WT old groups show a significant difference at contralateral CA1 Py (Fig. 5C) (Wilcoxon rank-sum test, $p=2.34x10^{-2}$). Their CSI values are 0.511±0.112 (WT young group) and 0.211±0.073 (WT old group), showing decreased connectivity in old WT mice. Age-related

connectivity differences are more frequently observed in APP-KI mice. For APP-KI young and APP-KI old, contralateral CA1 Py, contralateral CA2 Py and contralateral CA3 Py all show significantly weaker connections in APP-KI old relative to APP-KI young (Fig. 5D) (Wilcoxon rank-sum test, $p=4.6x10^{-5}$, $p=1.55x10^{-2}$, $p=4.34x10^{-2}$, respectively). The CSI values of APP-KI young group are 0.370±0.046 (CA1_Py_contra), 0.198±0.040 (CA2_Py_contra), 2.103±0.257 (CA3_Py_contra); the CSI values of APP-KI old group are 0.031±0.012 (CA1_Py_contra), 0.076 ±0.013 (CA2_Py_contra), 1.287±0.200 (CA3_Py_contra). Unexpectedly, there is an increase in CSI value of the ipsilateral CA1 oriens layer when comparing APP-KI young vs APP-KI old. Their CSI values are 0.626±0.041 (APP-KI young group) and 0.947±0.152 (APP-KI old group). Together, these data support significant alterations in presynaptic connectivity strength to CA1 excitatory neurons in APP-KI mice compared to WT mice. Moreover, these connectivity alterations show age-progressive features, in WT and especially in APP-KI mice.

Quantitative analysis of the regional-specific proportions of CA1 excitatory cell input pattern

To investigate whether the CA1 input connectivity patterns shift in APP-KI mice with their overall reduced connectivity, we measured the proportion of inputs (PI) index based on the proportion of each input region for the total inputs (Fig. 6). The PI index is represented by the fraction of presynaptic neurons in each input region over the entire brain inputs and provides a more global measure of connectivity contribution for a given region. For comparison between WT young and APP-KI young mice, the APP-KI young group shows significantly lower PI values in the ipsilateral CA1 oriens layer, ipsilateral CA2 pyramidal layer, ipsilateral CA2 oriens layer, MS-DB (Fig. 6A) (Wilcoxon rank-sum test, $p=4.63x10^{-3}$, $p=4.11x10^{-4}$, $p=1.85x10^{-2}$, $p=2.50x10^{-2}$, respectively). The PI values of WT young group are 0.113±0.017 (CA1_Or_ipsi), 0.117±0.014 (CA2_Py_ipsi), 0.010±0.004 (CA2_Or_ipsi), 0.087±0.007 (MS-DB); the PI values of APP-KI

young group are 0.067±0.009 (CA1_Or_ipsi), 0.078±0.005 (CA2_Py_ipsi), 0.004±0.001 (CA2_Or_ipsi), 0.067±0.004 (MS-DB). In contrast, the contralateral CA3 pyramidal layer shows significantly higher PI for young APP-KI mice relative to young WT mice (Fig. 6A) (Wilcoxon rank-sum test, $p=1.95x10^{-3}$). The PI value of the WT young group is 0.123±0.013 (CA3_Py_contra) and the PI value of the APP-KI young group is 0.202±0.013 (CA3_Py_contra). The unexpected increase in hippocampal connectivity might reflect compensatory increases in parts of the hippocampal formation in response to circuit input decreases in other parts of the hippocampus. For comparisons between WT old and APP-KI old groups, APP-KI old group shows lower PI values in the contralateral CA1 pyramidal layer, contralateral CA2 pyramidal layer, MS-DB and SUB (Fig.6B) (Wilcoxon rank-sum test, $p=3.39x10^{-2}$, $p=2.66x10^{-2}$, $p=1.17x10^{-2}$, $p=1.55x10^{-2}$, respectively). The PI values of the WT old group are 0.016±0.005 (CA1_Py_contra), 0.016±0.003 (CA2_Py_contra), 0.101±0.009 (MS-DB), 0.061±0.007 (SUB); the PI values of the APP-KI old group 0.004±0.002 (CA1_Py_contra), 0.008±0.001 (CA2_Py_contra), 0.066±0.007 (MS-DB), 0.034±0.006 (SUB). In contrast, the ipsilateral CA3 pyramidal layer is higher in APP-KI old group than WT old group (Fig. 6B) (Wilcoxon rank-sum test, $p=1.37x10^{-3}$). Their PI values are 0.389±0.023 (CA3_Py_ipsi, WT old group) and 0.504±0.014 (CA3_Py_ipsi, APP-KI old group). A significant difference was observed in the comparison between WT young and WT old, where the PI value of contralateral CA1 pyramidal layer is smaller in WT old relative to in WT young group (Fig. 6C) (WT young: 0.042±0.010, WT old: 0.016±0.005, Wilcoxon rank-sum test, $p=1.36x10^{-2}$). Unexpectedly, for age-related comparison between APP-KI young and APP-KI old, the inputs from ipsilateral CA1 oriens layer, ipsilateral CA2 pyramidal layer, and ipsilateral CA3 pyramidal layer all show higher PI values in the APP-KI old group (Fig. 6D) (Wilcoxon rank-sum test, $p=2.06x10^{-3}$, $p=3.06x10^{-3}$, $p=3.2x10^{-4}$, respectively). The PI values of APP-KI young group are 0.067±0.009 (CA1_Or_ipsi), 0.078±0.005 (CA2_Py_ipsi), 0.438±0.006 (CA3_Py_ipsi); the PI values of APP-KI old group are 0.107±0.011 (CA1_Or_ipsi), 0.112±0.008 (CA2_Py_ipsi), 0.504±0.014 (CA3_Py_ipsi). By comparison, the contralateral CA1 pyramidal layer, contralateral

CA2 pyramidal layer, contralateral CA3 pyramidal layer, SUB, and MnR/PMnR all show lower proportions of inputs in the APP-KI old group (Fig. 6B) (Wilcoxon rank-sum test, $p=4.6x10^{-5}$, $p=6.22x10^{-3}$, $p=3.06x10^{-3}$, $p=3.06x10^{-3}$, $p=8.48x10^{-3}$, respectively). The PI values of APP-KI young group are 0.037±0.004 (CA1_Py_contra), 0.018±0.003 (CA2_Py_contra), 0.202±0.013 (CA3_Py_contra), 0.057±0.003 (SUB), 0.0027±0.0003 (MnR/PMnR); the PI values of APP-KI old group are 0.004±0.001 (CA1_Py_contra), 0.008±0.001 (CA2_Py_contra), 0.128±0.008 (CA3_Py_contra), 0.034±0.006 (SUB), 0.0011±0.0004 (MnR/PMnR). Together, these data support the idea that compensatory circuit input changes may occur in response to connectivity losses in AD conditions.

Sex differences in connectivity strength and pattern to CA1 excitatory neurons

In human patients, AD is more common in females than males on an age-matched basis (Seshadri et al., 1997). We asked whether sex differences in CA1 neuron connectivity strength and patterns may be recapitulated in the AD mouse model. The CSI and PI values were compared between male and female mice for each group pair. Notably, for both CSI and PI, aged female APP-KI mice show significant connectivity defects for the SUB to CA1 projection as compared to aged male APP-KI mice (Wilcoxon rank-sum test, CSI $p=3.6x10^{-2}$, PI $p=3.6x10^{-2}$), while no significant differences are detected for other input regions when comparing between sexes. These results indicate that the circuit connections to CA1 excitatory neurons from different brain regions may be differentially impacted by sex-related factors.

Discussion

In this study, we applied monosynaptic rabies tracing approach to investigate alterations in input circuit connectivity of hippocampal CA1 excitatory neurons in age-matched WT and APP-KI mice. As immunostaining results show age-progressive amyloid deposition in hippocampal

CA1 in APP-KI mice, our monosynaptic rabies virus tracing reveals pathological impairments of excitatory CA1 cell input connectivity. We map the local and long-range presynaptic inputs to CA1 excitatory neurons from multiple brain regions in age-matched WT and APP-KI mice groups at young and old ages. Compared to WT mice, AD mice show an overall impaired hippocampal CA1 circuit connectivity. Our results show age-progressive and reduced hippocampal CA1 connectivity strength in APP-KI mice compared to WT mice, as well as interesting connectivity patterns shifts with different hippocampal regions.

Quantification of the WT and APP-KI mice in young and old age groups reveals age-associated AD circuit change in both long-range and local brain regions. For example, presynaptic inputs from MS-DB in APP-KI mice compared to WT mice are weaker in both age groups. MS-DB is an essential modulator of hippocampal activity (Roland et al., 2014). Accumulating evidence shows that the septal regions are involved in AD. Cholinergic neurons in MS are found to decrease substantially in AD patients and cholinergic innervations to the hippocampus are severely impacted (Hampel et al., 2018; Nelson et al., 2014; Takeuchi et al., 2021). Previous CA1 excitatory studies show that most of the rabies-labeled septohippocampal cells were cholinergic (Sun et al., 2014). The decrease of MS-DB to CA1 excitatory neuron connectivity revealed by monosynaptic rabies tracing may reflect a cholinergic neural associated connectivity strength decrease in AD mice.

It is noteworthy that local intrahippocampal connectivity changes with genotype and age. Surprisingly, the connectivity strength proportional pattern of CA3 pyramidal neurons is significantly larger in APP-KI old mice relative to WT old mice and is also higher in APP-KI old mice compared to APP-KI young mice. Similarly, there is a trend of increase in CA3 to CA1 connectivity in APP-KI young when compared to WT young group (Fig. 6A). The major connections to CA1 excitatory neurons originate from the CA3 pyramidal neurons. While the absolute connectivity strength (CSI) of CA3 pyramidal neurons to CA1 excitatory neurons shows no significant difference when comparing different ages and genotypes, the proportional input

pattern shifts significantly in APP-KI compared to WT mice. This raises the interesting possibility that there may be a compensatory effect of CA1 neural plasticity during APP progression. A previous study has shown that DG to CA3 GABAergic transmission and feedforward inhibition is reduced in CA3 pyramidal neurons of APP/PS1 mice (Viana da Silva et al., 2019). CA1 neurons receive robust information from CA3 neurons through the trisynaptic pathway. It is possible that the decrease of DG-CA3 inhibition leads to the hyperexcitation of CA3 neurons, and further contributes to the enhancement of the CA3 to CA1 pathway. Moreover, *in vivo* electrophysiological study discovered that APP-KI mice exhibit disrupted spatial remapping of CA1 place cells (Jun et al., 2020). Their results suggest that MEC→CA1 signal transfer via fast gamma oscillations is deteriorated in APP-KI mice, whereas slow gamma-mediated CA3→CA1 signal transfer remains relatively intact. The compromised remapping of CA1 neurons may indicate a potential differential impact on EC-CA1 and CA3-CA1 neural communication. We also note that the connectivity strength between contralateral CA1 pyramidal neuron inputs to ipsilateral CA1 excitatory neuron decreases in aged groups. This may reflect an age-dependent progressive deterioration of commissural inputs.

The age-progressive Aβ deposition in CA1 and the overall compromised connectivity of CA1 neurons in APP-KI mice, together, indicate that Aβ level may be associated with attenuated synaptic connections, as synaptic loss is a hallmark of AD. Increasing evidence has shown that Aβ deposition affects both local and long-range circuit connections in the brain. At the very early stage of the disease, Aβ induces neuron hyperactivity and excitatory/inhibitory imbalance by decreasing inhibitory GABAergic function (Busche et al., 2008) and causes glutamate accumulation near the synapse (Zott et al., 2019). As the disease progresses, the prolonged Aβ depositions further reduce glutamatergic synaptic transmission and lead to synaptic loss (Calvo-Rodriguez and Bacskai, 2021; Palop and Mucke, 2010). Three-dimensional analysis of hippocampal CA1 brain samples from AD human postmortem tissue shows that the total number of synapses is reduced at the early stages of AD, and this reduction progressively increases in

severity during the late stage of the disease (Montero-Crespo et al., 2021). This age-related synaptic deterioration has functional implications. *In vivo* two-photon Ca^{2+} imaging of hippocampal CA1 in an AD model mouse reveals that in the vicinity of plaque, CA1 pyramidal neuron activity is profoundly impacted, especially in aged AD mice (Busche et al., 2012). These earlier relevant functional and physiological studies support the potential functional consequences of AD-impacted neural circuit connectivity in hippocampal CA1 in our present study.

Our results also indicate sex differences in neural circuit connectivity to hippocampal CA1 in AD model mice, as more severe SUB-CA1 projection defects are found in female old APP-KI mice than in the male. This result is consistent with the well-established finding that there is a two-fold increased risk in women versus men (Seshadri et al., 1997). As the SUB-CA1 connections have been implicated in object-location memory (Sun et al., 2019) and loss of object location memory is one of the key impairments in Alzheimer's disease, our new finding in hippocampal sub-circuit mechanisms may provide an intriguing new target to counteract AD-related memory impairments.

The method of rabies labeling is sensitive and reliable, because labeled cells are seen in very distant structures such as the MS-DB area and other areas that are known to project weakly to hippocampal CA1. However, we do not expect this method to label every input to each neuron with 100% efficiency. The connectivity from EC to CA1 measured in this study is relatively sparse compared to earlier studies with bulk tracer injections with no quantitative measurements of project strengths. Note that our rabies viral tracing approach offers an important technical advantage so that we can semi-quantitatively assess the relative number of inputs from each source to each target cell type, and quantify the number of cells that are labeled at various input locations, thus providing weighted connection strengths for defined cell types. The EC-CA1 connectivity strength index (CSI) value measured in this study is CSI=0.034 ±0.011 for WT young group (n=7, 3-4 months), and CSI=0.052 ±0.022 for WT old group (n=10, 8-11 months). These values are comparable to the CSI value reported in a previous CA1 excitatory neuron rabies

tracing study (Sun et al., 2014). Since we are quantitatively investigating the circuit connectivity differences between WT and APP-KI mice at young and old ages using the same experimental strategy, the results for comparison across different groups are reliable, and are supported in general based on our earlier published results.

Together, our research showing the connectivity strength alterations and connectivity pattern shifts in APP-KI AD mice may provide insights for tackling AD at the neural circuit level. Future neural circuit studies may lead to improved therapeutic interventions that slow down or counteract this disease at an early stage in AD patients.

Conclusions

In conclusion, we applied Cre-dependent monosynaptic rabies tracing to study the circuit connectivity changes of hippocampal CA1 excitatory neurons in age-matched WT and APP-KI mice. Using semi-quantitative analysis, we identify age-progressive connectivity strength changes of CA1 neurons in AD model mice. Interestingly, our data show compensatory changes in CA3-CA1 connectivity patterns in AD model mice, as well as sex differences in SUB-CA1 connections.

Acknowledgments

The breeders of APP-KI mice used in this study were provided by the RIKEN BRC through the National Bio-Resource Project of the MEXT, Japan. This work is supported by NIH grants (RF1AG065675; RF1MH120020 to X.X.). T.C.H. is funded by R35 GM127102.

Funding

This work is supported by NIH grants (RF1AG065675; RF1MH120020 to X.X.). T.C.H. is funded by R35 GM127102.

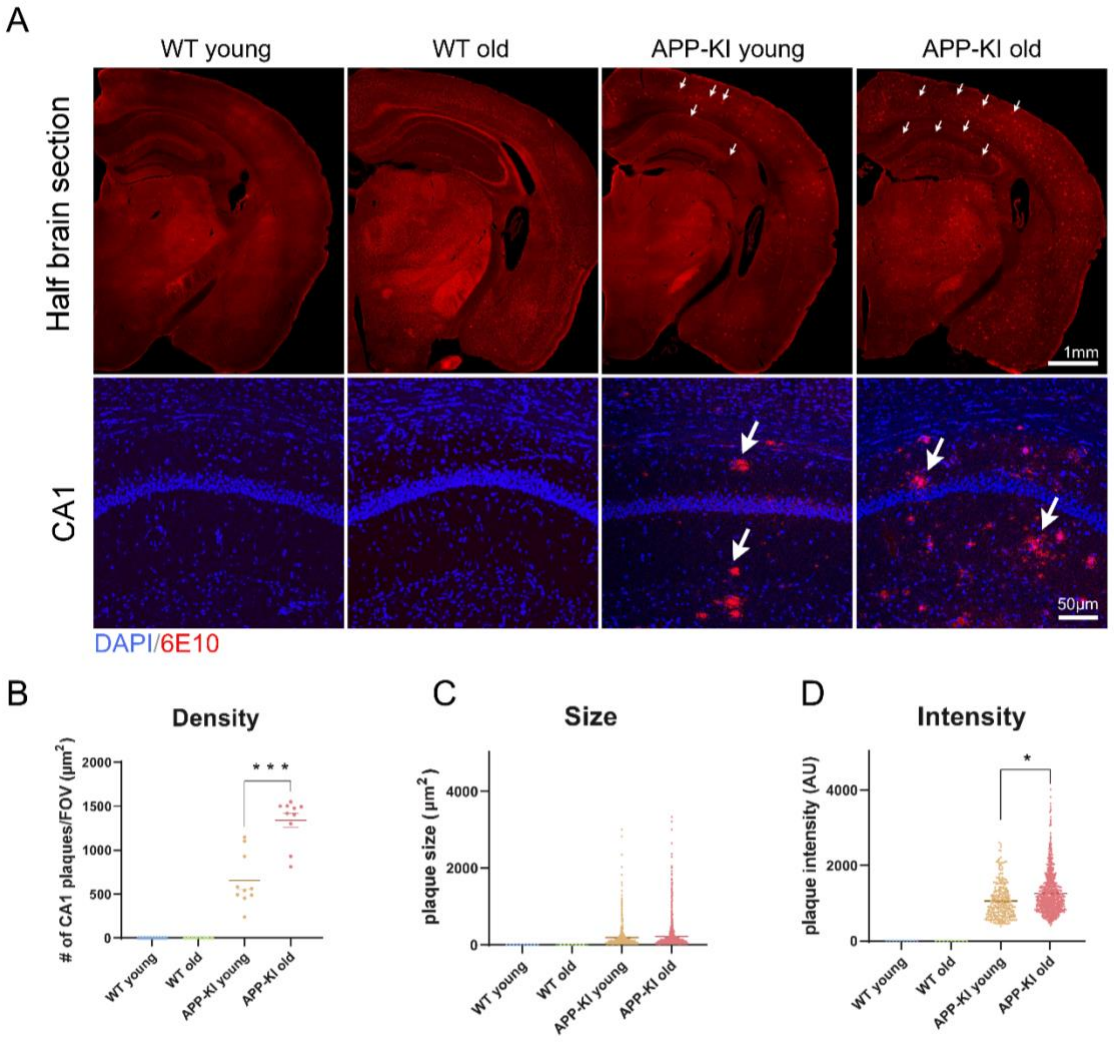

Figure 2.1 Age-progressive Aβ neuropathology in APP-KI mice

***A*,** Representative images of amyloid plaques in age-matched young and old APP-KI and WT mice. The upper four panels show half coronal brain sections in red channel autofluorescence without immunostaining. The bottom four panels depict enlarged views of 6E10 amyloid antibody immunostained hippocampal CA1 slices. White arrows point to the amyloid plaques in brain slices prepared from APP-KI young and APP-KI old mice. No plaques are detected in WT young and old. More amyloid deposits are detected in APP-KI old mice relative to APP-KI young mice. DAPI is labeled blue, amyloid plaque is labeled red. Scale bars are labeled on figure panels. ***B-D*,** Quantification of amyloid plaques stained by 6E10 antibody. No amyloid plaques are found in either WT young or old mice, but in APP-KI mice there is a significant age-dependent increase in both plaque density and intensity (B, density, APP-KI young: 654.3±94.9, APP-KI old: 1339±81.3, Wilcoxon rank-sum test, $p=2.0x10^{-4}$; D, intensity, APP-KI young:1057 ±27.4, APP-KI old: 1254±18.9, linear mixed effects model, p= 0.045573). C, no significance is detected in plaque size measurement. Two brain sections from every 5 mice in each group of mice were used for quantification. AU: arbitrary unit. * p<0.05, ** p<0.01, *** p<0.001.

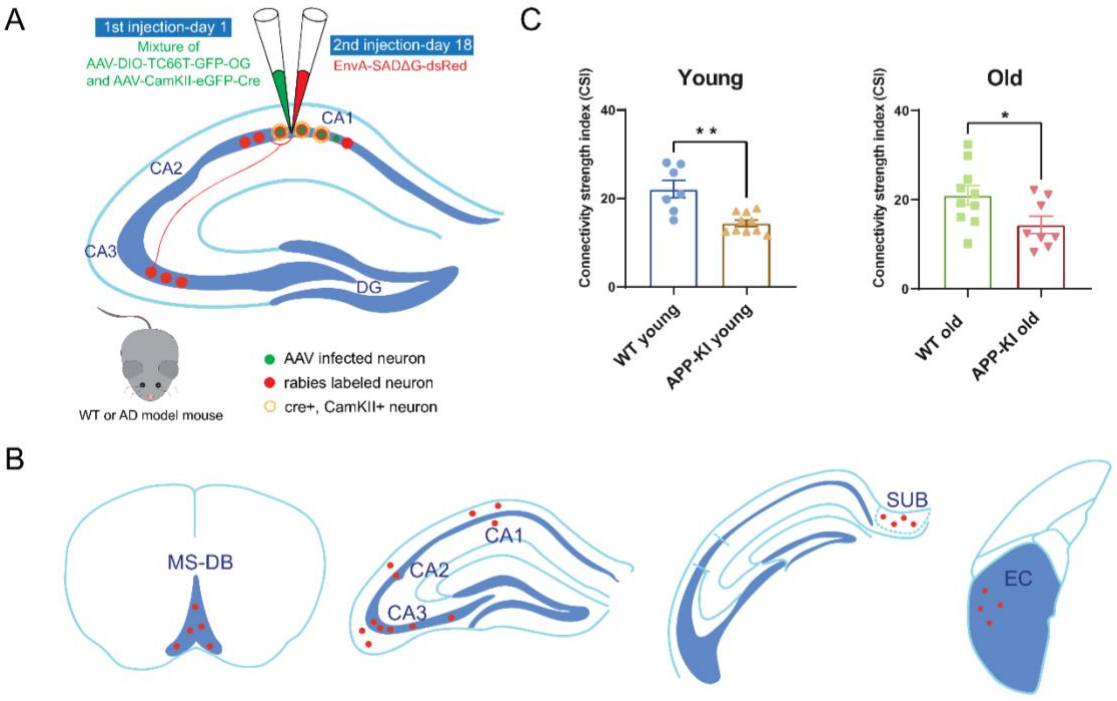

Figure 2.2 Cre-dependent monosynaptic rabies tracing reveals overall reduced circuit connectivity in APP-KI mice

***A*,** Schematic of cell-type-specific retrograde monosynaptic rabies tracing. To specifically label excitatory CA1 neurons, AAV helper virus (AAV-DIO-TC66T-GFP-OG and AAV-CaMKII-eGFP-Cre), labeled green, was injected into the dorsal hippocampal CA1 pyramidal layer, followed by 17 days later at the same site by an injection of rabies virus (EnvA-SADG-DsRed), labeled red. The neurons labeled both green and red represent the starter neurons. The neurons labeled red only represent the presynaptic inputs to the starter neurons. ***B*,** Major input regions to CA1 pyramidal layer excitatory neurons, including MS-DB, CA1, CA2, CA3, SUB, and Ent. Red color labels represent presynaptic input neurons. ***C*,** Overall connectivity revealed by monosynaptic rabies tracing. Left to right, wild type and APP-KI mice at young and old age. Connectivity strength is determined by the overall number of labeled neurons in the whole brain divided by the total number of starter neurons. APP-KI young mice (n=10) have significantly less connectivity strength compared to WT young mice (n=7) (WT young: 22.10±1.97, APP-KI young: 14.41±0.72, Wilcoxon rank-sum test, $p=2.0x10^{-3}$). APP-KI old mice (n=8) have significantly less connectivity strength relative to WT old mice (n=10) (WT old: 21.01±2.14, APP-KI old: 14.36±1.92, Wilcoxon rank-sum test, $p=3.40x10^{-2}$).

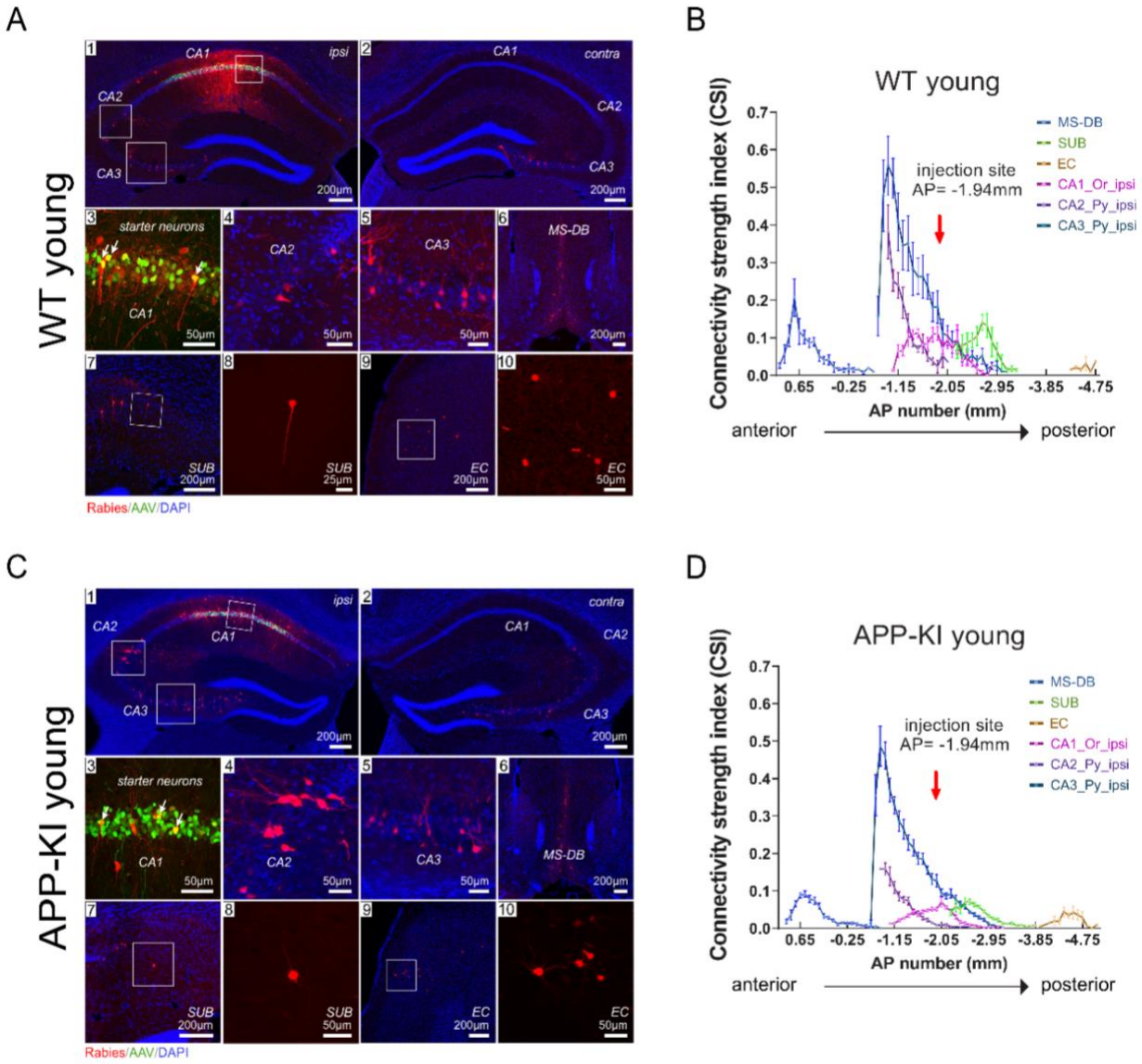

Figure 2.3 Monosynaptic rabies tracing maps specific regional inputs to excitatory CA1 cells along the anterior-posterior (AP) axis in young WT and APP-KI mice

A*, *C*,** Representative fluorescent coronal section images from WT young (n=7) and APP-KI young (n=10), respectively. Rabies virus-infected neurons are labeled by DsRed, and AAV-infected neurons are in green. All slices are counterstained by DAPI in blue. For both **A** and **C**, (1) shows the ipsilateral (ipsi) hippocampal formation including the CA1 injection site. (2), rabies virus mapped presynaptic inputs in the contralateral (contra) hippocampus. (3), enlarged image of CA1 starter neurons expressing both EGFP and DsRed fluorescent proteins from AAV and rabies virus. For both **A** and **C** (4-10), results of rabies virus-mediated retrograde monosynaptic tracing from CA1. The input regions include hippocampal CA2 (4), CA3 (5), medial septum and diagonal band (MS-DB) (6), subiculum (SUB) (7 and 8), and entorhinal cortex (EC) (9 and 10). (3), (4), (5), (8), and (10) are enlarged views of the white boxed areas shown in (1), (7) and (9), respectively. Scale bars are labeled for each panel. ***B, ***D*,** The connectivity strength index (CSI) distribution along anterior to posterior positions across the whole brain. The CSI is defined as the number of

input neurons normalized by the number of starter neurons; the AP position is given relative to bregma values. The red arrow at AP= -1.94 mm shows the position of the injection site. Representative input regions were used for the AP plot, including the hippocampal CA1 oriens layer (Or), ipsilateral CA2 and CA3 pyramidal layers (Py), as well as MS-DB, SUB, and EC.

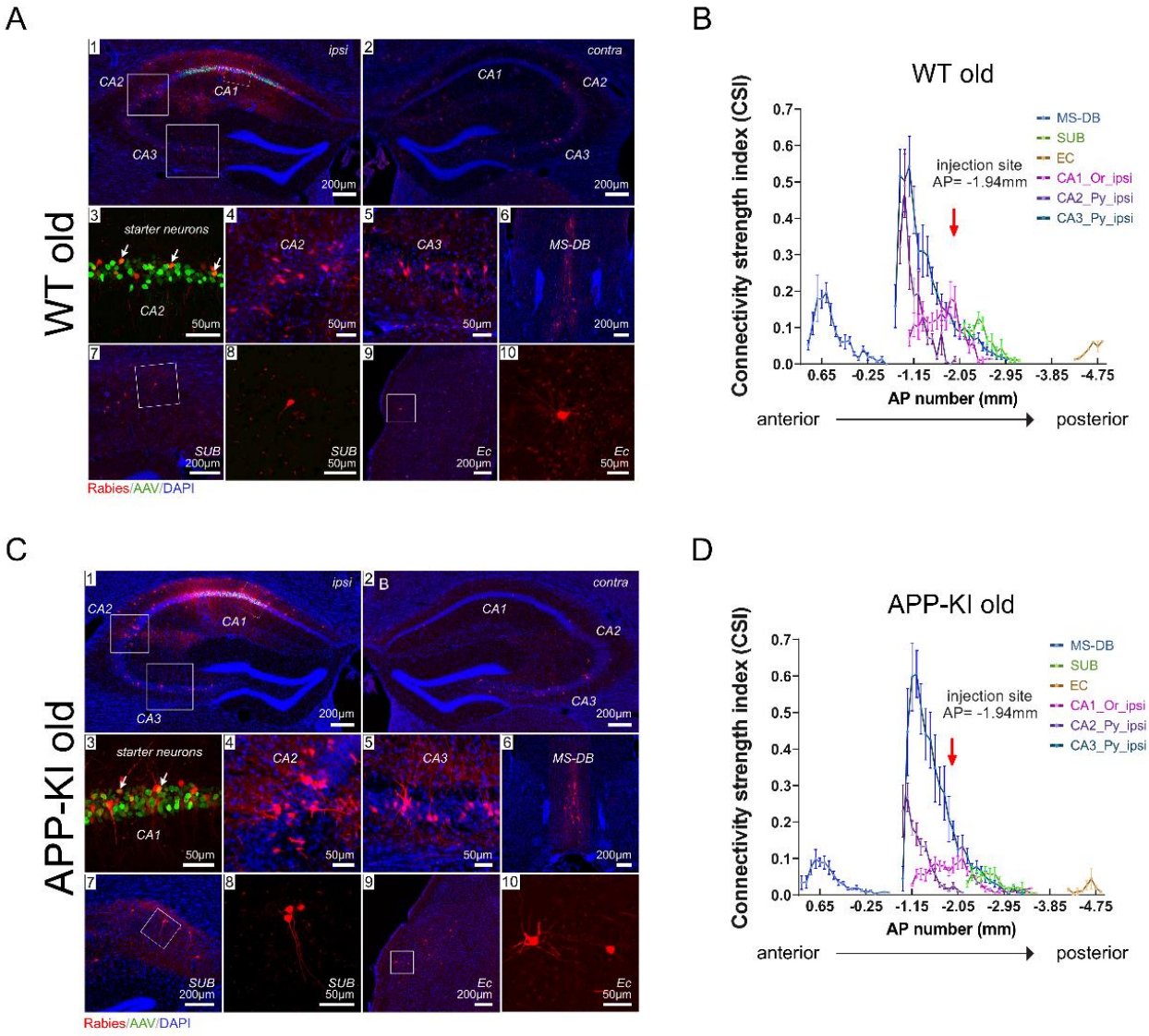

Figure 2.4 Monosynaptic rabies tracing maps specific regional inputs to excitatory CA1 cells along the anterior-posterior (AP) axis in old WT and APP-KI mice

***A*, *C*,** Representative fluorescent coronal section images from WT old (n=10) and APP-KI old (n=8), respectively. Rabies virus-infected neurons are labeled by DsRed, and AAV-infected neurons are in green. All slices are counterstained by DAPI in blue. For both **A and C**, (1) shows the ipsilateral hippocampal formation including the CA1 injection site. (2), rabies virus mapped presynaptic inputs in the contralateral hippocampus. (3), enlarged image of CA1 starter neurons expressing both EGFP and DsRed fluorescent proteins from AAV and rabies virus. For both **A** and **C** (4-10), results of rabies virus-mediated retrograde monosynaptic tracing from CA1. The input regions include hippocampal CA2 (4), CA3 (5), medial septum and diagonal band (MS-DB) (6), subiculum (SUB) (7 and 8), and entorhinal cortex (EC) (9 and 10). (3), (4), (5), (8), and (10)

are enlarged views of the white boxed areas shown in (1), (7), and (9), respectively. Scale bars are labeled for each panel. ***B*****, *****D*****,** The connectivity strength index (CSI) distribution along anterior to posterior positions across the whole brain. CSI is defined as the number of input neurons normalized by the number of starter neurons; AP position is given relative to bregma values. The red arrow at AP= -1.94 mm shows the position of the injection site. Representative input regions were used for the AP plot, including the hippocampal CA1 oriens layer (Or), ipsilateral CA2 and CA3 pyramidal layers (Py), as well as MS-DB, SUB, and EC.

A

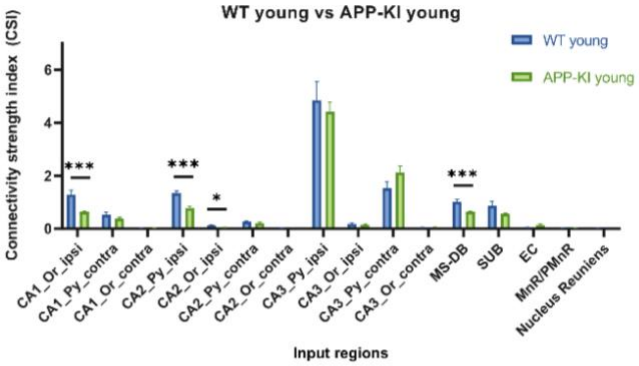
WT young vs APP-KI young
WT young
APP-KI young
Connectivity strength index (CSI)
Input regions
CA1_Or_ipsi
CA1_Py_contra
CA1_Or_contra
CA2_Py_ipsi
CA2_Or_ipsi
CA2_Py_contra
CA2_Or_contra
CA3_Py_ipsi
CA3_Or_ipsi
CA3_Py_contra
CA3_Or_contra
MS-DB
SUB
EC
MnR/PMnR
Nucleus Reuniens

B

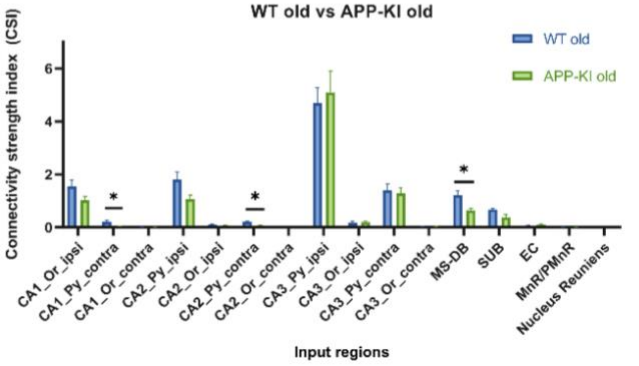
WT old vs APP-KI old
WT old
APP-KI old
Connectivity strength index (CSI)
Input regions
CA1_Or_ipsi
CA1_Py_contra
CA1_Or_contra
CA2_Py_ipsi
CA2_Or_ipsi
CA2_Py_contra
CA2_Or_contra
CA3_Py_ipsi
CA3_Or_ipsi
CA3_Py_contra
CA3_Or_contra
MS-DB
SUB
EC
MnR/PMnR
Nucleus Reuniens

C

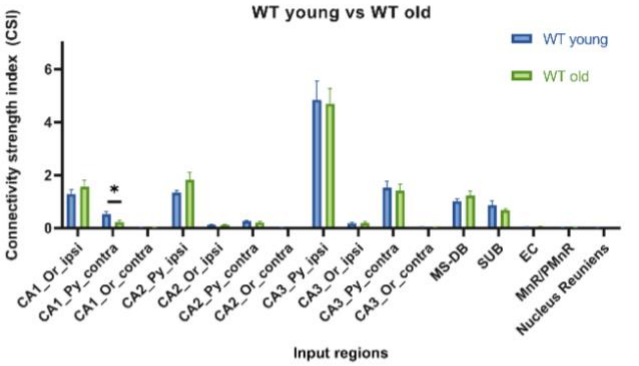
WT young vs WT old
WT young
WT old
Connectivity strength index (CSI)
Input regions
CA1_Or_ipsi
CA1_Py_contra
CA1_Or_contra
CA2_Py_ipsi
CA2_Or_ipsi
CA2_Py_contra
CA2_Or_contra
CA3_Py_ipsi
CA3_Or_ipsi
CA3_Py_contra
CA3_Or_contra
MS-DB
SUB
EC
MnR/PMnR
Nucleus Reuniens

D

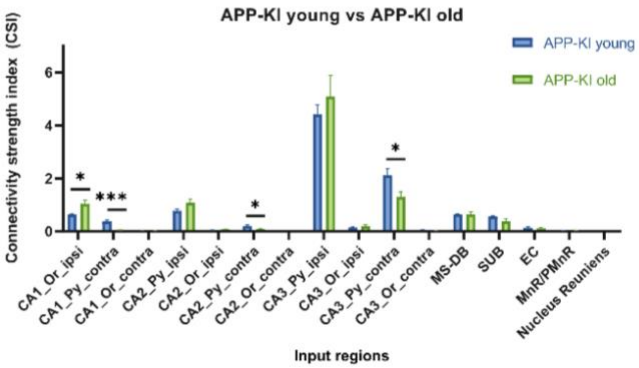
APP-KI young vs APP-KI old
APP-KI young
APP-KI old
Connectivity strength index (CSI)
Input regions
CA1_Or_ipsi
CA1_Py_contra
CA1_Or_contra
CA2_Py_ipsi
CA2_Or_ipsi
CA2_Py_contra
CA2_Or_contra
CA3_Py_ipsi
CA3_Or_ipsi
CA3_Py_contra
CA3_Or_contra
MS-DB
SUB
EC
MnR/PMnR
Nucleus Reuniens

Figure 2.5 Connectivity strength index (CSI) quantification of presynaptic inputs
Quantitative analysis of CA1 CSI values across WT young and old mice and APP-KI young and old mice. The CSI is the ratio of the CA1 input neuron number in a subregion to the total starter neuron number in a brain. The input regions include hippocampal CA1, CA2, and CA3 oriens layer (or) and pyramidal layer (Py), from both the ipsilateral and contralateral sides of the CA1 injection site, as well as the MS-DB, SUB, and EC. ***A*****,** WT young mice (n=7) have significantly higher CSI values relative to APP-KI young mice (n=10) in the CA1_Or_ipsi, CA2_Py_ipsi, CA2_Or_ipsi, and MS-DB regions (Wilcoxon rank-sum test, $p=4.11x10^{-4}$, $p=4.11x10^{-4}$, $p=1.36x10^{-2}$, $p=1.03x10^{-4}$, respectively). ***B*****,** WT old mice (n=10) have significantly higher CSI values relative to APP-KI old mice (n=8) in the CA1_Py_contra, CA2_Py_contra, and MS-DB regions (Wilcoxon rank-sum test, $p=2.64x10^{-2}$, $p=1.17x10^{-2}$, $p=1.55x10^{-2}$, respectively). ***C*****,** WT young mice have significantly higher CSI values relative to WT old mice in the CA1_Py_contra region (Wilcoxon rank-sum test, $p=2.34x10^{-2}$). ***D*****,** APP-KI old mice have significantly higher CSI values relative to APP-KI young mice in the CA1_Or_ipsi region (Wilcoxon rank-sum test, $p=1.17x10^{-2}$). APP-KI young mice have significantly higher CSI values relative to APP-KI old mice in the CA1_Py_contra, CA2_Py_contra, and CA3_Py_contra regions (Wilcoxon rank-sum test, $p=4.6x10^{-5}$, $p=1.55x10^{-2}$, $p=4.34x10^{-2}$, respectively). * $p<0.05$, ** $p<0.01$, *** $p<0.001$, **** $p<0.0001$. All data are represented with mean ±SEM. See also Tables 2.1 and 2.2.

A

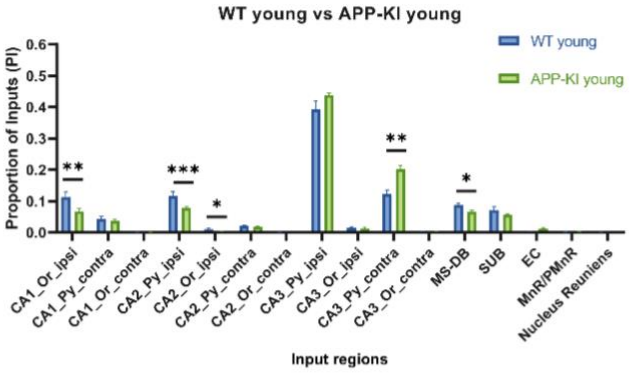
WT young vs APP-KI young
WT young
APP-KI young
Proportion of Inputs (PI)
0.6
0.5
0.4
0.3
0.2
0.1
0.0
**
***
*
**
*
CA1_Or_ipsi
CA1_Py_contra
CA1_Or_contra
CA2_Py_ipsi
CA2_Or_ipsi
CA2_Py_contra
CA2_Or_contra
CA3_Py_ipsi
CA3_Or_ipsi
CA3_Py_contra
CA3_Or_contra
MS-DB
SUB
EC
MnR/PMnR
Nucleus Reuniens
Input regions

B

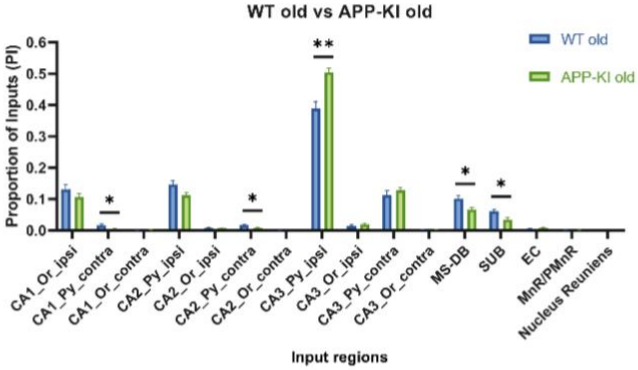
WT old vs APP-KI old
WT old
APP-KI old
Proportion of Inputs (PI)
0.6
0.5
0.4
0.3
0.2
0.1
0.0
**
*
*
*
*
CA1_Or_ipsi
CA1_Py_contra
CA1_Or_contra
CA2_Py_ipsi
CA2_Or_ipsi
CA2_Py_contra
CA2_Or_contra
CA3_Py_ipsi
CA3_Or_ipsi
CA3_Py_contra
CA3_Or_contra
MS-DB
SUB
EC
MnR/PMnR
Nucleus Reuniens
Input regions

C

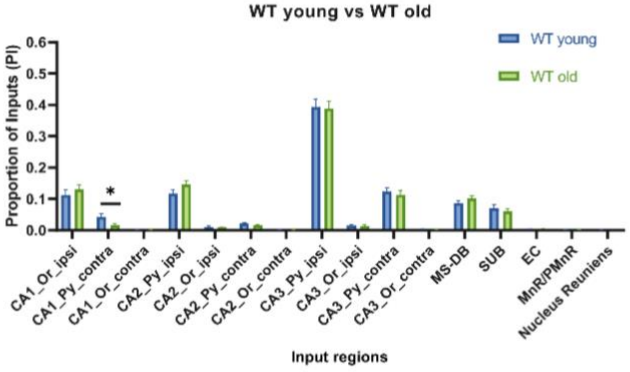
WT young vs WT old
WT young
WT old
Proportion of Inputs (PI)
0.6
0.5
0.4
0.3
0.2
0.1
0.0
*
CA1_Or_ipsi
CA1_Py_contra
CA1_Or_contra
CA2_Py_ipsi
CA2_Or_ipsi
CA2_Py_contra
CA2_Or_contra
CA3_Py_ipsi
CA3_Or_ipsi
CA3_Py_contra
CA3_Or_contra
MS-DB
SUB
EC
MnR/PMnR
Nucleus Reuniens
Input regions

D

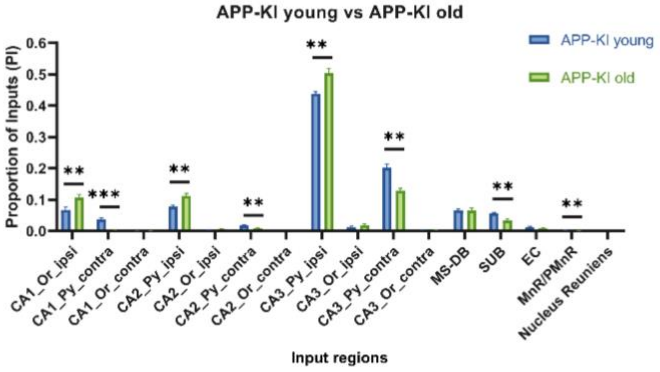
APP-KI young vs APP-KI old
APP-KI young
APP-KI old
Proportion of Inputs (PI)
0.6
0.5
0.4
0.3
0.2
0.1
0.0
**
**
***
**
**
**
**
CA1_Or_ipsi
CA1_Py_contra
CA1_Or_contra
CA2_Py_ipsi
CA2_Or_ipsi
CA2_Py_contra
CA2_Or_contra
CA3_Py_ipsi
CA3_Or_ipsi
CA3_Py_contra
CA3_Or_contra
MS-DB
SUB
EC
MnR/PMnR
Nucleus Reuniens
Input regions

Figure 2.6 Proportion of inputs (PI) quantification of presynaptic inputs
Quantitative analysis of PI values across four groups of mice. The PI is the ratio of the input neuron number in a subregion divided by the total input neuron number in a brain. The input regions include hippocampal CA1, CA2, and CA3 oriens layer (Or) and pyramidal layer (Py), from both the ipsilateral and contralateral sides of the injection site, as well as the MS-DB, SUB, and EC. ***A*****,** APP-KI young mice (n=10) have significantly lower PI values relative to WT young mice (n=7) in the CA1_Or_ipsi, CA2_Py_ipsi, CA2_Or_ipsi and MS-DB regions (Wilcoxon rank-sum test, $p=4.63x10^{-3}$, $p=4.11x10^{-4}$, $p=1.85x10^{-2}$, $p=2.50x10^{-2}$, respectively). APP-KI young mice have significantly higher PI values relative to WT young mice in the CA3_Py_contra region (Wilcoxon rank-sum test, $p=1.95x10^{-3}$). ***B*****,** APP-KI old mice (n=8) have significantly lower PI values relative to WT old mice (n=8) in the CA1_Py_contra, CA2_Py_contra, MS-DB and SUB regions (Wilcoxon rank-sum test, $p=3.39x10^{-2}$, $p=2.66x10^{-2}$, $p=1.17x10^{-2}$, $p=1.55x10^{-2}$, respectively). APP-KI old mice have significantly higher PI values relative to WT old mice in the CA3_Py_ipsi region (Wilcoxon rank-sum test, $p=1.37x10^{-3}$). ***C*****,** WT young mice have significantly higher PI values relative to WT old mice in the CA1_Py_contra region (Wilcoxon rank-sum test, $p=1.36x10^{-2}$). ***D*****,** APP-KI old mice have significantly higher PI values relative to APP-KI young mice in the CA1_Or_ipsi, CA2_Py_ipsi regions, and CA3_Py_ipsi (Wilcoxon rank-sum test, $p=2.06x10^{-3}$, $p=3.06x10^{-3}$, $p=3.2x10^{-4}$, respectively). APP-KI young mice have significantly higher PI values relative to APP-KI old mice in the CA1_Py_contra, CA2_Py_contra, CA3_Py_contra, SUB and MnR/PMnR regions (Wilcoxon rank-sum test, $p=4.6x10^{-5}$, $p=6.22x10^{-3}$, $p=3.06x10^{-3}$, $p=3.06x10^{-3}$, $p=8.48x10^{-3}$, respectively). All data are represented with mean ±SEM. * $p<0.05$, ** $p<0.01$, *** $p<0.001$, **** $p<0.0001$. See also Tables 2.1 and 2.2.

Tables

Table 2.1 Data summary of the connectivity strength index (CSI) and proportion of inputs (PI) index measurements

CSI Summary	WT young		WT old		APP-KI young		APP-KI old	
	Mean	SEM	Mean	SEM	Mean	SEM	Mean	SEM
CA1_or_ipsi	1.2809	0.1721	1.5535	0.2512	0.6259	0.0410	0.9465	0.1517
CA1_py_contra	0.5111	0.1124	0.2108	0.0734	0.3701	0.0456	0.0309	0.0123
CA1_or_contra	0.0187	0.0053	0.0091	0.0033	0.0115	0.0024	0.0117	0.0047
CA2_py_ipsi	1.3293	0.0858	1.8069	0.2971	0.7633	0.0621	1.0734	0.1448
CA2_or_ipsi	0.1070	0.0291	0.1072	0.0276	0.0372	0.0072	0.0622	0.0165
CA2_py_contra	0.2496	0.0257	0.2061	0.0400	0.1975	0.0398	0.0764	0.0126
CA2_or_contra	0.0060	0.0060	0.0022	0.0016	0.0031	0.0012	0.0014	0.0014
CA3_py_ipsi	4.8377	0.7154	4.6866	0.5800	4.4030	0.3643	5.0838	0.8064
CA3_or_ipsi	0.1711	0.0534	0.1769	0.0569	0.1329	0.0232	0.1905	0.0473
CA3_py_contra	1.5206	0.2597	1.4033	0.2529	2.1028	0.2571	1.2865	0.2000
CA3_or_contra	0.0333	0.0116	0.0295	0.0109	0.0402	0.0129	0.0258	0.0072
MS-DB	1.0107	0.0869	1.2202	0.1799	0.6404	0.0236	0.6379	0.0897
SUB	0.8626	0.1605	0.6709	0.0446	0.5553	0.0360	0.3799	0.1044
EC	0.0339	0.0109	0.0516	0.0218	0.1277	0.0354	0.0984	0.0394
MnR/PMnR	0.0188	0.0047	0.0084	0.0048	0.0267	0.0036	0.0151	0.0063
Nucleus Reuniens	0.0044	0.0029	0.0000	0.0000	0.0022	0.0007	0.0011	0.0011

PI Summary	WT young		WT old		APP-KI young		APP-KI old	
	Mean	SEM	Mean	SEM	Mean	SEM	Mean	SEM
CA1_or_ipsi	0.1123	0.0170	0.1302	0.0157	0.0670	0.0094	0.1066	0.0105
CA1_py_contra	0.0424	0.0096	0.0158	0.0049	0.0373	0.0043	0.0039	0.0015
CA1_or_contra	0.0015	0.0005	0.0007	0.0002	0.0010	0.0002	0.0013	0.0005
CA2_py_ipsi	0.1165	0.0135	0.1458	0.0121	0.0776	0.0046	0.1116	0.0084
CA2_or_ipsi	0.0099	0.0037	0.0082	0.0016	0.0039	0.0011	0.0063	0.0012
CA2_py_contra	0.0214	0.0018	0.0160	0.0025	0.0179	0.0027	0.0082	0.0011
CA2_or_contra	0.0008	0.0008	0.0003	0.0003	0.0003	0.0001	0.0002	0.0002
CA3_py_ipsi	0.3925	0.0264	0.3886	0.0225	0.4384	0.0063	0.5040	0.0136
CA3_or_ipsi	0.0143	0.0037	0.0134	0.0040	0.0132	0.0021	0.0186	0.0047
CA3_py_contra	0.1229	0.0128	0.1128	0.0141	0.2019	0.0129	0.1280	0.0084
CA3_or_contra	0.0030	0.0010	0.0022	0.0009	0.0038	0.0010	0.0026	0.0009
MS-DB	0.0867	0.0071	0.1010	0.0092	0.0665	0.0041	0.0659	0.0072
SUB	0.0706	0.0114	0.0605	0.0068	0.0566	0.0026	0.0340	0.0058
EC	0.0029	0.0009	0.0038	0.0015	0.0119	0.0030	0.0076	0.0023
MnR/PMnR	0.0018	0.0006	0.0007	0.0004	0.0027	0.0003	0.0011	0.0004
Nucleus Reuniens	0.0004	0.0003	0.0000	0.0000	0.0002	0.0001	0.0002	0.0002

# of mice	7	10	10	8
# of starters	67±10	59±13	274±23	118±13
# of starter neurons/section	7±1	7±1	22±2	11±1
# of total labeled neurons	829±158	714±194	2829±339	1175±186
Overall connectivity	22.118±1.967	21.019±2.140	14.435±0.722	14.377±1.923

The mean and standard error of the mean (SEM) of the CSI and PI values were calculated for every input region across all mice in each group. The input regions used for statistical analysis include hippocampal CA1, CA2, and CA3 pyramidal layer (Py) and oriens layer (Or), from both

the ipsilateral and contralateral sides of the injection site, as well as the MS-DB, SUB, EC, MnR/PMnR, and nucleus reuniens.

Table 2.2 Summary of CSI and PI comparison statistics

CSI Comparison	WT young vs APP-KI young		WT old vs APP-KI old	
	p value	significance	p value	significance
CA1_or_ipsi	0.000411	***	0.145710	n.s.
CA1_py_contra	0.303682	n.s.	0.026418	*
CA1_or_contra	0.324404	n.s.	0.877462	n.s.
CA2_py_ipsi	0.000411	***	0.083139	n.s.
CA2_or_ipsi	0.013575	*	0.359934	n.s.
CA2_py_contra	0.200689	n.s.	0.011655	*
CA2_or_contra	0.287330	n.s.	0.852941	n.s.
CA3_py_ipsi	0.600884	n.s.	0.896750	n.s.
CA3_or_ipsi	0.618624	n.s.	0.677179	n.s.
CA3_py_contra	0.108803	n.s.	0.965401	n.s.
CA3_or_contra	0.981798	n.s.	>0.999999	n.s.
MS-DB	0.000103	***	0.015540	*
SUB	0.314788	n.s.	0.054527	n.s.
EC	0.144655	n.s.	0.945221	n.s.
MnR/PMnR	0.193233	n.s.	0.243795	n.s.
Nucleus Reuniens	0.643665	n.s.	0.444444	n.s.

Statistical method: Wilcoxon rank sum test.
* p<0.05, ** p<0.01, *** p<0.001, **** p<0.0001

CSI Comparison	WT young vs WT old		APP-KI young vs APP-KI old	
	p value	significance	p value	significance
CA1_or_ipsi	0.600884	n.s.	0.011655	*
CA1_py_contra	0.023396	*	0.000046	****
CA1_or_contra	0.205728	n.s.	0.913913	n.s
CA2_py_ipsi	0.229535	n.s.	0.121989	n.s.
CA2_or_ipsi	0.886775	n.s.	0.203071	n.s.
CA2_py_contra	0.314788	n.s.	0.015540	*
CA2_or_contra	>0.999999	n.s.	0.230769	n.s.
CA3_py_ipsi	0.886775	n.s.	0.761826	n.s.
CA3_or_ipsi	>0.999999	n.s.	0.459756	n.s.
CA3_py_contra	0.812526	n.s.	0.043421	*
CA3_or_contra	0.679864	n.s.	0.713378	n.s.
MS-DB	0.600884	n.s.	0.514786	n.s.
SUB	0.600884	n.s.	0.274281	n.s.
EC	0.309524	n.s.	0.680594	n.s.
MnR/PMnR	0.060469	n.s.	0.100416	n.s.
Nucleus Reuniens	0.154412	n.s.	0.122172	n.s.

Statistical method: Wilcoxon rank sum test.
* p<0.05, ** p<0.01, *** p<0.001, **** p<0.0001

Table 2.2 continued

PI Comparison	WT young vs APP-KI young		WT old vs APP-KI old	
	p value	significance	p value	significance
CA1_or_ipsi	0.004628	**	0.315417	n.s.
CA1_py_contra	0.812526	n.s.	0.033937	*
CA1_or_contra	0.667781	n.s.	0.51017	n.s.
CA2_py_ipsi	0.000411	***	0.083139	n.s.
CA2_or_ipsi	0.018511	*	0.459756	n.s.
CA2_py_contra	0.474702	n.s.	0.026647	*
CA2_or_contra	0.295814	n.s.	0.852941	n.s.
CA3_py_ipsi	0.161251	n.s.	0.001371	**
CA3_or_ipsi	0.669066	n.s.	0.498697	n.s.
CA3_py_contra	0.001954	**	0.359934	n.s.
CA3_or_contra	0.739099	n.s.	0.492618	n.s.
MS-DB	0.02499	*	0.011655	*
SUB	0.474702	n.s.	0.01554	*
EC	0.072707	n.s.	0.119795	n.s.
MnR/PMnR	0.087824	n.s.	0.372275	n.s.
Nucleus Reuniens	0.643665	n.s.	0.444444	n.s.

Statistical method: Wilcoxon rank sum test.
* p<0.05, ** p<0.01, *** p<0.001, **** p<0.0001

PI Comparison	WT young vs WT old		APP-KI young vs APP-KI old	
	p value	significance	p value	significance
CA1_or_ipsi	0.417318	n.s.	0.002057	**
CA1_py_contra	0.013575	*	0.000046	****
CA1_or_contra	0.159348	n.s.	0.965355	n.s.
CA2_py_ipsi	0.108803	n.s.	0.003062	**
CA2_or_ipsi	0.962258	n.s.	0.121989	n.s.
CA2_py_contra	0.108803	n.s.	0.006216	**
CA2_or_contra	>0.999999	n.s.	0.219457	n.s.
CA3_py_ipsi	0.962258	n.s.	0.00032	***
CA3_or_ipsi	0.8116	n.s.	0.572604	n.s.
CA3_py_contra	0.474702	n.s.	0.003062	**
CA3_or_contra	0.448529	n.s.	0.513483	n.s.
MS-DB	0.417318	n.s.	0.696467	n.s.
SUB	0.536199	n.s.	0.003062	**
EC	0.750926	n.s.	0.32634	n.s.
MnR/PMnR	0.095023	n.s.	0.008478	**
Nucleus Reuniens	0.154412	n.s.	0.122172	n.s.

Statistical method: Wilcoxon rank sum test.
* p<0.05, ** p<0.01, *** p<0.001, **** p<0.0001

P-value and significance for each input region between each group. Input regions that do not have a significant difference between groups are labeled not significant (n.s.). The input regions used for statistical analysis include hippocampal CA1, CA2, and CA3 pyramidal layer (Py) and oriens layer (Or), from both the ipsilateral and contralateral sides of the injection site, as well as the MS-DB, SUB, EC, MnR/PMnR, and nucleus reuniens.

Table 2.3 Data summary of sex-specific CSI and PI values

CSI Summary	WT young male		WT young female		WT old male		WT old female		APP-KI young male		APP-KI young female		APP-KI old male		APP-KI old female	
	Mean	SEM	Mean	SEM	Mean	SEM	Mean	SEM	Mean	SEM	Mean	SEM	Mean	SEM	Mean	SEM
CA1_or_ipsi	1.0983	0.1723	1.4178	0.3831	1.4881	0.2591	1.6518	0.5479	0.6510	0.0761	0.6008	0.0381	1.1744	0.2161	0.7798	0.1021
CA1_py_contra	0.4543	0.2352	0.5538	0.1561	0.1636	0.0630	0.2815	0.1664	0.2956	0.0629	0.4446	0.0514	0.0316	0.0169	0.0297	0.0213
CA1_or_contra	0.0083	0.0044	0.0265	0.0076	0.0099	0.0047	0.0079	0.0049	0.0122	0.0039	0.0107	0.0033	0.0137	0.0071	0.0083	0.0052
CA2_py_ipsi	1.3560	0.1026	1.3093	0.1301	1.8017	0.4379	1.8148	0.4275	0.7368	0.0876	0.7898	0.0966	1.2241	0.2039	0.8223	0.0812
CA2_or_ipsi	0.1423	0.0542	0.0805	0.0094	0.1098	0.0258	0.1034	0.0636	0.0448	0.0090	0.0296	0.0112	0.0750	0.0248	0.0409	0.0107
CA2_py_contra	0.2810	0.0534	0.2260	0.0289	0.1909	0.0587	0.2290	0.0556	0.1934	0.0601	0.2016	0.0594	0.0884	0.0180	0.0566	0.0089
CA2_or_contra	0.0140	0.0140	0.0000	0.0000	0.0025	0.0025	0.0017	0.0017	0.0024	0.0017	0.0038	0.0018	0.0022	0.0022	0.0000	0.0000
CA3_py_ipsi	4.6247	1.2095	4.9975	0.5595	4.8688	0.9141	4.4133	0.6264	4.3574	0.5123	4.4486	0.5778	5.7404	1.1893	3.9896	0.6296
CA3_or_ipsi	0.1913	0.0273	0.1560	0.0324	0.1934	0.0559	0.1523	0.1270	0.1372	0.0434	0.1286	0.0232	0.1793	0.0649	0.2092	0.0813
CA3_py_contra	1.4967	0.4797	1.5385	0.1361	1.3514	0.3278	1.4813	0.4555	2.0292	0.3612	2.1764	0.4054	1.5091	0.2532	0.9157	0.2229
CA3_or_contra	0.0403	0.0228	0.0280	0.0119	0.0380	0.0153	0.0167	0.0145	0.0293	0.0151	0.0510	0.0215	0.0222	0.0075	0.0319	0.0165
MS-DB	0.9353	0.0713	1.0673	0.1868	1.1152	0.1923	1.3778	0.3696	0.6346	0.0199	0.6462	0.0458	0.7089	0.1187	0.5196	0.1303
SUB	0.5720	0.1729	1.0805	0.2672	0.6632	0.0735	0.6825	0.0370	0.5360	0.0388	0.5746	0.0643	0.5332	0.1216	0.1243	0.0099
EC	0.0450	0.0257	0.0256	0.0047	0.0495	0.0230	0.0548	0.0474	0.1024	0.0626	0.1530	0.0374	0.1453	0.0534	0.0202	0.0114
MnR/PMnR	0.0256	0.0081	0.0136	0.0071	0.0054	0.0054	0.0129	0.0094	0.0200	0.0044	0.0333	0.0040	0.0227	0.0084	0.0024	0.0024
Nucleus Reuniens	0.0000	0.0000	0.0077	0.0062	0.0000	0.0000	0.0000	0.0000	0.0023	0.0011	0.0022	0.0009	0.0017	0.0017	0.0000	0.0000

PI Summary	WT young male		WT young female		WT old male		WT old female		APP-KI young male		APP-KI young female		APP-KI old male		APP-KI old female	
	Mean	SEM	Mean	SEM	Mean	SEM	Mean	SEM	Mean	SEM	Mean	SEM	Mean	SEM	Mean	SEM
CA1_or_ipsi	0.1071	0.0341	0.1162	0.0225	0.1303	0.0197	0.1301	0.0297	0.0735	0.0188	0.0604	0.0044	0.1053	0.0097	0.1086	0.0265
CA1_py_contra	0.0355	0.0152	0.0476	0.0152	0.0122	0.0047	0.0211	0.0106	0.0295	0.0034	0.0452	0.0064	0.0038	0.0020	0.0041	0.0027
CA1_or_contra	0.0006	0.0003	0.0022	0.0009	0.0007	0.0004	0.0006	0.0004	0.0011	0.0004	0.0010	0.0003	0.0012	0.0007	0.0013	0.0009
CA2_py_ipsi	0.1303	0.0329	0.1062	0.0020	0.1436	0.0129	0.1490	0.0261	0.0760	0.0046	0.0791	0.0087	0.1112	0.0093	0.1122	0.0194
CA2_or_ipsi	0.0152	0.0083	0.0060	0.0009	0.0087	0.0011	0.0076	0.0039	0.0052	0.0019	0.0026	0.0008	0.0067	0.0016	0.0057	0.0019
CA2_py_contra	0.0249	0.0019	0.0187	0.0021	0.0139	0.0027	0.0191	0.0048	0.0178	0.0046	0.0180	0.0034	0.0083	0.0015	0.0079	0.0021
CA2_or_contra	0.0018	0.0018	0.0000	0.0000	0.0005	0.0005	0.0001	0.0001	0.0002	0.0001	0.0003	0.0001	0.0002	0.0002	0.0000	0.0000
CA3_py_ipsi	0.3947	0.0600	0.3909	0.0191	0.4039	0.0291	0.3658	0.0374	0.4447	0.0057	0.4321	0.0112	0.4924	0.0145	0.5234	0.0270
CA3_or_ipsi	0.0185	0.0048	0.0112	0.0035	0.0152	0.0043	0.0107	0.0082	0.0132	0.0034	0.0132	0.0030	0.0142	0.0049	0.0259	0.0088
CA3_py_contra	0.1245	0.0256	0.1217	0.0181	0.1065	0.0153	0.1224	0.0293	0.1996	0.0210	0.2041	0.0174	0.1340	0.0061	0.1180	0.0214
CA3_or_contra	0.0040	0.0020	0.0023	0.0013	0.0030	0.0013	0.0011	0.0009	0.0026	0.0012	0.0049	0.0016	0.0019	0.0008	0.0038	0.0019
MS-DB	0.0878	0.0171	0.0860	0.0052	0.0955	0.0105	0.1091	0.0179	0.0683	0.0076	0.0646	0.0038	0.0636	0.0075	0.0698	0.0169
SUB	0.0489	0.0077	0.0869	0.0197	0.0619	0.0106	0.0585	0.0081	0.0562	0.0035	0.0570	0.0043	0.0444	0.0048	0.0166	0.0007
EC	0.0036	0.0022	0.0024	0.0007	0.0037	0.0017	0.0039	0.0032	0.0098	0.0057	0.0139	0.0023	0.0107	0.0027	0.0024	0.0013
MnR/PMnR	0.0027	0.0013	0.0011	0.0006	0.0005	0.0005	0.0010	0.0006	0.0020	0.0004	0.0033	0.0002	0.0016	0.0005	0.0003	0.0003
Nucleus Reuniens	0.0000	0.0000	0.0007	0.0007	0.0000	0.0000	0.0000	0.0000	0.0002	0.0001	0.0002	0.0001	0.0003	0.0003	0.0000	0.0000

# of mice	3	4	6	4	5	5	5	3
# of starters	69±14	63±22	45±10	80±28	280±47	260±12	125±16	107±27
# of starter neurons/section	7±2	7±1	5±1	9±3	22±3	22±1	13±1	9±1
# of total labeled neurons	768±301	875±131	533±152	987±427	2974±611	2685±365	1373±227	846±257
Overall connectivity	20.657±3.108	23.214±2.789	20.487±3.156	21.818±3.015	13.791±0.982	15.078±1.08	16.513±2.677	10.817±0.685

Grey color filled areas represent male groups.

The CSI and PI values for male and female mice of each group are calculated for every input region. The input regions used for statistical analysis include hippocampal CA1, CA2, and CA3 pyramidal layer (Py) and oriens layer (Or), from both the ipsilateral and contralateral sides of the injection site, as well as the MS-DB, SUB, EC, MnR/PMnR, and nucleus reuniens. Data are represented as mean ± standard error of the mean (SEM).

Table 2.4 Statistical comparisons of WT and APP-KI mouse data between sexes

CSI Comparison	WT young male vs WT young female		WT old male vs WT old female		APP-KI young male vs APP-KI young female		APP-KI old male vs APP-KI old female	
	p value	significance	p value	significance	p value	significance	p value	significance
CA1_or_ipsi	0.628571	n.s.	>0.999999	n.s.	0.84127	n.s	0.392857	n.s
CA1_py_contra	0.942857	n.s.	0.609524	n.s.	0.134921	n.s	0.875	n.s
CA1_or_contra	0.114286	n.s.	0.714286	n.s.	0.587302	n.s	0.785714	n.s
CA2_py_ipsi	0.857143	n.s.	0.914286	n.s.	0.84127	n.s.	0.392857	n.s.
CA2_or_ipsi	0.228571	n.s.	0.609524	n.s.	0.309524	n.s.	0.571429	n.s.
CA2_py_contra	0.628571	n.s.	0.609524	n.s.	0.84127	n.s.	0.571429	n.s.
CA2_or_contra	0.428571	n.s.	>0.999999	n.s.	0.761905	n.s.	>0.999999	n.s.
CA3_py_ipsi	>0.999999	n.s.	0.914286	n.s.	0.84127	n.s.	0.392857	n.s.
CA3_or_ipsi	0.40000	n.s.	0.438095	n.s.	0.84127	n.s.	0.571429	n.s.
CA3_py_contra	>0.999999	n.s.	>0.999999	n.s.	0.690476	n.s.	0.142857	n.s.
CA3_or_contra	0.714286	n.s.	0.552381	n.s.	0.547619	n.s.	0.446429	n.s.
MS-DB	0.857143	n.s.	0.609524	n.s.	>0.999999	n.s.	0.571429	n.s.
SUB	0.114286	n.s.	0.761905	n.s.	>0.999999	n.s.	0.035714	*
EC	0.628571	n.s.	>0.999999	n.s.	0.309524	n.s.	0.142857	n.s.
MnR/PMnR	0.628571	n.s.	0.4	n.s.	0.055556	n.s.	0.142857	n.s.
Nucleus Reuniens	0.428571	n.s.	>0.999999	n.s.	0.825397	n.s.	>0.999999	n.s.

Statistical method: Wilcoxon rank sum test.
* p<0.05, ** p<0.01, *** p<0.001, **** p<0.0001

PI Comparison	WT young male vs WT young female		WT old male vs WT old female		APP-KI young male vs APP-KI young female		APP-KI old male vs APP-KI old female	
	p value	significance	p value	significance	p value	significance	p value	significance
CA1_or_ipsi	0.857143	n.s.	0.914286	n.s.	>0.999999	n.s.	>0.999999	n.s.
CA1_py_contra	0.628571	n.s.	0.476190	n.s.	0.095238	n.s.	>0.999999	n.s.
CA1_or_contra	0.057143	n.s.	0.904762	n.s.	0.460317	n.s.	>0.999999	n.s.
CA2_py_ipsi	0.857143	n.s.	0.914286	n.s.	0.690476	n.s.	>0.999999	n.s.
CA2_or_ipsi	0.400000	n.s.	0.257143	n.s.	0.095238	n.s.	0.571429	n.s.
CA2_py_contra	0.114286	n.s.	0.476190	n.s.	0.841270	n.s.	>0.999999	n.s.
CA2_or_contra	0.428571	n.s.	>0.999999	n.s.	0.841270	n.s.	>0.999999	n.s.
CA3_py_ipsi	0.857143	n.s.	0.476190	n.s.	0.420635	n.s.	0.392857	n.s.
CA3_or_ipsi	0.400000	n.s.	0.438095	n.s.	>0.999999	n.s.	0.250000	n.s.
CA3_py_contra	>0.999999	n.s.	0.761905	n.s.	>0.999999	n.s.	0.785714	n.s.
CA3_or_contra	0.457143	n.s.	0.438095	n.s.	0.309524	n.s.	0.446429	n.s.
MS-DB	0.857143	n.s.	0.761905	n.s.	>0.999999	n.s.	>0.999999	n.s.
SUB	0.114286	n.s.	>0.999999	n.s.	0.841270	n.s.	0.035714	*
EC	0.857143	n.s.	>0.999999	n.s.	0.690476	n.s.	0.071429	n.s.
MnR/PMnR	0.400000	n.s.	0.500000	n.s.	0.031746	*	0.142857	n.s.
Nucleus Reuniens	0.428571	n.s.	>0.999999	n.s.	>0.999999	n.s.	>0.999999	n.s.

Statistical method: Wilcoxon rank sum test.
* p<0.05, ** p<0.01, *** p<0.001, **** p<0.0001

P-value and significance for each input region of comparison between male and female mice in each group. Input regions that do not have a significant difference between groups are labeled not significant (n.s.). The input regions used for statistical analysis include hippocampal CA1, CA2, and CA3 pyramidal layer (Py) and oriens layer (Or), from both the ipsilateral and contralateral sides of the injection site, as well as the MS-DB, SUB, EC, MnR/PMnR, and nucleus reuniens.

References

Andrade-Moraes, C.H., Oliveira-Pinto, A.V., Castro-Fonseca, E., da Silva, C.G., Guimaraes, D.M., Szczupak, D., Parente-Bruno, D.R., Carvalho, L.R., Polichiso, L., Gomes, B.V.*, et al.* (2013). Cell number changes in Alzheimer's disease relate to dementia, not to plaques and tangles. Brain *136*, 3738-3752.

Busche, M.A., Chen, X., Henning, H.A., Reichwald, J., Staufenbiel, M., Sakmann, B., and Konnerth, A. (2012). Critical role of soluble amyloid-beta for early hippocampal hyperactivity in a mouse model of Alzheimer's disease. Proceedings of the National Academy of Sciences of the United States of America *109*, 8740-8745.

Busche, M.A., Eichhoff, G., Adelsberger, H., Abramowski, D., Wiederhold, K.H., Haass, C., Staufenbiel, M., Konnerth, A., and Garaschuk, O. (2008). Clusters of hyperactive neurons near amyloid plaques in a mouse model of Alzheimer's disease. Science *321*, 1686-1689.

Busche, M.A., Kekus, M., Adelsberger, H., Noda, T., Forstl, H., Nelken, I., and Konnerth, A. (2015). Rescue of long-range circuit dysfunction in Alzheimer's disease models. Nature neuroscience *18*, 1623-1630.

Calvo-Rodriguez, M., and Bacskai, B.J. (2021). Mitochondria and Calcium in Alzheimer's Disease: From Cell Signaling to Neuronal Cell Death. Trends Neurosci *44*, 136-151.

Geula, C. (1998). Abnormalities of neural circuitry in Alzheimer's disease: hippocampus and cortical cholinergic innervation. Neurology *51*, S18-29; discussion S65-17.

Hampel, H., Mesulam, M.M., Cuello, A.C., Farlow, M.R., Giacobini, E., Grossberg, G.T., Khachaturian, A.S., Vergallo, A., Cavedo, E., Snyder, P.J.*, et al.* (2018). The cholinergic system in the pathophysiology and treatment of Alzheimer's disease. Brain *141*, 1917-1933.

Hardy, J., and Allsop, D. (1991). Amyloid deposition as the central event in the aetiology of Alzheimer's disease. Trends Pharmacol Sci *12*, 383-388.

Hardy, J., and Selkoe, D.J. (2002). The amyloid hypothesis of Alzheimer's disease: progress and problems on the road to therapeutics. Science *297*, 353-356.

Harris, S.S., Wolf, F., De Strooper, B., and Busche, M.A. (2020). Tipping the Scales: Peptide-Dependent Dysregulation of Neural Circuit Dynamics in Alzheimer's Disease. Neuron *107*, 417-435.

Hyman, B.T., Van Hoesen, G.W., and Damasio, A.R. (1990). Memory-related neural systems in Alzheimer's disease: an anatomic study. Neurology *40*, 1721-1730.

Jeon, S.G., Kim, Y.J., Kim, K.A., Mook-Jung, I., and Moon, M. (2018). Visualization of Altered Hippocampal Connectivity in an Animal Model of Alzheimer's Disease. Mol Neurobiol *55*, 7886-7899.

Jun, H., Bramian, A., Soma, S., Saito, T., Saido, T.C., and Igarashi, K.M. (2020). Disrupted Place Cell Remapping and Impaired Grid Cells in a Knockin Model of Alzheimer's Disease. Neuron *107*, 1095-1112 e1096.

Kim, K., Miller, D., Sapienza, V., Chen, C.-M.J., Bai, C., Grundke-Iqbal, I., Currie, J., and Wisniewski, H. (1988). Production and characterization of monoclonal antibodies reactive to synthetic cerebrovascular amyloid peptide. Neurosci Res Commun *2*, 121-130.

Kosik, K.S., Joachim, C.L., and Selkoe, D.J. (1986). Microtubule-associated protein tau (tau) is a major antigenic component of paired helical filaments in Alzheimer disease. Proceedings of the National Academy of Sciences of the United States of America *83*, 4044-4048.

Lin, X., Chen, L., Baglietto-Vargas, D., Kamalipour, P., Ye, Q., LaFerla, F.M., Nitz, D.A., Holmes, T.C., and Xu, X. (2022). Spatial coding defects of hippocampal neural ensemble calcium activities in the triple-transgenic Alzheimer's disease mouse model. Neurobiol Dis *162*, 105562.

Mehla, J., Lacoursiere, S.G., Lapointe, V., McNaughton, B.L., Sutherland, R.J., McDonald, R.J., and Mohajerani, M.H. (2019). Age-dependent behavioral and biochemical characterization of single APP knock-in mouse (APP(NL-G-F/NL-G-F)) model of Alzheimer's disease. Neurobiol Aging *75*, 25-37.

Miyamichi, K., Shlomai-Fuchs, Y., Shu, M., Weissbourd, B.C., Luo, L., and Mizrahi, A. (2013). Dissecting local circuits: parvalbumin interneurons underlie broad feedback control of olfactory bulb output. Neuron *80*, 1232-1245.
Montero-Crespo, M., Dominguez-Alvaro, M., Alonso-Nanclares, L., DeFelipe, J., and Blazquez-Llorca, L. (2021). Three-dimensional analysis of synaptic organization in the hippocampal CA1 field in Alzheimer's disease. Brain *144*, 553-573.
Nelson, A.R., Kolasa, K., and McMahon, L.L. (2014). Noradrenergic sympathetic sprouting and cholinergic reinnervation maintains non-amyloidogenic processing of AbetaPP. J Alzheimers Dis *38*, 867-879.
Neuman, K.M., Molina-Campos, E., Musial, T.F., Price, A.L., Oh, K.J., Wolke, M.L., Buss, E.W., Scheff, S.W., Mufson, E.J., and Nicholson, D.A. (2015). Evidence for Alzheimer's disease-linked synapse loss and compensation in mouse and human hippocampal CA1 pyramidal neurons. Brain Struct Funct *220*, 3143-3165.
Palop, J.J., Chin, J., Roberson, E.D., Wang, J., Thwin, M.T., Bien-Ly, N., Yoo, J., Ho, K.O., Yu, G.Q., Kreitzer, A.*, et al.* (2007). Aberrant excitatory neuronal activity and compensatory remodeling of inhibitory hippocampal circuits in mouse models of Alzheimer's disease. Neuron *55*, 697-711.
Palop, J.J., and Mucke, L. (2010). Amyloid-beta-induced neuronal dysfunction in Alzheimer's disease: from synapses toward neural networks. Nature neuroscience *13*, 812-818.
Querfurth, H.W., and LaFerla, F.M. (2010). Alzheimer's disease. N Engl J Med *362*, 329-344.
Roland, J.J., Stewart, A.L., Janke, K.L., Gielow, M.R., Kostek, J.A., Savage, L.M., Servatius, R.J., and Pang, K.C. (2014). Medial septum-diagonal band of Broca (MSDB) GABAergic regulation of hippocampal acetylcholine efflux is dependent on cognitive demands. The Journal of neuroscience : the official journal of the Society for Neuroscience *34*, 506-514.
Saito, T., Matsuba, Y., Mihira, N., Takano, J., Nilsson, P., Itohara, S., Iwata, N., and Saido, T.C. (2014). Single App knock-in mouse models of Alzheimer's disease. Nature neuroscience *17*, 661-663.
Selkoe, D.J., American College of, P., and American Physiological, S. (2004). Alzheimer disease: mechanistic understanding predicts novel therapies. Ann Intern Med *140*, 627-638.
Seshadri, S., Wolf, P.A., Beiser, A., Au, R., McNulty, K., White, R., and D'Agostino, R.B. (1997). Lifetime risk of dementia and Alzheimer's disease. The impact of mortality on risk estimates in the Framingham Study. Neurology *49*, 1498-1504.
Soltesz, I., and Losonczy, A. (2018). CA1 pyramidal cell diversity enabling parallel information processing in the hippocampus. Nature neuroscience *21*, 484-493.
Soria Lopez, J.A., Gonzalez, H.M., and Leger, G.C. (2019). Alzheimer's disease. Handb Clin Neurol *167*, 231-255.
Sun, Y., Jin, S., Lin, X., Chen, L., Qiao, X., Jiang, L., Zhou, P., Johnston, K.G., Golshani, P., Nie, Q.*, et al.* (2019). CA1-projecting subiculum neurons facilitate object-place learning. Nature neuroscience *22*, 1857-1870.
Sun, Y., Nguyen, A.Q., Nguyen, J.P., Le, L., Saur, D., Choi, J., Callaway, E.M., and Xu, X. (2014). Cell-type-specific circuit connectivity of hippocampal CA1 revealed through Cre-dependent rabies tracing. Cell reports *7*, 269-280.
Takeuchi, Y., Nagy, A.J., Barcsai, L., Li, Q., Ohsawa, M., Mizuseki, K., and Berenyi, A. (2021). The Medial Septum as a Potential Target for Treating Brain Disorders Associated With Oscillopathies. Front Neural Circuits *15*, 701080.
Viana da Silva, S., Zhang, P., Haberl, M.G., Labrousse, V., Grosjean, N., Blanchet, C., Frick, A., and Mulle, C. (2019). Hippocampal Mossy Fibers Synapses in CA3 Pyramidal Cells Are Altered at an Early Stage in a Mouse Model of Alzheimer's Disease. The Journal of neuroscience : the official journal of the Society for Neuroscience *39*, 4193-4205.
West, M.J., Kawas, C.H., Stewart, W.F., Rudow, G.L., and Troncoso, J.C. (2004). Hippocampal neurons in pre-clinical Alzheimer's disease. Neurobiol Aging *25*, 1205-1212.

Wickersham, I.R., Lyon, D.C., Barnard, R.J., Mori, T., Finke, S., Conzelmann, K.K., Young, J.A., and Callaway, E.M. (2007). Monosynaptic restriction of transsynaptic tracing from single, genetically targeted neurons. Neuron *53*, 639-647.
Xu, X., Sun, Y., Holmes, T.C., and Lopez, A.J. (2016). Noncanonical connections between the subiculum and hippocampal CA1. The Journal of comparative neurology *524*, 3666-3673.
Yu, Z., Guindani, M., Grieco, S.F., Chen, L., Holmes, T.C., and Xu, X. (2022). Beyond t test and ANOVA: applications of mixed-effects models for more rigorous statistical analysis in neuroscience research. Neuron *110*, 21-35.
Zott, B., Simon, M.M., Hong, W., Unger, F., Chen-Engerer, H.J., Frosch, M.P., Sakmann, B., Walsh, D.M., and Konnerth, A. (2019). A vicious cycle of beta amyloid-dependent neuronal hyperactivation. Science *365*, 559-565.

Chapter 3: Monosynaptic Rabies Tracing Reveals Sex- and Age-Dependent Dorsal Subiculum Connectivity Alterations in an Alzheimer's Disease Mouse Model

Abstract

The subiculum (SUB), a hippocampal formation structure, is among the earliest brain regions impacted in Alzheimer's disease (AD). Towards a better understanding of AD circuit-based mechanisms, we mapped synaptic circuit inputs to dorsal SUB using monosynaptic rabies tracing in the 5xFAD mouse model by quantitatively comparing the circuit connectivity of SUB excitatory neurons in age-matched controls and 5xFAD mice at different ages for both sexes. Input-mapped brain regions include hippocampal subregions (CA1, CA2, CA3), medial septum and diagonal band (MS-DB), retrosplenial cortex (RSC), SUB, post subiculum (postSUB), visual cortex (Vis), auditory cortex (Aud), somatosensory cortex (SS), entorhinal cortex (EC), thalamus, perirhinal cortex (Prh), ectorhinal cortex (Ect) and temporal association cortex (TeA). We find sex- and age-dependent changes in connectivity strengths and patterns of SUB presynaptic inputs from hippocampal subregions and other brain regions in 5xFAD mice compared to control mice. Significant sex differences for SUB inputs are found in 5xFAD mice for CA1, CA2, CA3, postSUB, Prh, LEC, and MEC: all areas critical for learning and memory. Notably, we find significant changes at different ages for visual cortical inputs to SUB. While visual function is not ordinarily considered defective in AD, these specific connectivity changes reflect altered visual circuitry contributing to learning and memory deficits. Our work provides new insights into SUB-directed neural circuit mechanisms during AD progression and supports the idea that neural circuit disruptions are a prominent feature of AD.

Significance Statement

Alzheimer's disease is a major health concern in the elderly, but the underlying neural circuit mechanisms of this disease remain unclear. The SUB is a critical brain region for relaying and integrating hippocampal and cortical information. In this study, we applied monosynaptic rabies viral tracing to study the circuit connectivity changes of SUB excitatory neurons in age-

matched, gender-balanced control and 5xFAD mice. We identified age-progressive alterations of connectivity strengths and patterns of SUB neurons in AD model mice. The circuit alterations are differentially impacted in different genders for specific brain regions. Our new findings are supported by human AD literature and can help to identify potential new therapeutical circuit targets for AD treatments.

Introduction

Alzheimer's disease (AD) is the most common form of dementia and a major health concern worldwide. AD age-progressive cognitive decline is correlated with extensive synaptic and neuronal loss. However, the temporal relationship between these behavioral and brain structural connectivity changes remains poorly understood. Recent evidence suggests that disruption of long-range and local neural circuit connections is a functionally critical defect in human AD patients and animal models (Busche et al., 2015; Harris et al., 2020; Jeon et al., 2018). DiI-based retrograde neural circuit tracing of the hippocampus in the 5xFAD mouse model demonstrates decreased hippocampal inputs from MS-DB, EC, auditory cortex, locus coeruleus, dorsal raphe, substantia nigra pars compacta, and olfactory bulb (Jeon et al., 2018). Our recent work using monosynaptic rabies virus tracing reveals substantial connectivity alterations of hippocampal CA1 excitatory neurons in the amyloid precursor protein (APP) knock-in mouse model (Ye et al., 2022). Furthermore, AD prevalence differs between males and females, but the underlying basis of this remains poorly understood. In humans, females have a higher risk of developing pathological features of AD than men who are the same age (Calvo and Einstein, 2023; Seshadri et al., 1997). We recently found sex differences in CA1 connectivity and patterns in APP-KI mice (Ye et al., 2022). Specifically, aged AD female mice have significantly lower SUB to CA1 connectivity defects compared to aged AD male mice.

Our present work focuses on the SUB, a brain region that plays a role in spatial navigation, mnemonic processing, and control of the stress response (O'Mara, 2005). The degeneration of vulnerable pyramidal neurons in the SUB is among the earliest neuropathological changes in AD (Good et al., 2004). We used the 5xFAD mouse line (Oakley et al., 2006) to study the SUB neural connectivity. The 5xFAD mouse line expresses AD-related human transgenes APP and presenilin 1 (PSEN1), with Swedish (K670N/M671L), Florida (I716V), and London (V717I) mutations in APP, and M146L and L286V mutations in PSEN1. 5xFAD mice develop AD-related neuropathological phenotypes early and quickly (Oakley et al., 2006). Anti-amyloid beta (Aβ) immunostaining in a 5xFAD model mouse shows the highest density of Aβ deposits occurring within the pyramidal neurons of the SUB and deep cortical layers (Oakley et al., 2006). To test our hypothesis that SUB input connections are altered in the 5xFAD mouse model, we used genetically modified monosynaptic rabies virus tracing to measure the circuit connectivity of SUB excitatory neurons. Technical developments in rabies tracing methods allow for the semi-quantitative mapping of cell-type-specific neural circuit connections (Sun et al., 2019; Sun et al., 2014; Xu et al., 2020; Xu et al., 2016). EnvA pseudotyping enables the modified rabies virus to infect specific cell types. Trans-synaptic rabies spread is limited to direct presynaptic inputs using a glycoprotein gene deleted (ΔG) rabies virus and transcomplementation with glycoprotein expression offered by helper AAV that provides both TVA and glycoprotein in SUB cells.

To determine age-dependent neural circuit alterations, we examined age-matched control wild-type (WT) and 5xFAD mice at two ages (3-4 and 8-9 months) for both sexes. The age groups were chosen based on previous findings of behavioral and social deficits, and neuropathological developments (Kosel et al., 2019; Oakley et al., 2006). The 5xFAD mouse SUB shows increased synaptic degeneration and neuron loss at around 9 months old (Eimer and Vassar, 2013). We are interested in determining the age-related progression and sex-specific differences in the AD phenotype in relation to SUB input connectivity. Our results show significant alterations in the circuit connectivity of SUB in AD model mice, with overall weaker connectivity strengths,

connectivity pattern shifts, and significant sex differences in 5xFAD mice compared to control mice.

Materials and Methods

Animals

All experiments were managed according to the National Institutes of Health (NIH) guidelines for animal care and use, and were authorized by the University of California, Irvine Institutional Animal Care and Use Committee (IACUC) and Institutional Biosafety Committee (IBC). To study SUB circuit connections in the Alzheimer's disease mouse model, control and 5xFAD mice at two ages were used: WT C57BL/6, with a young group at 3-4 months old (n = 8, 3 males, 5 females) and a middle-age group at 8-9 months old (n = 10, 5 males, 5 females), and 5xFAD (C57BL/6 background, The Jackson Laboratory #034848, ME, USA), with a young group at 3-4 months old (n = 10, 6 males, 4 females) and a middle-age group at 8-9 months old (n = 12, 5 males, 7 females). The 5xFAD and WT C57BL/6 mice were of the same genetic background but not littermates. All mice had free access to food and water in their home cages with lights maintained on a 12h/12h light/dark cycle. All personnel working with the rabies virus received rabies vaccinations and the virus-related experiments were conducted under biosafety level (BSL) 2 conditions.

Viral injections

To study neural circuit connections, mice were injected with helper AAVs and rabies virus. Mice were first anesthetized under 1-2% isoflurane for 10 minutes with a 0.8 L/min oxygen flow rate using an isoflurane tabletop unit (HME109, Highland Medical Equipment, Temecula, CA, USA). Their head fur was shaved and the mice were then placed in a rodent stereotaxic frame (Leica Angle Two™ for mouse, Leica Biosystems Inc., Buffalo Grove, IL, USA) with a continuous

flow of 1-2% isoflurane anesthetic. After disinfection with 70% alcohol and Betadine, the skin received a small incision and the skull was exposed to reveal the landmarks of bregma and lambda. The desired injection site relative to bregma and lambda was located using a three-axis manipulator, with the guidance of a digital brain atlas of the stereotaxic machine. A small craniotomy was performed above the injection site, exposing the dura. A glass pipette (tip inner diameter, 20-30 μm) was loaded with virus solution and lowered to the target injection site. The virus was delivered through a picospritzer (Parker Hannifin, Hollis, NH, USA) pressure injection machine at a rate of 20-30 nL/min with a 10 ms pulse duration. The virus was injected into the dorsal SUB using the following coordinates: anteroposterior (AP) -3.40 mm, mediolateral (ML) +2.00 mm, dorsoventral (DV) -1.67 mm, all values given relative to bregma. In order to prevent backflow of the virus immediately following injection, the glass pipette was held at the injection site for 10 minutes after virus delivery and was then withdrawn at a constant slow speed. After the mice were removed from the stereotaxic frame, their skin was sutured using tissue adhesive (3M Vetbond, St. Paul, MN, USA). The mice were injected with 5mg/kg carprofen subcutaneously to mitigate pain and inflammation and were placed on a heating pad for 15 minutes post-surgery, where they were monitored until waking, and were then returned to their home cages.

To map the retrograde circuit connectivity of the SUB, the following helper AAVs were used: AAV8-DIO-TC66T-2A-GFP-2A-oG (Salk Institute, CA, USA, 2.36×10^{13} GC/ml) and pENN.AAV.CamKII 0.4.Cre.SV40 (Addgene viral prep #105558-AAV1, 5.3×10^{13} GC/ml). pENN.AAV.CamKII 0.4.Cre.SV40 was a gift from Dr. James M. Wilson. The AAV8-DIO-TC66T-2A-GFP-2A-oG was 1:2 diluted with Hank's balanced salt solution (HBSS). The pENN.AAV.CamKII 0.4.Cre.SV40 was 1:4 diluted with HBSS. These two diluted helper AAVs were finally 1:1 mixed. The final titers for the two viruses are 5.9×10^{12} GC/ml (AAV8-DIO-TC66T-2A-GFP-2A-oG) and 6.63×10^{12} GC/ml (pENN.AAV.CamKII 0.4.Cre.SV40). On the first day, the SUB target site was delivered with 0.05 μl of the AAV mixture by pressure injection. Following 20 days, the mice were injected with the rabies virus EnvA-RV-SADΔG-DsRed (CNCM, 2.1×10^{9}

IU/ml, 0.4 µl) at the same injection site using pressure injection. The rabies virus was produced at the Center for Neural Circuit Mapping (CNCM) virus core facility of the University of California, Irvine, with required cell lines and seeding viruses originally developed in Dr. Edward Callaway's group at the Salk Institute for Biological Studies. For 9 days before the mice were perfused for tissue processing, the rabies virus was allowed to replicate and retrogradely spread from targeted Cre+ starter neurons to directly connected presynaptic neurons.

Histology and Immunochemistry

The mice were transcardially perfused with 20 ml of PBS and then with 40 ml of PBS containing 4% paraformaldehyde (PFA) using a mini pump with variable flows (United States Plastic Corp., USA). The perfused brains settled in 4% PFA solution for 24 hours followed by 30% sucrose-PBS solution for another 24 hours at 4°C before histological processing. The brains were then frozen in dry ice and coronally sectioned at 30 µm thickness on a microtome (Leica SM2010R, Germany).

For each mouse brain, coronal sections were collected continuously into a 24-well plate across the wells. For brain-wide neural circuit mapping analysis, 1 out of 3 consecutive coronal sections across the entire brain were counterstained with DAPI, mounted and then imaged. Therefore, a third of the whole brain section series was used for quantification.

To examine amyloid-beta expression, one coronal slice in each mouse for both genders (n = 4-5 for each gender) from each mouse group were stained with primary antibody 6E10 (Biolegend, Mouse, #803002,1:500 dilution, USA), followed by Cy5 conjugated donkey anti-mouse secondary antibody (Jackson ImmunoResearch, #715-175-151,1:200 dilution, USA).

All sections were imaged by an automated fluorescent slide scanner microscope (Olympus VS120-S6, Japan) with a 10× magnification objective. For high-resolution imaging of selected brain slices, a confocal microscope was utilized (Olympus FLUOVIEW FV3000, Japan) with a 40× magnification objective.

Data quantification and statistical analysis

For amyloid analysis, the amyloid plaque number, plaque size, plaque intensity, intraneuronal 6E10+ number, as well as the SUB field of view (FOV) were quantified in an unbiased fashion using the measurement tool in Fiji ImageJ (NIH, USA). The SUB region included for amyloid quantification was contralateral to the injection site with similar anterior-to-posterior position.

For rabies circuit tracing analysis, we followed an established counting protocol (Sun et al., 2014). A third of the whole brain coronal sections were arranged on an overview canvas in Adobe Photoshop software (Adobe, San Jose, CA, USA). We identified brain sections containing the SUB region in which we searched for double-labeled starter neurons with EGFP (helper AAVs) and DsRed (rabies). Next, we aligned the rest of the virally-infected brain sections using a standard mouse brain atlas (Paxinos, 2008) to determine the anatomical structures of brain regions containing rabies-labeled neurons using DAPI-labeled morphological features. No stereological measurement protocol was used. All labeled cells in each mounted brain were counted using the Adobe Photoshop count tool. We operationally determined the input connectivity strength index (CSI) as the ratio of the number of presynaptic neurons in a brain region of interest versus the number of starter neurons in the SUB region. In this study, the CSI refers to the connectivity strength index that is calculated based on the number of single-labeled red fluorescent neurons in an area versus the number of double-labeled red and green starter neurons in SUB. The CSI values allow us to numerically compare the input strengths of different brain regions while normalized to the number of excitatory SUB neurons. We calculated the proportion of inputs (PI) index as the ratio of the number of labeled presynaptic neurons in a brain region of interest versus the total number of labeled neurons in each brain to show the proportional distribution of each input region. For rabies data quantification, only the cases with starter neurons

restricted within the dorsal SUB region were included. Any cases that showed evidence of leakage to other adjacent regions were excluded.

The anterior-to-posterior (AP) CSI distribution curve was plotted to reveal the input pattern across the AP axis of the mouse brains. The input-labeled neuron numbers were counted for every brain slice for each mouse, which corresponds to an AP position number (relative to bregma) according to the standard mouse brain atlas (Paxinos, 2008). The CSI values were calculated as described above. For all mice within the same age/genotype group, the CSI values were registered to similar AP positions and were plotted along the AP axis using a custom-written MATLAB analysis pipeline.

All data are presented as the mean ± SEM. We applied appropriate statistical tests, and the data analysis was conducted using GraphPad Prism (GraphPad Software, San Diego, CA, USA) or custom-written MATLAB scripts. Statistical analysis methods included the Wilcoxon rank-sum test, paired Wilcoxon rank-sum test, and linear mixed effects model (LME) (Yu et al., 2022). The LME model was applied to analyze the size and intensity of amyloid plaques. Using LME is critical for avoiding false positive statistical results for comparisons between animal groups where repeated amyloid measurements were taken from each animal. For CSI/PI multiple comparisons across the young, and middle age WT and 5xFAD mice, the p values were adjusted for multiple comparisons using the False Discovery Rate (FDR) Benjamini-Hochberg approach with a desired FDR equals to 0.05. Alpha levels of $p \leq 0.05$ were considered significant. Different levels of statistical significance are represented by * $p \leq 0.05$, ** $p \leq 0.01$, *** $p \leq 0.001$, and **** $p \leq 0.0001$.

Code accessibility

The custom analysis scripts are available on GitHub (https://github.com/QiaoYeNeuro/Brain-Circuit-Connectivity-Analysis).

Results

Age-dependent and sex-specific differences in SUB amyloid deposition

In this study, we used the 5xFAD mouse model to study the neural circuit connectivity of SUB excitatory neurons. We focus on the SUB as it is one of the earliest brain regions to show degeneration in Alzheimer's disease (Carlesimo et al., 2015). The 5xFAD mouse model expresses five human familial AD-associated genes (Oakley et al., 2006). We first set out to characterize the Aβ level of the SUB region in the 5xFAD mouse model. To detect Aβ levels in 5xFAD and WT mice, we immunostained mouse brain sections with 6E10 Aβ monoclonal antibody (Kim et al., 1988) and quantified the plaque levels in male and female mice at young (3-4 months) and middle (8-9 months) ages for both genotypes (Fig. 1). Aβ antibody 6E10 immunostaining reveals extensive amyloid plaque deposition in the SUB of 5xFAD mice (Fig. 1A-E). In contrast, no 6E10-immunopositive staining appears in WT young or middle-age mice. We find staining in two forms, Aβ as plaques in the extracellular space and intraneuronal aggregates. Quantitative plaque analysis of 6E10 staining shows that 5xFAD middle-age mice have significantly greater plaque size and immunofluorescence intensity in the SUB relative to 5xFAD young mice (Fig. 1C, D) (Linear mixed effects model, $p = 1.86\times10^{-12}$, $p = 9.13\times10^{-7}$, respectively). The extracellular plaque size value of the 5xFAD young group is 73.59 ± 1.645 and the 5xFAD middle-age group is 139.9 ± 2.247; the extracellular plaque staining intensity value of the 5xFAD young group is 3018 ± 33.42 and 5xFAD middle-age group is 3761 ± 30.54. There are no significant differences detected in extracellular plaque density between 5xFAD young and middle-age mice, although 5xFAD middle-age mice do have slightly higher plaque density relative to 5xFAD young mice (Fig. 1B) (Wilcoxon rank-sum test, $p = 0.0676$). The density value of the 5xFAD young age group is 2151 ± 214.3 and the 5xFAD middle-age group is 2698 ± 141.8. While no intraneuronal Aβ staining is present in WT mice, 6E10 immunostaining revealed a substantial density of neurons with intraneuronal staining in 5xFAD mice. The density of neurons with intraneuronal staining in 5xFAD mice has an age-progressive decline, with significantly higher

density in 5xFAD young mice compared to 5xFAD middle-age mice, which is consistent with the age-dependent neurodegenerative nature of AD (Fig. 1E) (Wilcoxon rank-sum test, $p = 7.58\times10^{-5}$). The intraneuronal density value of the 5xFAD young age group is 7188 ± 548.1 and the 5xFAD middle-age group is 3554 ± 396.7. 6E10 immunostaining of the SUB also reveals significant sex differences in plaque density, size, and intensity for 5xFAD mice (Fig. 1F-J). Middle-age male and young age female 5xFAD mice exhibit significantly higher extracellular plaque densities compared to young age male 5xFAD mice (Fig. 1G). (Wilcoxon rank-sum test, $p = 0.0159$, $p = 0.0079$, respectively). The density values of the 5xFAD young group are 1601 ± 94.84 (male), 2702 ± 214.6 (female) and 5xFAD middle-age group are 2432 ± 157.5 (male), 2963 ± 148.6 (female). In terms of plaque size, significantly larger plaque size is detected in middle-age male 5xFAD mice compared to young male 5xFAD mice, and middle-age female 5xFAD mice show significantly larger plaque size than those of young female 5xFAD mice (Fig. 1H) (Linear mixed effects model, $p = 2.63\times10^{-11}$, $p = 5.81\times10^{-6}$, respectively). The size values of the 5xFAD young group are 68.69 ± 2.734 (male), 74.30 ± 2.022 (female) and 5xFAD middle-age group are 130.4 ± 2.917 (male), 149.8 ± 3.421 (female). Significantly stronger plaque intensity is detected in middle-age male 5xFAD mice compared to young age male 5xFAD mice, in middle-age female 5xFAD mice compared to young female 5xFAD mice, and in young female 5xFAD young compared to young male 5xFAD mice (Fig. 1I) (Linear mixed effects model, $p = 1.39\times10^{-23}$, $p = 0.0118$, $p = 6.76\times10^{-16}$, respectively). The intensity values of the 5xFAD young group are 1985 ± 35.98 (male), 3473 ± 37.11 (female) and 5xFAD middle-age group are 3718 ± 37.67 (male), 3805 ± 48.52 (female). Male and female 5xFAD mice exhibit a significant decrease in the density of neurons with intraneuronal staining as age progresses, and the neuronal density of young and middle-age male 5xFAD mice is significantly higher than that of young and middle-age 5xFAD female mice, respectively (Fig. 1J) (Linear mixed effects model, $p = 0.0079$, $p = 0.0079$, $p = 0.0317$, $p = 0.0079$, respectively). The intraneuronal density values of the 5xFAD young group are 8579 ± 293.9 (male), 5896 ± 656.4 (female) and 5xFAD middle-age group are 4603 ± 323.5 (male), 2506 ± 232

(female). For each of the four groups the sample size is n=4-5 mice. One representative section was quantified from each mouse (Fig. 1B-E, G-J). Sample sizes for the linear mixed effects model analysis consist of the number of individual plaques for each group (Fig. 1C, D, H, and I) (Extracellular: 5xFAD young male n=432, 5xFAD young female n=980, 5xFAD middle male n=1321, 5xFAD middle female n=1255). More statistical details are provided in Table 3.1 and Table 3.2. The unit for plaque size is μm^2, plaque density is per mm^2, and the intensity is arbitrary unit (AU) of optical density. Overall, our SUB amyloid immunostaining results reveal strong age-dependent and sex-dependent alterations.

Brain-wide neural circuit connections to SUB excitatory cells are altered in 5xFAD mice

To investigate whether the SUB circuit connectivity is altered in AD model mice, we applied Cre-dependent monosynaptic rabies tracing in gender-balanced, age-matched 5xFAD and WT mice as shown schematically (Fig. 2A). The rabies tracing was performed at young (3-4 months) and middle (8-9 months) ages. The Cre-dependent monosynaptic rabies virus enables retrograde mapping of neural circuit inputs to specific neuron cell types in conjunction with helper AAVs. Our monosynaptic rabies tracing approach takes advantage of the ability to target rabies infection to specific cell types using EnvA pseudotyping, and to limit trans-synaptic spread to direct inputs, by using glycoprotein gene-deleted (ΔG) rabies virus and transcomplementation. EnvA-pseudotyped rabies virus can only infect neurons that express avian tumor virus receptor A (TVA), an avian receptor protein that is absent in mammalian cells unless it is provided through exogenous gene delivery. The deletion-mutant rabies virus can then be transcomplemented with the expression of rabies glycoprotein in the same TVA-expressing cells to enable its retrograde spread restricted to direct presynaptic neurons. To target the excitatory neurons in the SUB, a mixture of helper AAV was injected (AAV1-CaMKIIα-cre and AAV8-DIO-TC66T-oG-EGFP) stereotaxically into the SUB in the right hemisphere of all experiment mice. The combination of the double inverted open frame (DIO) and Cre recombinase allows for the expression of a highly specific TVA receptor (TC66T)

(Miyamichi et al., 2013) and optimized rabies glycoprotein (oG) in CaMKIIα positive excitatory SUB neurons. Twenty days after the initial AAV injection, the EnvA pseudotyped G-deleted rabies virus (EnvA-RV-SADΔG-DsRed) was delivered stereotaxically to the same injection site as the helper AAVs. The rabies virus was incubated for 9 days before the mice brains were harvested for sectioning and further histological processing. Overall, we map the presynaptic connections of SUB excitatory neurons in multiple brain regions for both 5xFAD and WT mice (Fig. 2C). These inputs primarily originate from the medial septum and diagonal band (MS-DB), hippocampal CA1, CA2, CA3, retrosplenial cortex (RSC), SUB, post subiculum (postSUB), visual (Vis) cortex, auditory (Aud) cortex, somatosensory (SS) cortex, temporal association cortex (TeA), perirhinal cortex (Prh), ectorhinal cortex (Ect), lateral entorhinal cortex (LEC) and medial entorhinal cortex (MEC) (Fig. 2C). Notably, the SUB excitatory neurons receive strong intrinsic connections from local SUB neurons. For both 5xFAD and WT mice at young and middle ages, the strongest inputs originate from the hippocampal CA1 pyramidal layer. To quantitatively assess the brain-wide overall connectivity of SUB excitatory neurons, we divide the total number of neurons labeled in the entire brain over the number of starter neurons. The initial AAV and rabies-infected neurons are defined as the starter neurons, which express both EGFP and DsRed signals; rabies-labeled presynaptic neurons display only DsRed fluorescence (Fig. 2A). Our results indicate that the SUB excitatory neuron input connections in middle-age 5xFAD mice are compromised with weaker overall brain-wide connectivity compared to WT mice at both ages and young 5xFAD mice (Fig. 2B).

Regional-specific SUB neural circuit connectivity alterations in 5xFAD mice

To map and compare the regional-specific connections to SUB excitatory neurons in age-matched 5xFAD and WT mice, one out of every three sections in each brain coronal section series was mounted for examination and quantification of starter cells and their presynaptic cells in different brain structures. The example presynaptic labeled brain regions as well as the SUB

injection site are shown for each mouse group (WT young: Fig. 3, WT middle-age: Fig. 4, 5xFAD young age: Fig. 5, 5xFAD middle-age: Fig. 6). All brain slices are counterstained with DAPI. Neurons infected with AAV are shown in green (GFP) and rabies-labeled neurons are shown in red (DsRed). For both WT and 5xFAD mice at young and middle ages, the SUB presynaptic input regions include ipsilateral hippocampal CA1 pyramidal layer (CA1_py), CA1 oriens layer (CA1_or), CA1 radiatum layer (CA1_rad), CA1 lacunosum-moleculare layer (CA1_lmol), CA2 pyramidal layer (CA2_py), CA2 oriens layer (CA2_or), CA3 pyramidal layer (CA3_py), CA3 oriens layer (CA3_or), local SUB neurons, postSUB, MS-DB, thalamus, RSC, Vis cortex, Aud cortex, SS cortex, TeA, Prh, Ect, LEC, and MEC. Very sparse labeling was occasionally observed in contralateral CA1, hypothalamus, dentate gyrus, cingulate cortex, and midbrain, and was thus not included in statistical comparison analysis. The SUB input brain regions mapped by rabies tracing in WT young, WT middle-age, 5xFAD young, and 5xFAD middle-age are generally consistent.

To quantitatively compare the connectivity difference across different experiment groups, we aligned one-third of the entire brain coronal slices and quantified the starter neuron numbers and the presynaptic input neuron numbers for each brain region. To determine semi-quantitative normalized neural connectivity, we operationally defined the connectivity strength index (CSI). The CSI is presented by the number of rabies-labeled presynaptic neurons in a brain region divided by the number of starter neurons in the SUB. The CSI value reflects an absolute measurement of the connectivity between the SUB and its presynaptic input regions.

To investigate the brain-wide neuron input distribution pattern along the anterior-to-posterior (AP) axis in both WT and 5xFAD mice at young and middle ages, the input CSI values of major brain regions are calculated for each brain section along the AP axis of the mouse brain (Fig. 7). The example brain regions included in the analysis are the ipsilateral hippocampal CA1 pyramidal layer, SUB, MS-DB, RSC, Vis cortex, and Aud cortex. The SUB excitatory cells in the four groups of mice show an overall similar distribution pattern of regional inputs, with MS-DB

accounting for the most anterior position, followed by thalamus, hippocampal CA1, Vis cortex, and Aud cortex, moving progressively more posteriorly. Notably, for 5xFAD middle-age mice, there is a significant decrease in area-under-curve of CA1 pyramidal inputs than the WT young group (5xFAD middle-age vs. WT young, $p = 1.67\times10^{-6}$, paired Wilcoxon rank-sum test).

Quantitative comparisons of SUB connectivity strengths show significant age-dependent differences between controls versus 5xFAD mice

To quantitatively assess the connectivity strength differences for WT young, WT middle-age, 5xFAD young and 5xFAD middle-age mice, we calculated the CSI values for each presynaptic brain region and compared them across genotypes and ages (Fig. 8, Table 3.3). The presynaptic input regions include subregions within the hippocampus, SUB complex, sensory cortex and EC, as denoted by colored shades, as well as other regions mentioned above (Fig. 8D). Overall, SUB receives the strongest inputs from the ipsilateral CA1 pyramidal layer for all mouse groups. As noted, the average CSI value of CA1_py inputs is very extensive (~38 for WT young mice). Besides the strongest inputs from CA1 sublayers, the rabies tracing reveals substantial non-canonical connections from CA2 and CA3. The second largest set of inputs originates from local SUB neurons. Among the sensory cortical regions, the visual cortex is the major input source. For the thalamic inputs, the inputs are primarily from the anterior thalamus.

Detailed statistical comparisons between the four groups of mice reveal significant CSI differences (Fig. 8, Table 3.4). Comparing age-matched WT and 5xFAD mice, the visual cortex of the 5xFAD young group shows significantly stronger input connections to excitatory SUB neurons relative to the WT young group (Fig. 8A) (Wilcoxon rank-sum test, $p = 1.29\times10^{-2}$). The CSI value of the WT young group is 1.275 ± 0.7136; the CSI value of the 5xFAD young group is 5.2217 ± 1.6207. For comparison between the two middle-age groups, 5xFAD middle-age mice show significantly smaller CSI values in CA1_py, CA1_or, CA1_rad, MS-DB, Vis cortex, and Aud cortex compared to WT middle-age mice (Fig. 8B) (Wilcoxon rank-sum test, $p = 1.2\times10^{-4}$, p =

4.46×10^{-2}, $p = 8.78\times10^{-3}$, $p = 3.33\times10^{-3}$, $p = 1.29\times10^{-2}$, $p = 1.38\times10^{-2}$, respectively). The CSI values of WT middle-age group are 31.5 ± 4.3837 (CA1_py),1.2242 ± 0.2206 (CA1_or), 0.2302 ± 0.0286 (CA1_rad), 1.0204 ± 0.1924 (MS-DB), 2.828 ± 1.5745 (Vis cortex), 0.7486 ± 0.5241 (Aud cortex); the CSI values of 5xFAD middle-age group are 13.8835 ± 1.3216 (CA1_py), 0.5687 ± 0.1026 (CA1_or), 0.1216 ± 0.0318 (CA1_rad), 0.4593 ± 0.0628 (MS-DB), 0.5301 ± 0.2877 (Vis cortex), 0.0672 ± 0.0390 (Aud cortex), showing decreased connectivity in aged 5xFAD mice. In terms of comparison within the same genotype but at different ages, WT young and WT middle-age groups show a significant difference in CSI values at CA1_rad, SUB and MS-DB (Fig. 8C) (Wilcoxon rank-sum test, $p = 8.78\times10^{-3}$, $p = 4.66\times10^{-2}$, $p = 2.74\times10^{-2}$, respectively). Among these regions, only CA1_rad shows higher CSI values in WT middle-age mice. The CSI values of WT young group are 0.116 ± 0.0193 (CA1_rad), 10.1783 ± 1.2574 (SUB), 1.3175 ± 0.1816 (MS-DB); the CSI values of WT middle-age group are 0.2302 ± 0.0286 (CA1_rad), 6.5282 ± 0.5425 (SUB), 1.0204 ± 0.1924 (MS-DB). Age-related connectivity differences are more frequently observed in 5xFAD mice. For 5xFAD young and 5xFAD middle-age mice, CA1_py, CA2_py, MS-DB, RSC, Vis cortex, Aud cortex and TeA regions all show significantly weaker connections in 5xFAD middle-age relative to 5xFAD young mice (Fig. 8D) (Wilcoxon rank-sum test, $p = 1\times10^{-5}$, $p = 5.6\times10^{-4}$, $p = 4.03\times10^{-3}$, $p = 4.46\times10^{-2}$, $p = 1.2\times10^{-3}$, $p = 8.1\times10^{-4}$, $p = 6.45\times10^{-3}$, respectively). The CSI values of the 5xFAD young group are 40.7620 ± 2.3022 (CA1_py), 0.8725 ± 0.0868 (CA2_py), 0.9410 ± 0.1071 (MS-DB), 1.4492 ± 0.3497 (RSC), 5.2217 ± 1.6207 (Vis cortex), 0.8048 ± 0.2012 (Aud cortex) and 0.3566 ± 0.0686 (TeA); the CSI values of 5xFAD middle-age group are 13.8835 ± 1.3216 (CA1_py), 0.4024 ± 0.0506 (CA2_py), 0.4593 ± 0.0628 (MS-DB), 0.6619 ± 0.2547 (RSC), 0.5301 ± 0.2877 (Vis cortex), 0.0672 ± 0.0390 (Aud cortex) and 0.0888 ± 0.0291 (TeA). To show the CSI values of specific impacted regions for all four mouse groups, example regions are plotted (Fig. 8E). Interestingly, the CSI value of the visual cortex in the 5xFAD young group is much higher than in WT young and 5xFAD middle-age mice. Together, these data demonstrate significant alterations in presynaptic connectivity strength to SUB excitatory neurons

in 5xFAD mice compared to WT mice. Moreover, these connectivity alterations show age-progressive features in WT and especially in 5xFAD mice.

Quantitative analyses of regional-specific SUB input pattern changes in 5xFAD mice

To investigate whether the SUB input connectivity patterns shift in 5xFAD mice with their significantly altered connectivity, we measured the proportion of input (PI) index based on the proportion of each input region for the total inputs (Fig. 9). The PI index is represented by the fraction of presynaptic neurons in each input region over the entire brain inputs and provides a more global measure of connectivity contribution for a given region. For comparison between WT young and 5xFAD young mice, the 5xFAD young mice show significantly higher PI values in the visual cortex (Fig. 9A) ($p = 1.93\times10^{-2}$). The PI values of WT young and 5xFAD young mice are 1.9859 ± 0.9604 and 7.6444 ± 2.2371, respectively. For WT middle-age and 5xFAD middle-age mice, 5xFAD middle-age mice show significantly lower PI values in CA1_py and Aud cortex ($p = 1.2\times10^{-3}$, $p = 2.66\times10^{-2}$, respectively), and show significantly higher PI values in CA1_lmol, CA3_or, and SUB ($p = 2.75\times10^{-2}$, $p = 6.01\times10^{-3}$, $p = 7\times10^{-5}$, respectively) (Fig. 9B). The PI values for WT middle-age are 64.8701 ± 2.4048 (CA1_py), 0.9941 ± 0.4759 (Aud cortex), 0.1572 ± 0.0393(CA1_lmol), 0.0992 ± 0.0186 (CA3_or), 14.8686 ± 1.5137 (SUB). The PI values for 5xFAD middle-age are 51.0676 ± 2.1452 (CA1_py), 0.2911 ± 0.1738 (Aud cortex), 0.4002 ± 0.1152 (CA1_lmol), 0.2486 ± 0.0324 (CA3_or), 27.5509 ± 1.5691 (SUB). For comparisons between ages, WT young mice show lower PI values in CA1_rad than WT middle-age mice (Fig. 9C) ($p = 1.79\times10^{-2}$). The PI values of WT young and WT middle-age mice are 0.2115 ± 0.0556, and 0.5114 ± 0.0625, respectively. Compared to 5xFAD young mice, 5xFAD middle-age mice show significantly lower connections in CA1_py, Vis cortex, Aud cortex ($p = 1.2\times10^{-3}$, $p = 1.37\times10^{-2}$, $p = 1.32\times10^{-2}$, respectively), and higher PI values in CA1_rad, CA1_lmol, CA3_or, and SUB ($p = 1.79\times10^{-2}$, $p = 1.76\times10^{-2}$, $p = 1.79\times10^{-2}$, $p = 5.0\times10^{-5}$, respectively) (Fig. 9D). The PI values of 5xFAD young group are 63.0325 ± 1.8142 (CA1_py), 7.6444 ± 2.2371 (Vis cortex),1.2035 ±

0.2885 (Aud cortex), 0.1582 ± 0.0507 (CA1_rad), 0.1127 ± 0.0514 (CA1_lmol), 0.1258 ± 0.0258 (CA3_or), and 13.8588 ± 1.4307 (SUB). The PI values of 5xFAD middle-age group are 51.0676 ± 2.1452 (CA1_py), 2.2177 ± 1.2674 (Vis cortex), 0.2911 ± 0.1738 (Aud cortex), 0.4526 ± 0.0978 (CA1_rad), 0.4002 ± 0.1152 (CA1_lmol), 0.2486 ± 0.0324 (CA3_or), and 27.5509 ± 1.5691 (SUB). To show the PI values of specific impacted regions for all four mouse groups, example regions are plotted (Fig. 9E). Notably, the SUB PI of the 5xFAD middle-age group is higher than the other three mouse groups. Together, these data support the idea that compensatory circuit input changes may occur in response to connectivity losses in AD conditions.

Sex-specific differences in SUB input connectivity strengths and patterns

In human patients, AD is more common in females than males on an age-matched basis (Seshadri et al., 1997). We asked whether sex differences in SUB neuron connectivity strengths and patterns may be recapitulated in the 5xFAD mouse model. The CSI and PI values were compared between male and female mice for each group pair (Fig. 10, Tables 3.5 and 3.6). Significant sex differences are observed in all four groups of mice when comparing CSI and PI values. Specifically, for the WT young group, male mice show higher CSI values than female mice for MS-DB ($p = 3.57\times10^{-2}$), and lower PI values in postSUB ($p = 3.57\times10^{-2}$) (Table 3.6). For the WT middle-age group, male mice show higher CSI values in CA2_or, CA3_or, and SUB ($p = 3.17\times10^{-2}$, $p = 7.9\times10^{-3}$, $p = 3.17\times10^{-2}$, respectively). WT middle-age male mice show higher PI values than females in CA3_or, SUB ($p = 3.17\times10^{-2}$, $p = 3.17\times10^{-2}$, respectively) (Table 3.6). For 5xFAD mice, there are more sex differences (Fig. 10). For the 5xFAD young group, male mice show higher CSI values CA1_or, CA3_py ($p = 1.9\times10^{-2}$, $p = 3.81\times10^{-2}$, respectively), and lower CSI values in postSUB and MEC ($p = 1.9\times10^{-2}$, $p = 3.81\times10^{-2}$, respectively). 5xFAD young male mice show higher PI values in CA1_or, CA2_py, and lower CSI values in postSUB than female mice ($p = 3.81\times10^{-2}$, $p = 3.81\times10^{-2}$, $p = 3.81\times10^{-2}$, respectively). For the 5xFAD middle-age group, male mice show higher CSI values than female mice in Prh, LEC, and MEC ($p = 1.01\times10^{-2}$, p =

3.03×10^{-2}, $p = 3.03\times10^{-2}$, respectively). For PI values, 5xFAD middle-age male mice show higher PI values than female mice in Prh, LEC and MEC ($p = 5.1\times10^{-3}$, $p = 3.03\times10^{-2}$, $p = 1.77\times10^{-2}$, respectively). Overall, there are significant sex differences in multiple brain regions, and this sex difference is more prominent in 5xFAD mice than WT mice for both ages. These results indicate that the circuit connections to SUB excitatory neurons from different brain regions may be differentially impacted by sex-related factors, especially in 5xFAD mice.

Discussion

While past work focused on neuropathological features, AD is increasingly considered as a neural circuit disorder. In the work described above, we applied the monosynaptic rabies tracing approach to investigate alterations in neural circuit connectivity of SUB excitatory neurons in age-matched, gender-balanced WT and 5xFAD mice. Our immunostaining results of the SUB region are in strong agreement with 5xFAD neuropathology data reported in previously published studies (Jawhar et al., 2012; Oakley et al., 2006). In parallel to our immunostaining results that show age-progressive amyloid deposition of SUB in 5xFAD mice, our monosynaptic rabies virus tracing reveals pathological impairments of excitatory SUB input connectivity. We mapped and compared local and long-range presynaptic inputs to SUB excitatory neurons from multiple brain regions in age-matched WT and 5xFAD mouse groups at young and middle ages. Quantification of the age-matched WT and 5xFAD SUB neural tracing reveals age- and genotype-dependent alterations. Our results also demonstrate prominent sex differences in AD-induced circuit connectivity alterations.

Our monosynaptic rabies tracing method is robust, as it works through a highly specific interaction between the TVA receptor and EnvA pseudotyped rabies. To ensure the precise labeling of the dorsal SUB, we used a small amount of helper AAV (0.05 μL) to prevent leaky labeling of starter cells outside the SUB, followed by a typical amount of 0.4 μL of EnvA pseudotyped RV injection, which was established in previous protocols (Lin et al., 2021; Ye et al.,

2022). Moreover, cortical rabies labeling indeed reflects the presynaptic input labeling of SUB starter neurons, instead of leaky labeling. This is because of the technical nature of our monosynaptic rabies tracing approach. In our SUB experiments, only the starter cells in the SUB can take up EnvA-ΔG rabies virus, as they have the required TVA receptor expression. However, the cortical cells and their axons do not express TVA, thus technically they cannot be directly infected and labeled by EnvA-pseudotyped rabies virus. This is verified by our control experiments of single injections of pseudotyped rabies virus alone that did not yield artifactual labeling. In our previously published studies and others investigating hippocampal CA1 circuitry using monosynaptic rabies tracing, no rabies labeling was observed in the cortex above the CA1 injection site, arguing against the possibility that pseudotyped rabies virus infects through the damaged axons and other processes that would bypass the EnvA-mediated specificity (Sun et al., 2014; Tao et al., 2021; Ye et al., 2022). Overall, the presynaptic input regions identified by this study and the CSI values of the WT young group are generally concordant with an earlier SUB rabies tracing study using a CaMK2a-Cre; TVA mouse line (Sun et al., 2019), with the strongest input from hippocampal CA1, and significant inputs from the EC, visual, auditory cortex and other regions. We observed robust labeling from the visual cortex and somatosensory cortex. These observations are supported by the Allen Brain Connectivity and Janelia MouseLight datasets (Oh et al., 2014; Winnubst et al., 2019), where AAV injections from the visual cortex and somatosensory cortex result in axon labeling in the SUB region. Note that we do not anticipate that the rabies tracing method labels every input to each neuron with 100% efficiency. Nevertheless, the rabies virus tracing technique used in this study holds significant promise as a powerful tool for quantitatively assessing connectivity when comparing between WT and AD model mice.

In the current study, we identify substantial non-canonical inputs from hippocampal CA3, which has not been reported previously. Moreover, this study provides the first viral genetic-based anatomical evidence verifying that SUB neurons receive strong recurrent connections, supporting

earlier anatomy and whole-cell recording studies (Bohm et al., 2015; Harris et al., 2001). Our Cre-dependent viral strategy facilitates precise mapping of the local SUB circuitry because this molecular tool restricts the expression of optimized rabies glycoprotein (oG) and the highly specific TVA receptor (TC66T) exclusively within CaMKII+ SUB neurons. Therefore, the presynaptic labeled SUB neurons are indeed local input neurons, eliminating any artifactual possibility of leakage. Furthermore, our results demonstrate that the local intrinsic connections to SUB excitatory neurons are resistant in AD, as the CSI values of the WT and 5xFAD groups at both ages are consistent. However, the proportional input of SUB local connection in the AD middle-age group is significantly higher due to the decrease of other input regions, indicating a potential compensatory effect of AD on SUB connections.

It is noteworthy that the visual cortical inputs to SUB show a significantly increased connectivity in young 5xFAD mice compared to WT mice, followed by decreased connectivity in middle-age 5xFAD mice. It is increasingly recognized that early stages of AD are characterized by neuronal hyperexcitability, followed by a transition towards hypo-excitability at later ages. Therefore, the increased connectivity of the visual cortex to SUB in young AD mice may be attributed to enhanced synaptic connection strengths due to hyperexcitability in the initial phases of the disease, as an earlier study shows that rabies labeling may be activity-dependent (Beier et al., 2017). The visual cortex is generally considered an understudied brain region in AD. However, recently increasing evidence suggests that the visual cortex may be functionally implicated in AD. It has been shown that 40 Hz gamma frequency entrainment attenuates amyloid load in the visual cortex and hippocampal CA1 of young 5xFAD mice, reduces neuron and spine loss, and improves behavioral performance (Iaccarino et al., 2016). This indicates a potential functional network between the visual cortex and the hippocampal formation system. Indeed, a previous study shows that the projection from the visual cortex to SUB is implicated in object location memory (Sun et al., 2019). 5xFAD mice display impairment of object location memory at 8-10 months but not 4-5

months old (Zhang et al., 2023). This implies that the impairment of visual cortex inputs to SUB could be involved in spatial and object-related learning and memory deficits.

Importantly, our viral tracing results demonstrate prominent sex differences in circuit alterations in 5xFAD mice. In human patients, the risk of women having AD is higher than in men due to a series of factors such as longevity, hormonal level, genetics, inflammation, and other sociocultural factors (Nebel et al., 2018; Zhu et al., 2021). While the underlying mechanism of the sex difference remains elusive, there is evidence showing that the association between AD pathology and clinical AD was substantially stronger in women than in men (Barnes et al., 2005). Moreover, a study has shown that women had higher CSF total tau and Aβ42 levels, more rapid cognitive decline, and hippocampal atrophy, indicating that they experience worse pathologic alterations than men (Koran et al., 2017). Differences between sexes were also revealed by transcriptomic analysis of AD-pathology-associated marker genes and females show higher expression (Mathys et al., 2019). In this study, the amyloid quantification shows that female mice exhibit more severe amyloid plaques and intraneuronal accumulation in both young and middle-age 5xFAD mice. Importantly, there are notable disparities in neural circuit connectivity to the SUB between the sexes. The sex-specific impacted regions are primarily hippocampal subregions, postSUB, Prh, and EC: all of these areas are critical for learning and memory. Interestingly, in young 5xFAD mice, female mice show higher connectivity than male mice in certain regions. However, in middle-age 5xFAD mice, female mice all show weaker connectivity compared to male mice for regions with sex differences. This further implies sex-specific differences in the timing of hyperexcitability in young 5xFAD mice.

Together, our research shows significant connectivity strength alterations and connectivity pattern shifts in AD model mice. These new findings may provide valuable insights into addressing AD neural mechanisms as a neural circuit disorder. The sex-specific differences are interesting and may offer a new perspective to tackle this disease. Future neural circuit studies could pave

the way for improved therapeutic interventions that may slow down or mitigate this disease during its early stages in Alzheimer's patients.

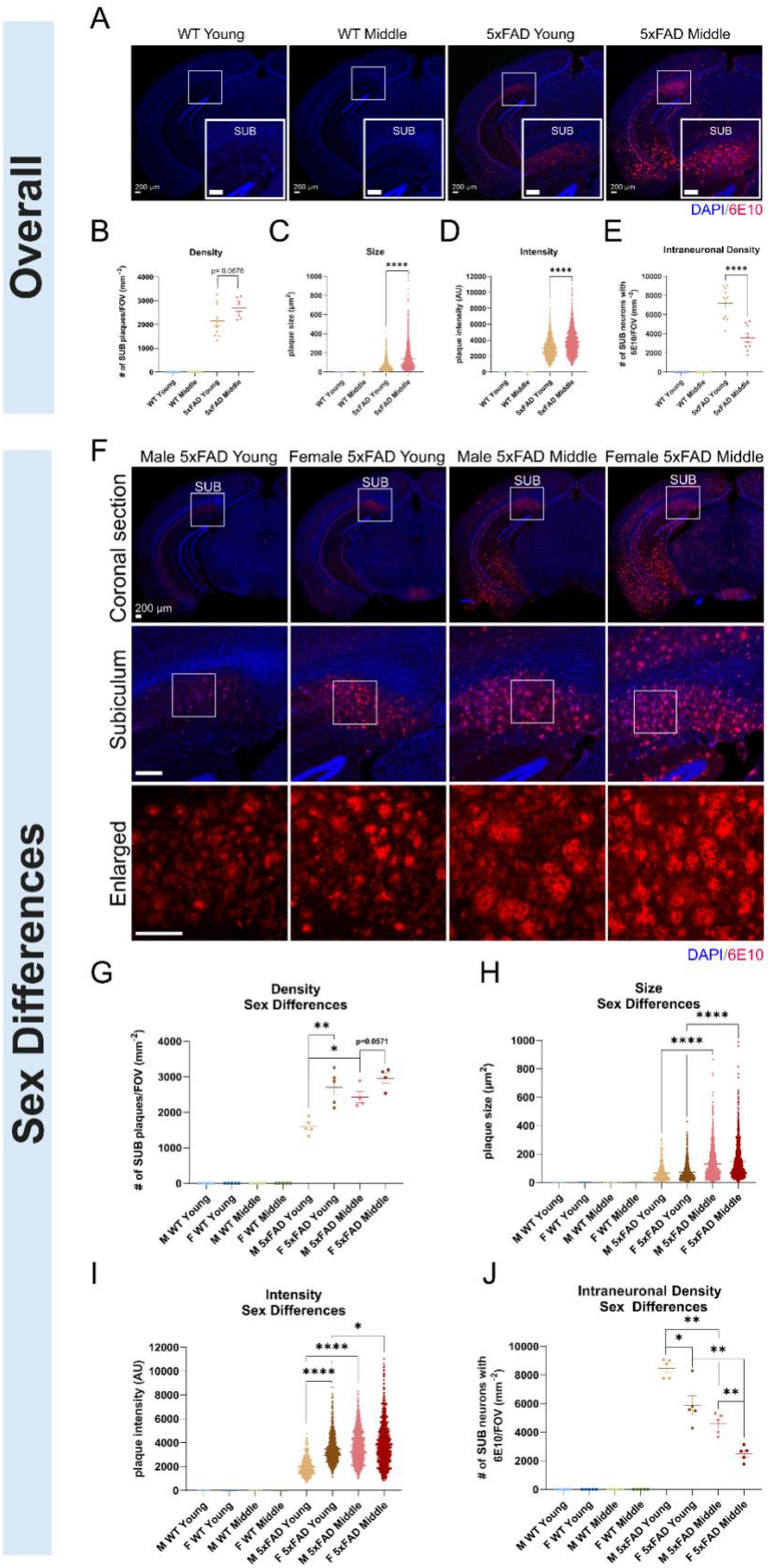
Overall
Sex Differences
A
WT Young
WT Middle
5xFAD Young
5xFAD Middle
SUB
200 µm
DAPI/6E10
B
Density
C
Size
D
Intensity
E
Intraneuronal Density
F
Male 5xFAD Young
Female 5xFAD Young
Male 5xFAD Middle
Female 5xFAD Middle
Coronal section
Subiculum
Enlarged
G
Density
Sex Differences
# of SUB plaques/FOV (mm⁻²)
H
Size
Sex Differences
plaque size (µm²)
I
Intensity
Sex Differences
plaque intensity (AU)
J
Intraneuronal Density
Sex Differences
# of SUB neurons with 6E10/FOV (mm⁻²)
M WT Young
F WT Young
M WT Middle
F WT Middle
M 5xFAD Young
F 5xFAD Young
M 5xFAD Middle
F 5xFAD Middle

Figure 3.1 Age-progressive Aβ neuropathology in 5xFAD mice

6E10 immunostaining and quantification in age-matched WT and 5xFAD for both ages. ***A***, Representative images of 6E10 amyloid antibody immunostained plaques and neurons in young and middle age-matched WT and 5xFAD mice. The four panels show coronal brain sections. The large white squares show an enlarged view of the SUB outlined by the smaller white squares. DAPI staining is in blue, and the 6E10+ amyloid signal is in red. ***B-E,*** Quantification of extracellular and intraneuronal 6E10 signals in SUB. More amyloid plaques were detected in 5xFAD middle-age mice relative to 5xFAD young, while none were detected in both age groups of WT mice. 5xFAD middle-age mice show slightly higher plaque density, and significantly greater plaque size and intensity relative to 5xFAD young mice (***B***, density, 5xFAD young: 2151 ± 214.3, 5xFAD middle-age: 2698 ± 141.8, Wilcoxon rank-sum test, $p = 0.0676$; ***C***, size, 5xFAD young: 73.59 ± 1.645, 5xFAD middle-age: 139.9 ± 2.247, linear mixed effects model, $p = 1.86\times10^{-12}$; ***D***, intensity, 5xFAD young: 3018 ± 33.42, 5xFAD middle-age: 3761 ± 30.54, linear mixed effects model, $p = 9.13\times10^{-7}$). ***E,*** 5xFAD young mice have significantly greater intraneuronal 6E10 density relative to 5xFAD middle-age (density, 5xFAD young: 7188±548.1, 5xFAD middle-age: 3554±396.7, Wilcoxon rank-sum test, $p = 7.58\times10^{-5}$). The mouse numbers for each of the 4 groups of WT and 5xFAD mice of both ages are n = 10. ***F-H***, Sex-specific comparison of 6E10 immunostaining. ***F***, Representative images of DAPI and 6E10 antibody immunostaining in 5xFAD mice of both age groups and genders. The first row of panels shows coronal brain sections with DAPI and 6E10 amyloid antibody immunostaining. The second row of panels shows an enlarged view of the SUB outlined by the smaller white squares in the first row. The third row of panels shows an even larger view of the white squares in the second row. ***G-J***, Quantification of sex differences in SUB 6E10 stained amyloid plaques and neurons. ***G***, There is a significant increase of extracellular plaque density in young female 5xFAD and middle-age male 5xFAD compared to male 5xFAD young mice. There is a significant age-dependent increase of extracellular plaque density in male mice, but not female mice (density, male 5xFAD young: 1601 ± 94.84, female 5xFAD young: 2702 ± 214.6, male 5xFAD middle-age: 2432±157.5, female 5xFAD middle-age: 2963 ± 148.6, Wilcoxon rank-sum test, male 5xFAD young vs. female 5xFAD young, $p = 0.0079$, male 5xFAD young vs. male 5xFAD middle-age, $p = 0.0159$, male 5xFAD middle-age vs. female 5xFAD middle-age, $p = 0.0571$). ***H***, For both genders of 5xFAD mice, the middle-age mice have significantly greater extracellular plaque size relative to the young mice, revealing that plaque size has an age-dependent increase within the same sex (size, male 5xFAD young: 68.69 ± 2.734, female 5xFAD young: 74.3 ± 2.022, male 5xFAD middle-age: 130.4 ± 2.917, female 5xFAD middle-age: 149.8 ± 3.421, linear mixed effects model, male 5xFAD young vs. male 5xFAD middle-age: $p = 2.63\times10^{-11}$, female 5xFAD young vs. female 5xFAD middle-age: $p = 5.81\times10^{-6}$). ***I***, There is a significant age-dependent increase in extracellular plaque intensity within the same sex and a significant sex-dependent increase only in 5xFAD young mice (male 5xFAD young: 1985 ± 35.98, female 5xFAD young: 3473 ± 37.11, male 5xFAD middle-age: 3718 ± 37.67, female 5xFAD middle-age: 3805 ± 48.52, linear mixed effects model, male 5xFAD young vs. male 5xFAD middle-age: $p = 1.39\times10^{-23}$, female 5xFAD young vs. female 5xFAD middle-age, $p = 0.01184$, male 5xFAD young vs. female 5xFAD young: $p = 6.76\times10^{-16}$). ***J***, There is a significant sex and age-dependent decrease in intraneuronal 6E10 stained neuron density in 5xFAD mice. In both male and female 5xFAD mice, middle-age mice have significantly less intraneuronal neuron density than young mice. In 5xFAD mice of the same age group (young or middle), the female mice have significantly less intraneuronal neuron density (density, male 5xFAD young: 8479 ± 293.9, female 5xFAD young: 5896 ± 656.4, male 5xFAD middle-age: 4603 ± 323.5, female 5xFAD middle-age: 2506 ± 232.0, Wilcoxon rank-sum test, male 5xFAD young vs. female 5xFAD young: $p = 0.0317$, male 5xFAD middle-age vs. female 5xFAD middle-age: $p = 0.0079$, male 5xFAD young vs. male 5xFAD middle-age: $p = 0.0079$, female 5xFAD young vs. female 5xFAD middle-age: $p = 0.0079$). The mouse numbers for each of the 8 groups (two age groups, male and female, WT and 5xFAD) are 4-5. One representative section was used for quantification for each mouse brain (Fig. 1B-E, G-

J). Sample sizes for the linear mixed effects model are based on both the mouse numbers and the number of individual plaques measured from each mouse brain (Fig. 1C, D, H, and I) (5xFAD young male n=432, 5xFAD young female n=980, 5xFAD middle male n=1321, 5xFAD middle female n=1255). Scale bars are included in the figure panels. The unit for plaque size is μm^2, plaque density is per mm^2, and the intensity is arbitrary unit (AU) of optical density. Statistical significances are denoted by * $p \leq 0.05$, ** $p \leq 0.01$, *** $p \leq 0.001$, **** $p \leq 0.0001$.

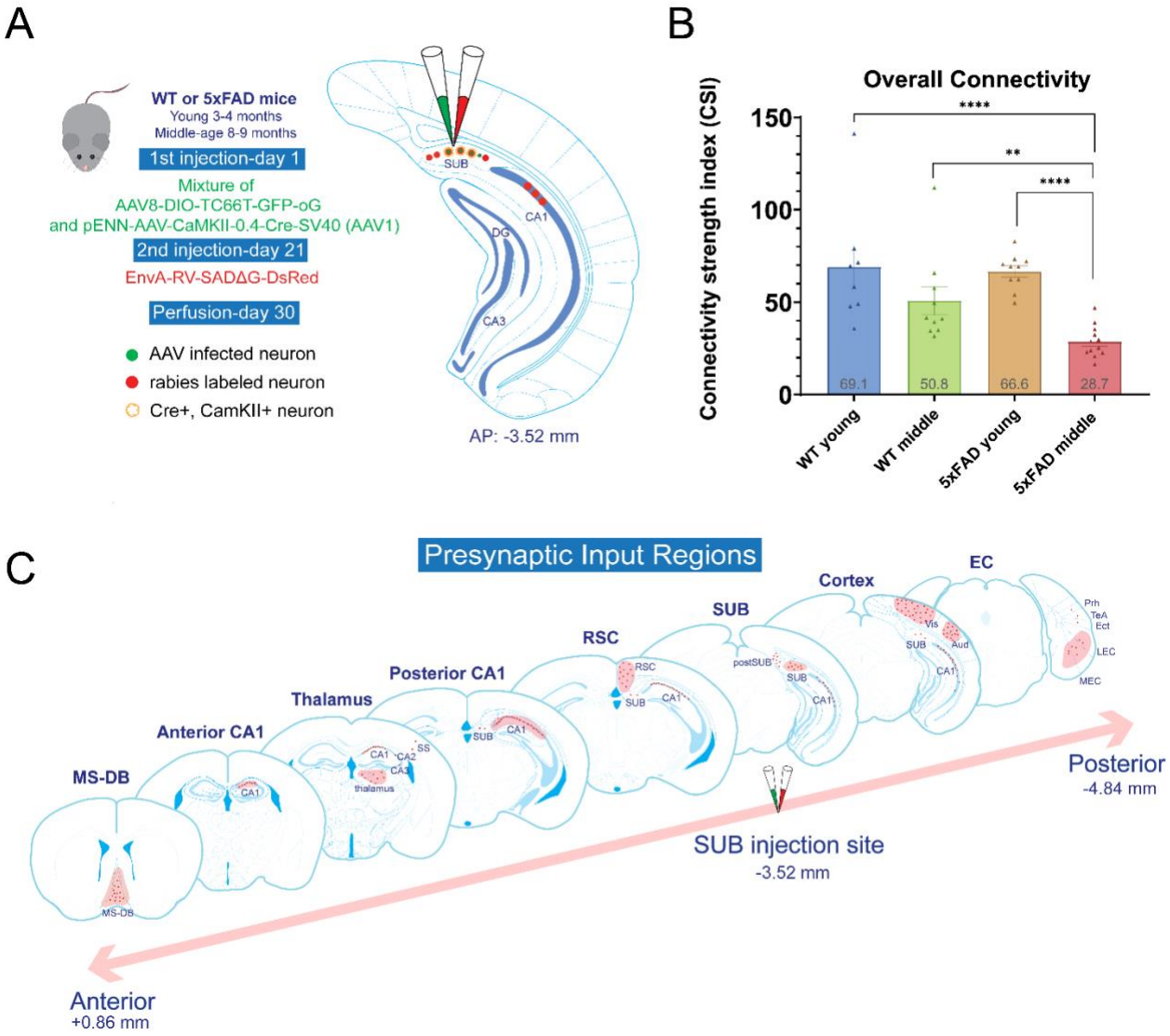

Figure 3.2 Brain-wide presynaptic inputs to SUB excitatory neurons revealed by monosynaptic rabies tracing

A, Schematic of cell-type-specific retrograde monosynaptic rabies tracing. To specifically label excitatory SUB neurons, the AAV helper virus (AAV-DIO-TC66T-GFP-oG and AAV-CaMKII-Cre), labeled green, was injected into the dorsal SUB, followed 20 days later at the same site by an injection of rabies virus (EnvA-RV-SADΔG-DsRed), labeled red. The neurons labeled both green and red represent the starter neurons. The neurons labeled only red represent the presynaptic inputs to the starter neurons. Nine days after rabies injection, the mice were perfused for further analysis. ***B***, Overall brain connectivity strength index (CSI) for WT young (n = 8), WT middle-age (n = 10), 5xFAD young (n = 10), and 5xFAD middle-age (n = 12) group (69.1 ± 11.5, 50.8 ± 7.6, 66.6 ± 3.1, 28.7 ± 2.5, respectively). The CSI is defined as the number of input neurons normalized

by the number of starter neurons. The 5xFAD middle-age group has a significantly lower CSI than the WT young, WT middle-age, and 5xFAD young group (Wilcoxon rank-sum test, $p = 6.35 \times 10^{-5}$, $p = 1.13 \times 10^{-3}$, $p = 3.09 \times 10^{-6}$, respectively). Data are presented as mean ± SEM. Statistical significances are denoted by * p≤0.05, ** p≤0.01, *** p≤0.001, **** p≤0.0001. ***C***, Coronal sections of major input regions to SUB excitatory neurons arranged along the anterior-to-posterior (AP) axis, including medial septum and diagonal band (MS-DB), anterior and posterior CA1, thalamus, retrosplenial cortex (RSC), subiculum (SUB), visual (Vis) cortex, auditory (Aud) cortex and entorhinal cortex (EC). The major input regions are labeled in red-shaded areas. Other input regions such as CA2, CA3, post subiculum (postSUB), somatosensory (SS) cortex, perirhinal cortex (Prh), temporal association cortex (Tea), and ectorhinal cortex (Ect) are labeled as well. The injection site is denoted along the AP axis. Red color labels represent presynaptic input neurons.

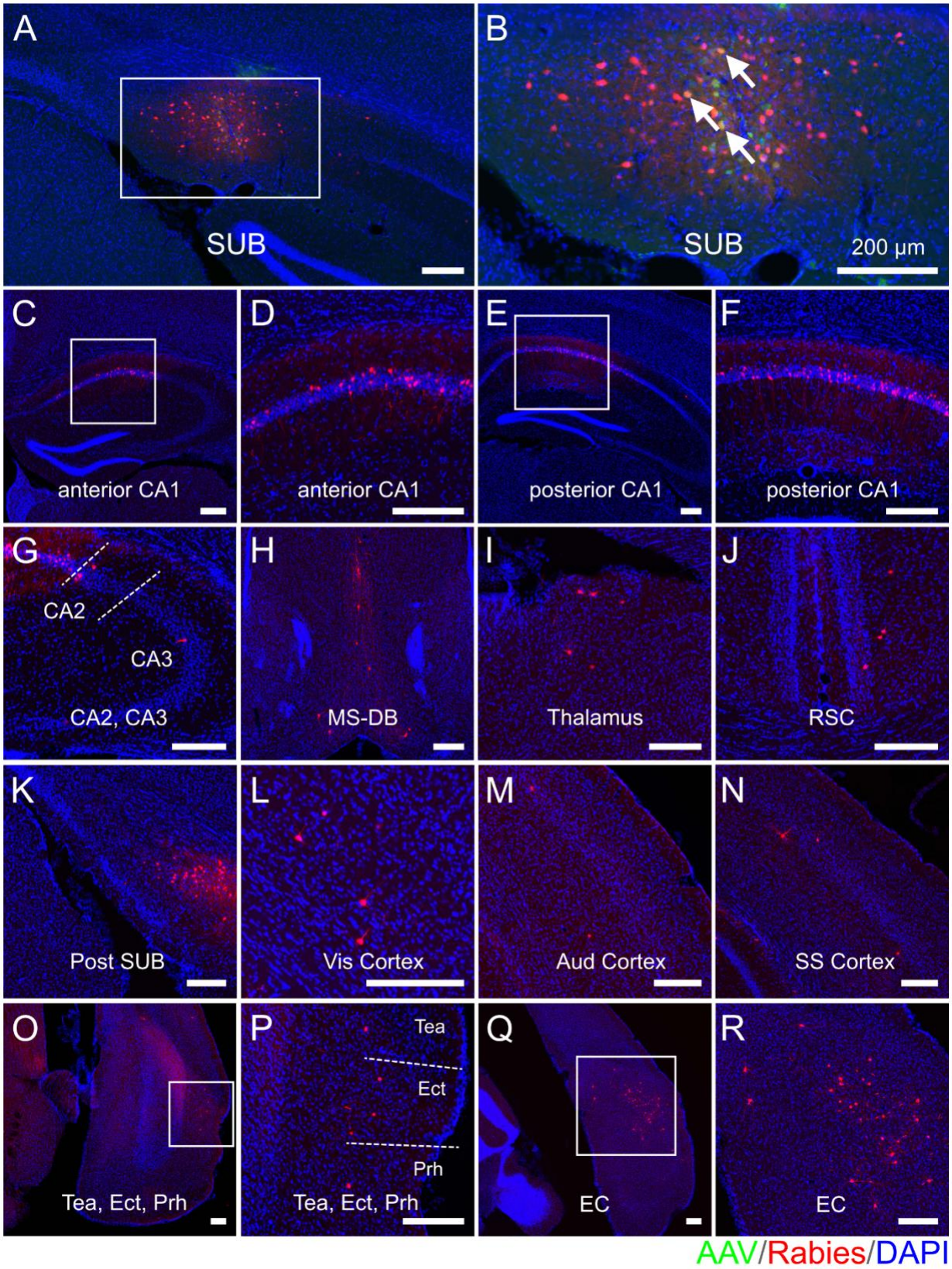
A
SUB
B
SUB
200 μm
C
anterior CA1
D
anterior CA1
E
posterior CA1
F
posterior CA1
G
CA2
CA3
CA2, CA3
H
MS-DB
I
Thalamus
J
RSC
K
Post SUB
L
Vis Cortex
M
Aud Cortex
N
SS Cortex
O
Tea, Ect, Prh
P
Tea
Ect
Prh
Tea, Ect, Prh
Q
EC
R
EC
AAV/Rabies/DAPI

Figure 3.3 Monosynaptic rabies tracing maps region-specific inputs to excitatory SUB cells in young WT mice

Representative fluorescent coronal section images from the WT young group. ***A***, Dorsal SUB injection site. Rabies virus-infected neurons are labeled by DsRed, and AAV-infected neurons are labeled by EGFP. ***B***, Enlarged view of SUB injection site, including white arrows to represent starter neurons. Starter neurons are labeled both red (RV) and green (AAV) fluorescent proteins. ***C-R***, Major presynaptic input regions of SUB mapped by rabies virus-mediated retrograde monosynaptic tracing. The input regions include the SUB (***A, B***), anterior CA1 (***C, D***), posterior CA1 (***E, F***), CA2 & CA3 (***G***), MS-DB (***H***), thalamus (***I***), RSC (***J***), postSUB (***K***), Vis cortex (***L***), Aud cortex (***M***), SS cortex (***N***), Tea & Ect & Prh (***O, P***), and EC (***Q, R***). (***D***), (***F***), (***P***), and (***R***) are enlarged views of the white boxes in (***C***), (***E***), (***O***), and (***Q***), respectively. All slices are counterstained by DAPI in blue. Scale bars labeled for each panel represent 200 μm.

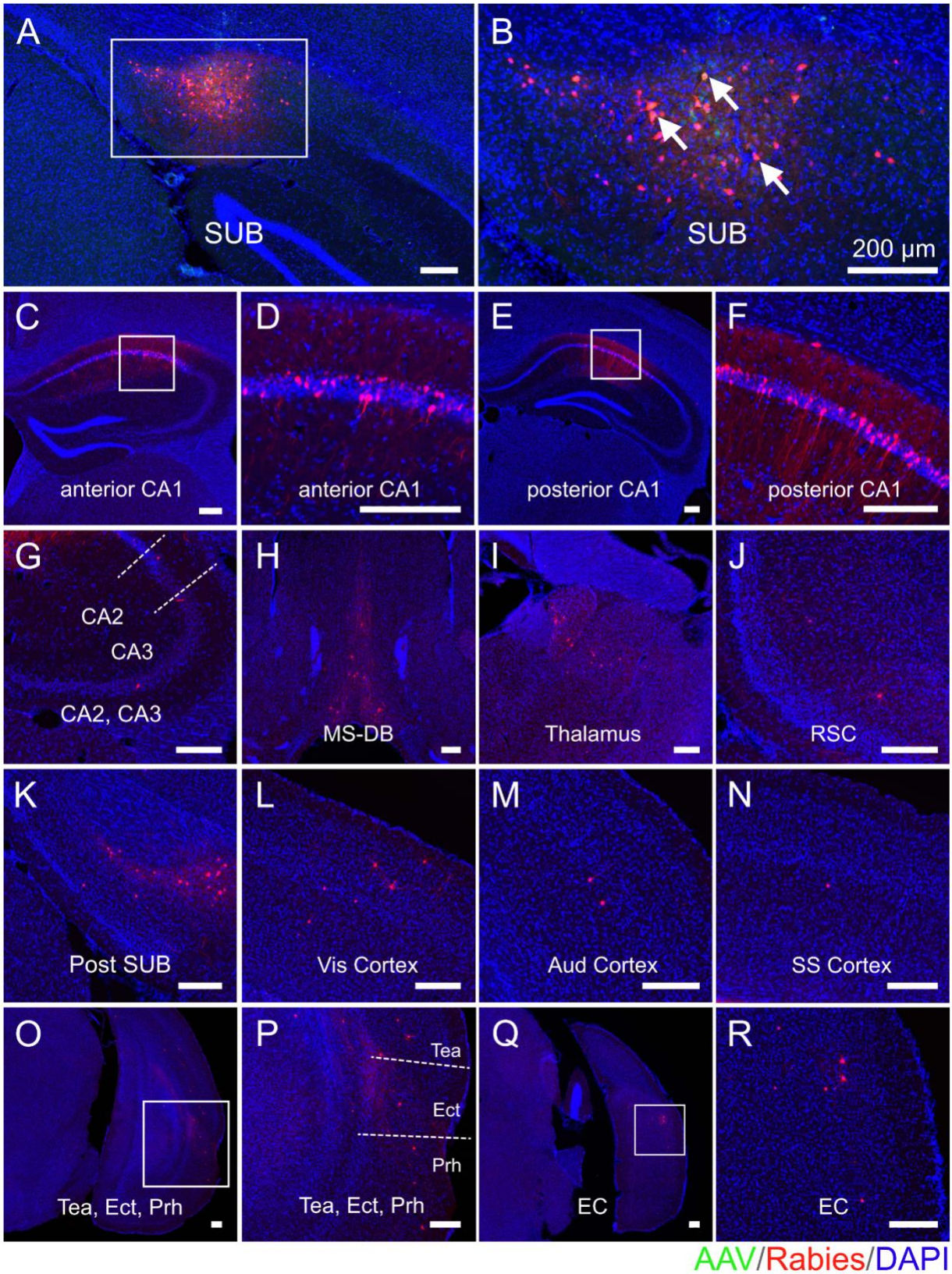
A
SUB
B
SUB
200 μm
C
anterior CA1
D
anterior CA1
E
posterior CA1
F
posterior CA1
G
CA2
CA3
CA2, CA3
H
MS-DB
I
Thalamus
J
RSC
K
Post SUB
L
Vis Cortex
M
Aud Cortex
N
SS Cortex
O
Tea, Ect, Prh
P
Tea
Ect
Prh
Tea, Ect, Prh
Q
EC
R
EC
AAV/Rabies/DAPI

Figure 3.4 Monosynaptic rabies tracing maps region-specific inputs to excitatory SUB cells in middle-age WT mice

Representative fluorescent coronal section images from the WT middle-age group. ***A*****,** Dorsal SUB injection site. Rabies virus-infected neurons are labeled by DsRed, and AAV-infected neurons are labeled by EGFP. ***B*****,** Enlarged view of SUB injection site, including white arrows to represent starter neurons. Starter neurons are labeled both red (RV) and green (AAV) fluorescent proteins. ***C-R***, Major presynaptic input regions of SUB mapped by rabies virus-mediated retrograde monosynaptic tracing. The input regions include the SUB (***A, B***), anterior CA1 (***C*****,** ***D***), posterior CA1 (***E*****,** ***F***), CA2 & CA3 (***G***), MS-DB (***H***), thalamus (***I***), RSC (***J***), postSUB (***K***), Vis cortex (***L***), Aud cortex (***M***), SS cortex (***N***), Tea & Ect & Prh (***O, P***), and EC (***Q, R***). (***D***), (***F***), (***P***), and (***R***) are enlarged views of the white boxes in (***C***), (***E***), (***O***), and (***Q***), respectively. All slices are counterstained by DAPI in blue. Scale bars labeled for each panel represent 200 μm.

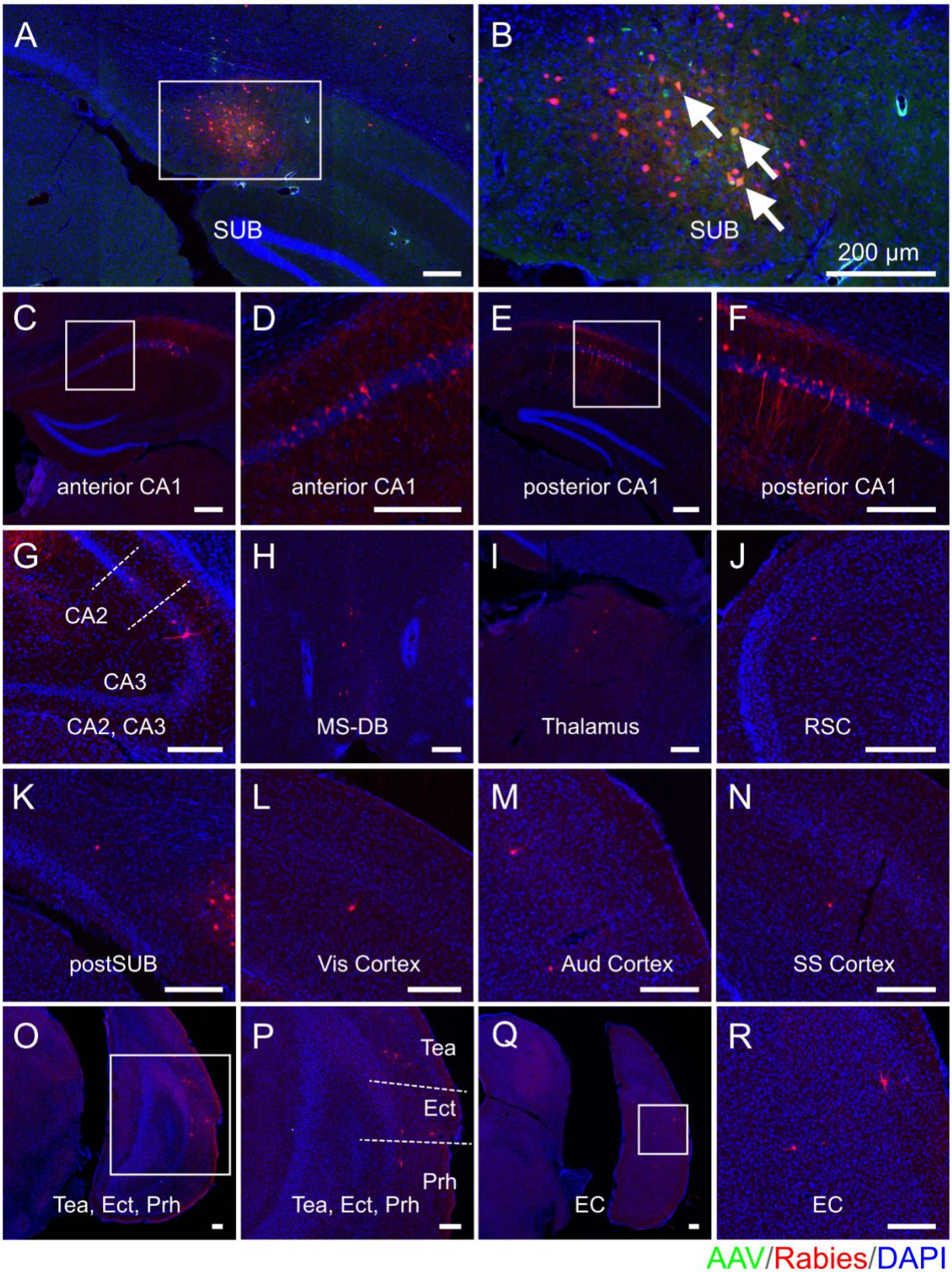
A
SUB
B
SUB
200 μm
C
anterior CA1
D
anterior CA1
E
posterior CA1
F
posterior CA1
G
CA2
CA3
CA2, CA3
H
MS-DB
I
Thalamus
J
RSC
K
postSUB
L
Vis Cortex
M
Aud Cortex
N
SS Cortex
O
Tea, Ect, Prh
P
Tea
Ect
Prh
Tea, Ect, Prh
Q
EC
R
EC
AAV/Rabies/DAPI

Figure 3.5 Monosynaptic rabies tracing maps region-specific inputs to excitatory SUB cells in young 5xFAD mice

Representative fluorescent coronal section images from 5xFAD young group. ***A*****,** Dorsal SUB injection site. Rabies virus-infected neurons are labeled by DsRed, and AAV-infected neurons are labeled by EGFP. ***B*****,** Enlarged view of SUB injection site, including white arrows to represent starter neurons. Starter neurons are labeled both red (RV) and green (AAV) fluorescent proteins. ***C-R***, Major presynaptic input regions of SUB mapped by rabies virus-mediated retrograde monosynaptic tracing. The input regions include the SUB (***A, B***), anterior CA1 (***C*****,** ***D***), posterior CA1 (***E*****,** ***F***), CA2 & CA3 (***G***), MS-DB (***H***), thalamus (***I***), RSC (***J***), postSUB (***K***), Vis cortex (***L***), Aud cortex (***M***), SS cortex (***N***), Tea & Ect & Prh (***O, P***), and EC (***Q, R***). (***D***), (***F***), (***P***), and (***R***) are enlarged views of the white boxes in (***C***), (***E***), (***O***), and (***Q***), respectively. All slices are counterstained by DAPI in blue. Scale bars labeled for each panel represent 200 μm.

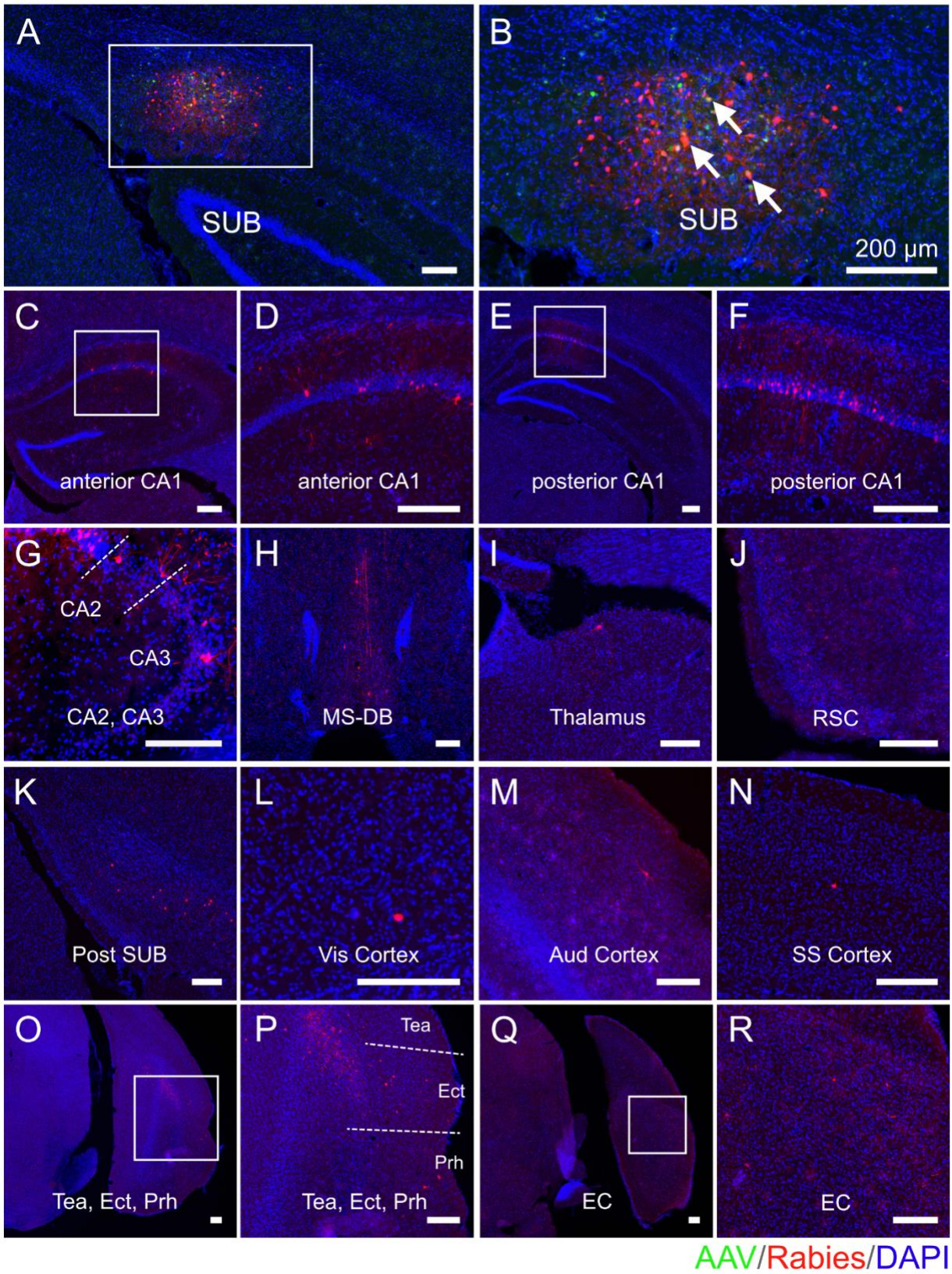
A
SUB
B
SUB
200 μm
C
anterior CA1
D
anterior CA1
E
posterior CA1
F
posterior CA1
G
CA2
CA3
CA2, CA3
H
MS-DB
I
Thalamus
J
RSC
K
Post SUB
L
Vis Cortex
M
Aud Cortex
N
SS Cortex
O
Tea, Ect, Prh
P
Tea
Ect
Prh
Tea, Ect, Prh
Q
EC
R
EC
AAV/Rabies/DAPI

Figure 3.6 Monosynaptic rabies tracing maps region-specific inputs to excitatory SUB cells in middle-age 5xFAD mice

Representative fluorescent coronal section images from 5xFAD middle-age group. ***A*****,** Dorsal SUB injection site. Rabies virus-infected neurons are labeled by DsRed, and AAV-infected neurons are labeled by EGFP. ***B*****,** Enlarged view of SUB injection site, including white arrows to represent starter neurons. Starter neurons are labeled both red (RV) and green (AAV) fluorescent proteins. ***C-R***, Major presynaptic input regions of SUB mapped by rabies virus-mediated retrograde monosynaptic tracing. The input regions include the SUB (***A, B***), anterior CA1 (***C*****,** ***D***), posterior CA1 (***E*****,** ***F***), CA2 & CA3 (***G***), MS-DB (***H***), thalamus (***I***), RSC (***J***), postSUB (***K***), Vis cortex (***L***), Aud cortex (***M***), SS cortex (***N***), Tea & Ect & Prh (***O, P***), and EC (***Q, R***). (***D***), (***F***), (***P***), and (***R***) are enlarged views of the white boxes in (***C***), (***E***), (***O***), and (***Q***), respectively. All slices are counterstained by DAPI in blue. Scale bars labeled for each panel represent 200 μm.

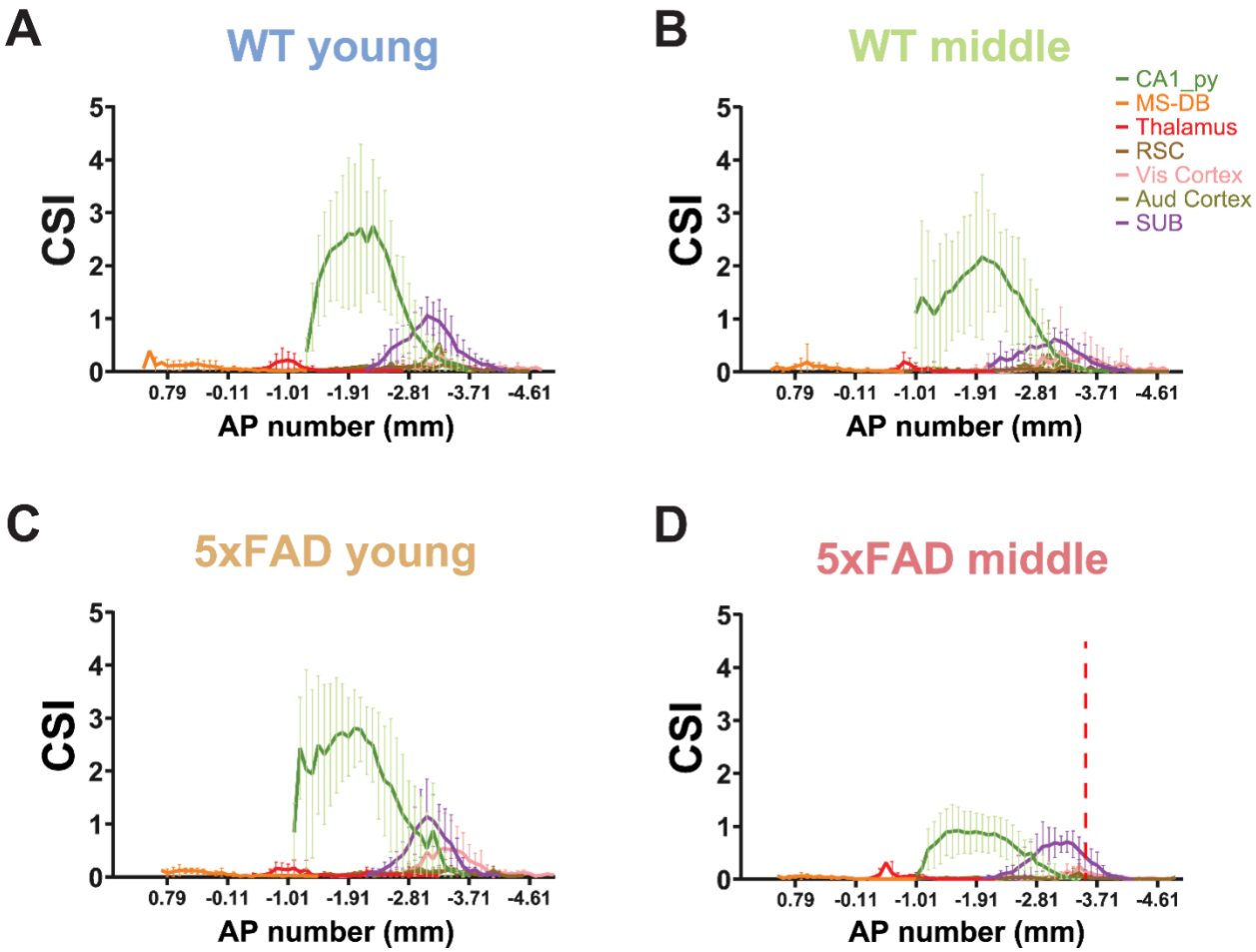

Figure 3.7 Anterior-to-posterior CSI distributions across the brain for different age and genotype groups

The connectivity strength index (CSI) distributions along the AP axis across the whole brain. The CSI is defined as the number of input neurons normalized by the number of starter neurons; the AP positions are given relative to bregma values. Representative input regions were used for the AP plot, including the CA1_py layer, MS-DB, thalamus, RSC, Vis cortex, Aud cortex, and SUB. ***A***, WT young group (n = 8). ***B***, WT middle-age group (n = 10). ***C***, 5xFAD young group (n=10). ***D***, 5xFAD middle-age group (n = 12). The red dashed line at AP = - 3.52 mm shows the position of the viral injection site. There is a significant difference in the CA1_py distribution between WT young and 5xFAD middle-age group (paired Wilcoxon rank-sum test, $p = 1.67 \times 10^{-6}$).

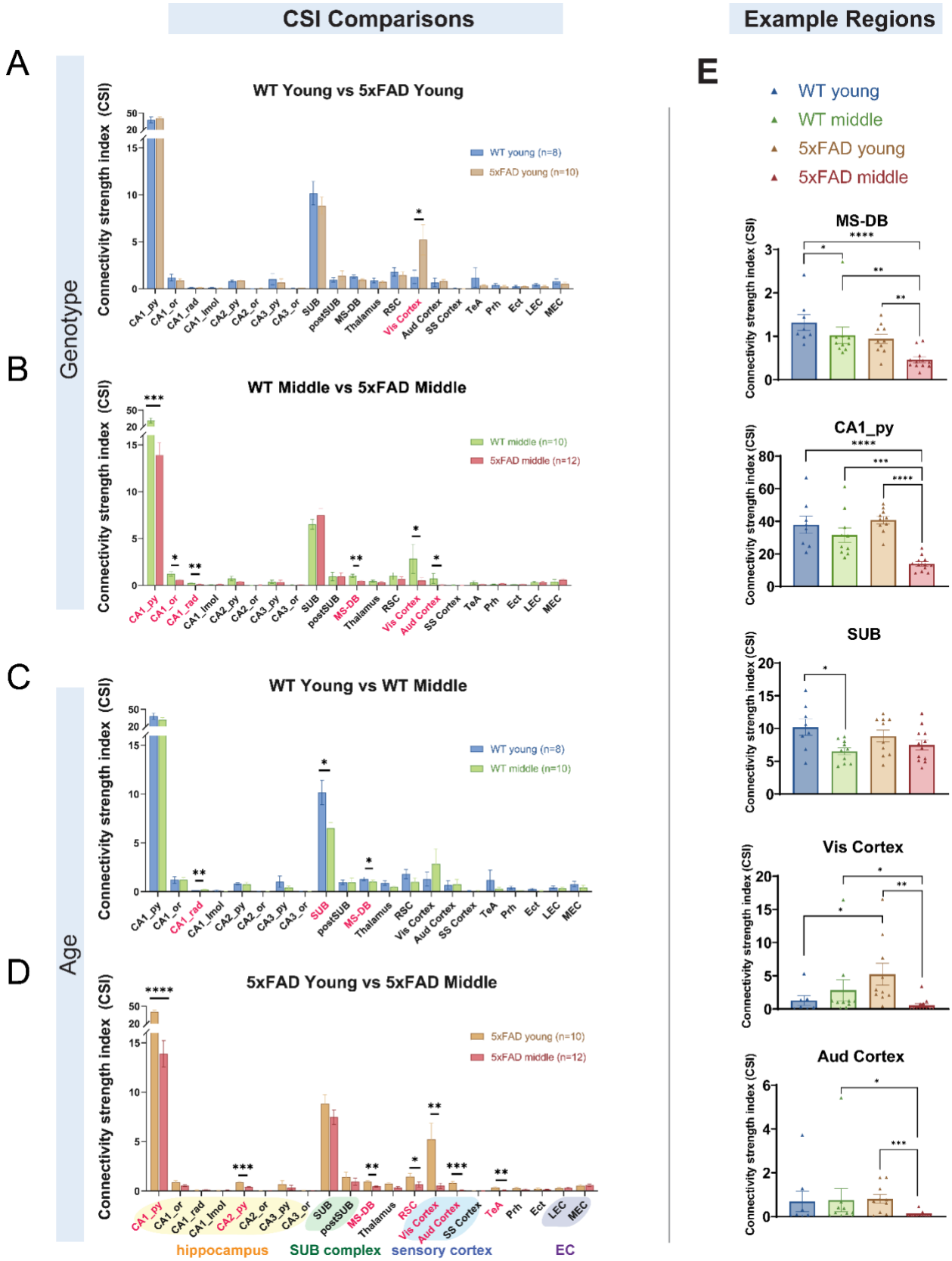
CSI Comparisons
Example Regions
A
B
C
D
E
Genotype
Age
WT Young vs 5xFAD Young
WT Middle vs 5xFAD Middle
WT Young vs WT Middle
5xFAD Young vs 5xFAD Middle
Connectivity strength index (CSI)
WT young (n=8)
5xFAD young (n=10)
WT middle (n=10)
5xFAD middle (n=12)
CA1_py
CA1_or
CA1_rad
CA1_lmol
CA2_py
CA2_or
CA3_py
CA3_or
SUB
postSUB
MS-DB
Thalamus
RSC
Vis Cortex
Aud Cortex
SS Cortex
TeA
Prh
Ect
LEC
MEC
hippocampus
SUB complex
sensory cortex
EC
WT young
WT middle
5xFAD young
5xFAD middle
MS-DB
CA1_py
SUB
Vis Cortex
Aud Cortex

Figure 3.8 Connectivity strength quantification of presynaptic inputs regions to SUB excitatory neurons

Quantitative analysis of SUB connectivity strength index (CSI) values of WT young, WT middle-age, 5xFAD young, and 5xFAD middle-age mice. The CSI is the ratio of the SUB input neuron number in a subregion to the total starter neuron number in a brain. The input regions include hippocampal CA1, CA2, and CA3 sublayers, as well as the SUB, postSUB, thalamus, RSC, Vis cortex, Aud cortex, SS cortex, TeA, Prh, Ect, LEC, and MEC. The regions showing statistical differences are shown in red text. ***A***, WT young mice have significantly lower CSI values relative to 5xFAD young mice in the visual cortex ($p = 1.29\times10^{-2}$). ***B***, WT middle-age mice have significantly higher CSI values relative to 5xFAD middle-age mice in CA1_py, CA1_or, CA1_rad, MS-DB, Vis cortex, and Aud cortex ($p = 1.2\times10^{-4}$, $p = 4.46\times10^{-2}$, $p = 8.78\times10^{-3}$, $p = 3.33\times10^{-3}$, $p = 1.29\times10^{-2}$, $p = 1.38\times10^{-2}$, respectively). ***C***, WT young mice have significantly higher CSI values relative to WT middle-age mice in SUB and MS-DB ($p = 4.66\times10^{-2}$, $p = 2.74\times10^{-2}$, respectively). WT middle-age mice have significantly higher CSI values relative to WT young mice in CA1_rad ($p = 8.78\times10^{-3}$). ***D***, 5xFAD young mice have significantly higher CSI values relative to 5xFAD middle-age mice in CA1_py, CA2_py, MS-DB, RSC, Vis cortex, Aud cortex, and TeA ($p = 1\times10^{-5}$, $p = 5.6\times10^{-4}$, $p = 4.03\times10^{-3}$, $p = 4.46\times10^{-2}$, $p = 1.2\times10^{-3}$, $p = 8.1\times10^{-4}$, $p = 6.45\times10^{-3}$, respectively). ***E***, CSI comparisons of example regions across four groups of mice. Representative regions include MS-DB, CA1_py, SUB, Vis Cortex, and Aud Cortex. The mouse numbers for each group are WT young n = 8, WT middle-age n = 10, 5xFAD young n = 10, and 5xFAD middle-age n = 12. The statistical test is the Wilcoxon rank-sum test. The p values are adjusted with False Discovery Rate (FDR) Benjamini-Hochberg approach (desired FDR = 0.05). All data are represented with mean ± SEM. Statistical significances are denoted by * $p\leq0.05$, ** $p\leq0.01$, *** $p\leq0.001$, **** $p\leq0.0001$. See also Tables 3.3 and 3.4.

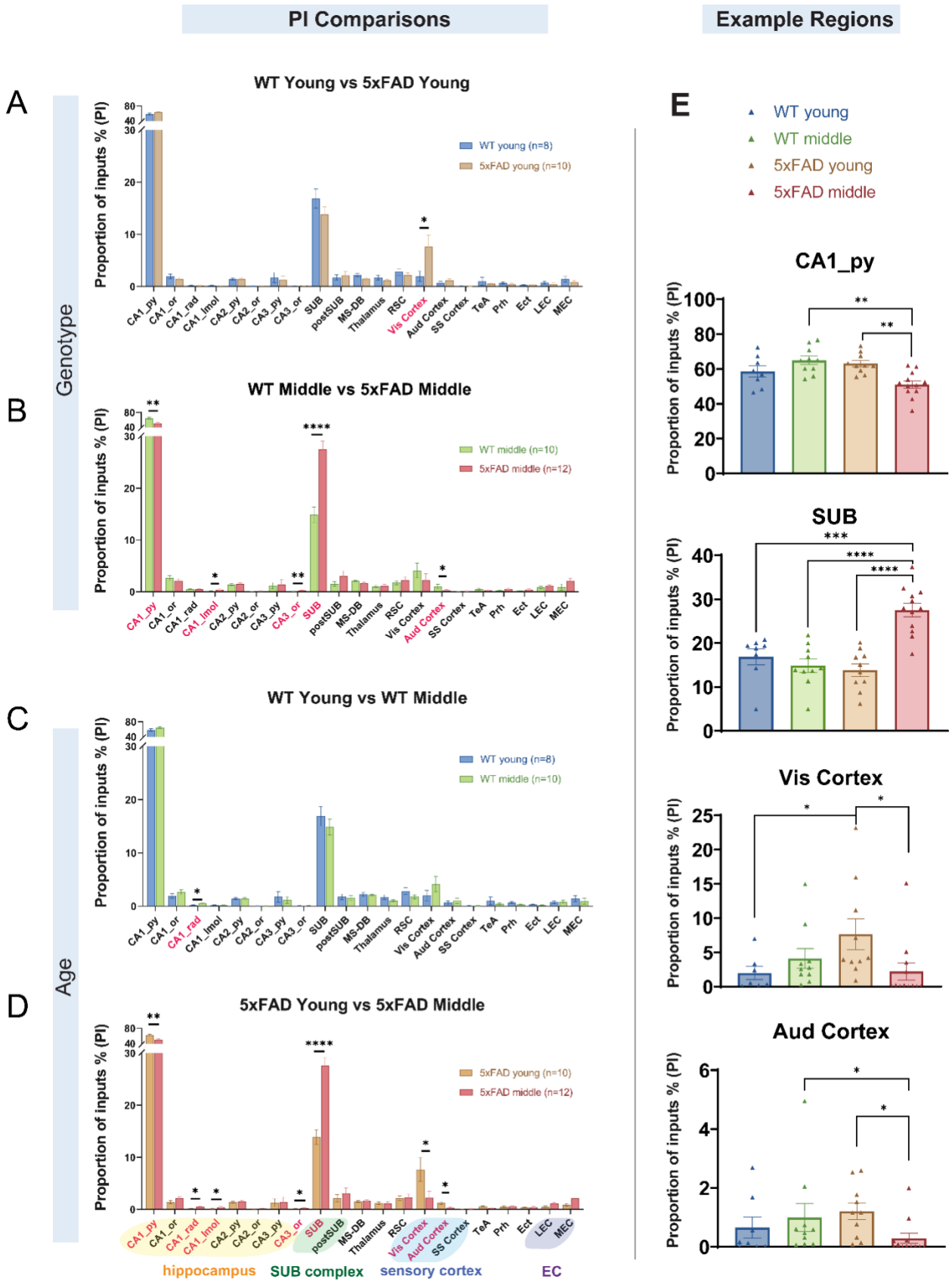
PI Comparisons
Example Regions
A
B
C
D
Genotype
Age
WT Young vs 5xFAD Young
WT Middle vs 5xFAD Middle
WT Young vs WT Middle
5xFAD Young vs 5xFAD Middle
Proportion of inputs % (PI)
WT young (n=8)
5xFAD young (n=10)
WT middle (n=10)
5xFAD middle (n=12)
CA1_py
CA1_or
CA1_rad
CA1_lmol
CA2_py
CA2_or
CA3_py
CA3_or
SUB
postSUB
MS-DB
Thalamus
RSC
Vis Cortex
Aud Cortex
SS Cortex
TeA
Prh
Ect
LEC
MEC
hippocampus
SUB complex
sensory cortex
EC
E
WT young
WT middle
5xFAD young
5xFAD middle
CA1_py
SUB
Vis Cortex
Aud Cortex

Figure 3.9 Quantification of the proportion of inputs to SUB excitatory neurons
Quantitative analysis of the proportion of inputs (PI) values across four groups of mice. The PI is the ratio of the input neuron number in a subregion to the total input neuron number in a brain. The input regions include hippocampal CA1, CA2, and CA3 sublayers, as well as the SUB, postSUB, thalamus, RSC, Vis cortex, Aud cortex, SS cortex, TeA, Prh, Ect, LEC, and MEC. The regions showing statistical differences are shown in red text. ***A***, 5xFAD young mice show significantly higher PI values than WT young mice in the Vis cortex ($p = 1.93\times10^{-2}$). ***B***, WT middle-age mice show significantly higher PI values than 5xFAD middle-age mice in CA1_py, and Aud cortex ($p = 1.2\times10^{-3}$, $p = 2.66\times10^{-2}$, respectively). WT middle-age mice show significantly lower PI values than 5xFAD middle-age mice in CA1_lmol, CA3_or and SUB ($p = 2.75\times10^{-2}$, $p = 6.01\times10^{-3}$, $p = 7\times10^{-5}$, respectively). ***C***, WT young mice show significantly lower PI values than WT middle-age mice in CA1_rad ($p = 1.79\times10^{-2}$). ***D***, 5xFAD young mice show significantly higher PI values than 5xFAD middle-age mice in CA1_py, Vis cortex, and Aud cortex ($p = 1.2\times10^{-3}$, $p = 1.37\times10^{-2}$, $p = 1.32\times10^{-2}$, respectively). 5xFAD young mice show significantly lower PI values than 5xFAD middle-age mice in CA1_rad, CA1_lmol, CA3_or and SUB ($p = 1.79\times10^{-2}$, $p = 1.76\times10^{-2}$, $p = 1.79\times10^{-2}$, $p = 5.0\times10^{-5}$, respectively). ***E***, PI comparisons of example regions across four groups of mice. Representative regions include CA1_py, SUB, Vis Cortex and Aud Cortex. The mouse numbers for each group are WT young n = 8, WT middle-age n = 10, 5xFAD young n = 10, and 5xFAD middle-age n = 12. The statistical test is the Wilcoxon rank-sum test. The p values are adjusted with False Discovery Rate (FDR) Benjamini-Hochberg approach (desired FDR = 0.05). All data are represented with mean ± SEM. Statistical significances are denoted by * $p \leq 0.05$, ** $p \leq 0.01$, *** $p \leq 0.001$, **** $p \leq 0.0001$. See also Tables 3.3 and 3.4.

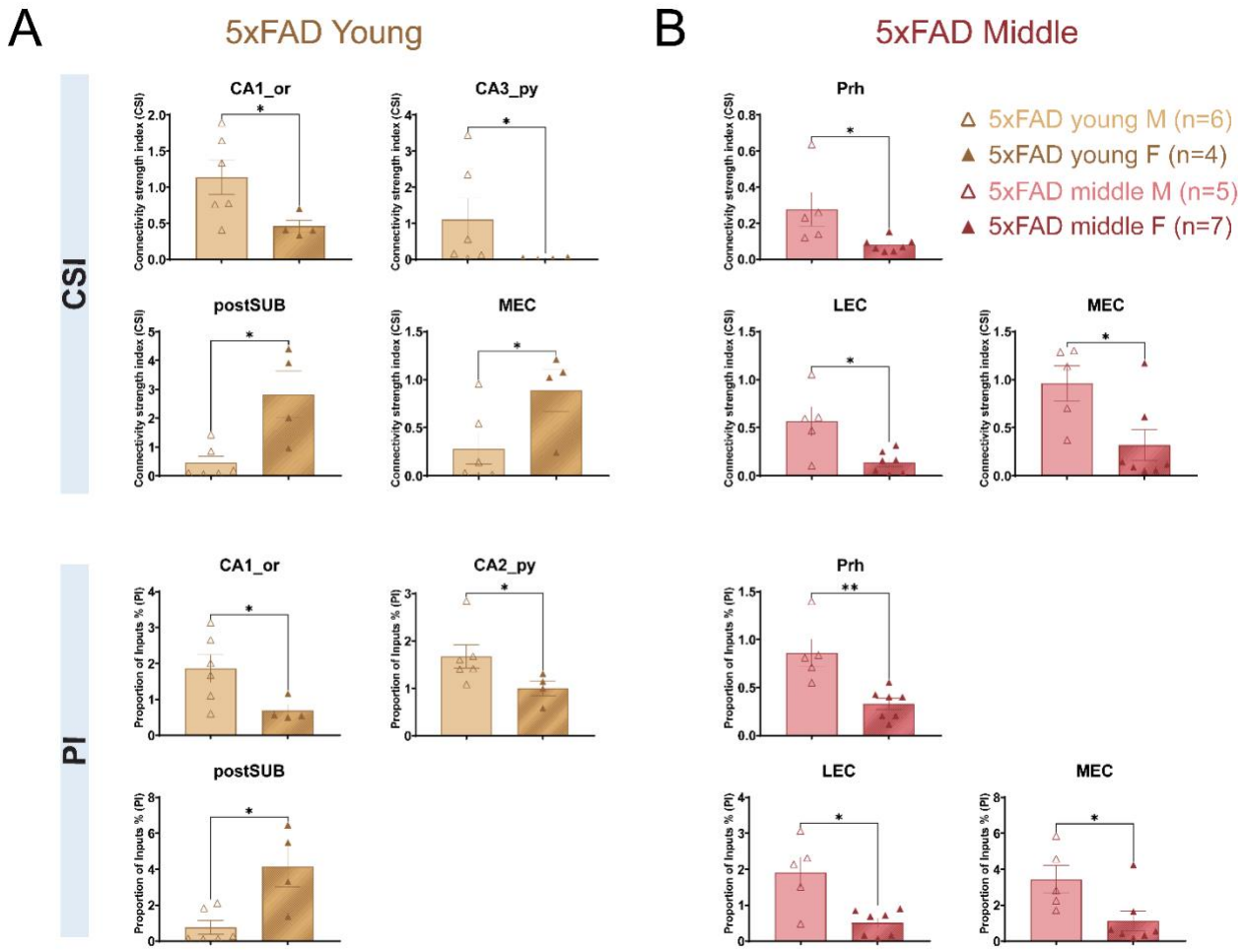

Figure 3.10 Sex differences of CSI and PI measurements in 5xFAD young and middle-age mice

Sex-specific comparisons of CSI and PI values for 5xFAD young and middle-age mice. ***A***, Sex differences of 5xFAD young group. The CSI differences are observed for CA1_or, CA3_py, postSUB, MEC (Wilcoxon rank-sum test, $p = 1.9\times10^{-2}$, $p = 3.81\times10^{-2}$, $p = 1.9\times10^{-2}$, $p = 3.81\times10^{-2}$, respectively). The PI differences are observed for CA1_or, CA2_py, and postSUB (Wilcoxon rank-sum test, $p = 3.81\times10^{-2}$, $p = 3.81\times10^{-2}$, $p = 3.81\times10^{-2}$, respectively). ***B***, Sex differences of 5xFAD middle-age group. The CSI differences are observed for Prh, LEC, and MEC (Wilcoxon rank-sum test, $p = 1.01\times10^{-2}$, $p = 3.03\times10^{-2}$, $p = 3.03\times10^{-2}$, respectively). The PI differences are observed in Prh, LEC, and MEC (Wilcoxon rank-sum test, $p = 5.1\times10^{-3}$, $p = 3.03\times10^{-2}$, $p = 1.77\times10^{-2}$, respectively). The mouse numbers for each group are 5xFAD young (male n = 4, female n = 6), and 5xFAD middle-age (male n = 5, female n = 7). The statistical test is the Wilcoxon rank-sum test. All data are represented with mean ± SEM. Statistical significances are denoted by * $p \leq 0.05$, ** $p \leq 0.01$, *** $p \leq 0.001$, **** $p \leq 0.0001$.

Table 3.1 Summary of quantification for 6E10 amyloid-beta immunostaining

Summary	WT young		WT middle		5xFAD young		5xFAD middle	
# of mice	8-10 for each group							
	Mean	SEM	Mean	SEM	Mean	SEM	Mean	SEM
Density (mm^{-2})	0	0	0	0	2151	±214.3	2698	±141.8
Size (μm^2)	0	0	0	0	73.59	±1.645	139.9	±2.247
Intensity (AU)	0	0	0	0	3018	±33.42	3761	±30.54
Intracellular Density (mm^{-2})	0	0	0	0	7188	±548.1	3554	±396.7
Statistical Comparison								
Comparison	5xFAD young vs 5xFAD middle							
	p value				significance			
Density (mm^{-2})	6.7600E-02				ns			
Size (μm^2)	1.8648E-12				****			
Intensity (AU)	9.1253E-07				****			
Intracellular Density (mm^{-2})	7.5776E-05				****			

Statistical method: Wilcoxon rank sum test and linear mixed effects model.
* p<0.05, ** p<0.01, *** p<0.001, **** p<0.0001

The 6E10 amyloid staining quantification results and statistical comparisons summary for WT young, WT middle-age, 5xFAD young, and 5xFAD middle-age mice (n = 8-10 for each group). Statistical significances are denoted by * $p \leq 0.05$, ** $p \leq 0.01$, *** $p \leq 0.001$, **** $p \leq 0.0001$.

Table 3.2 Summary of quantification for sex-specific 6E10 amyloid-beta (Aβ) immunostaining

Summary	WT Young Male		WT Young Female		WT Middle Male		WT Middle Female		5xFAD Young Male		5xFAD Young Female		5xFAD Middle Male		5xFAD Middle Female	
# of mice	4-5 for each group															
	Mean	SEM	Mean	SEM	Mean	SEM	Mean	SEM	Mean	SEM	Mean	SEM	Mean	SEM	Mean	SEM
Density (mm^{-2})	0	0	0	0	0	0	0	0	1601	94.8	2702	214.6	2432	157.5	2963	148.6
Size (μm^2)	0	0	0	0	0	0	0	0	68.7	2.7	74.3	2.0	130	2.9	150	3.4
Intensity (AU)	0	0	0	0	0	0	0	0	1985	36.0	3473	37.1	3718	37.7	3805	48.5
Intracellular Density (mm^{-2})	0	0	0	0	0	0	0	0	8479	293.9	5896	656.4	4603	323.5	2506	232.0

Statistical Comparison

Comparison	5xFAD Young Male vs 5xFAD Young Female		5xFAD Middle Male vs 5xFAD Middle Female		5xFAD Young Male vs 5xFAD Middle Male		5xFAD Young Female vs 5xFAD Middle Female	
	p value	significance	p value	significance	p value	significance	p value	significance
Density (mm^{-2})	7.9000E-03	**	5.7100E-02	ns	1.5900E-02	*	4.1270E-01	ns
Size (μm^2)	7.7752E-01	ns	2.0914E-01	ns	2.6272E-11	****	5.8125E-06	****
Intensity (AU)	6.7646E-16	****	3.4272E-01	ns	1.3916E-23	****	1.1840E-02	*
Intracellular Density (mm^{-2})	3.1700E-02	*	7.9000E-03	**	7.9000E-03	**	7.9000E-03	**

Statistical method: Wilcoxon rank sum test and linear mixed effects model

* p<0.05, ** p<0.01, *** p<0.001, **** p<0.0001

The 6E10 amyloid staining quantification results and statistical comparisons summary for both sexes of WT young, WT middle-age, 5xFAD young, and 5xFAD middle-age mice (n = 4-5 for each subgroup). Statistical significances are denoted by * $p \leq 0.05$, ** $p \leq 0.01$, *** $p \leq 0.001$, **** $p \leq 0.0001$.

Table 3.3 Data summary of CSI and PI measurements

CSI Summary	WT Young		WT Middle		5xFAD Young		5xFAD Middle	
	Mean	SEM	Mean	SEM	Mean	SEM	Mean	SEM
CA1_py	37.7953	5.2921	31.5000	4.3837	40.7620	2.3022	13.8835	1.3216
CA1_or	1.2013	0.3422	1.2242	0.2206	0.8664	0.1782	0.5687	0.1026
CA1_rad	0.1160	0.0193	0.2302	0.0286	0.0985	0.0314	0.1216	0.0318
CA1_lmol	0.1093	0.0401	0.0628	0.0147	0.0632	0.0247	0.1024	0.0263
CA2_py	0.8291	0.0965	0.7376	0.2225	0.8725	0.0868	0.4024	0.0506
CA2_or	0.0296	0.0093	0.0234	0.0072	0.0583	0.0127	0.0438	0.0130
CA3_py	1.0087	0.5901	0.3927	0.1854	0.6763	0.3820	0.3453	0.2308
CA3_or	0.0475	0.0128	0.0413	0.0074	0.0748	0.0133	0.0686	0.0112
SUB	10.1783	1.2574	6.5282	0.5425	8.8363	0.9168	7.4721	0.7437
postSUB	0.9515	0.2478	0.9427	0.4536	1.4021	0.5041	0.9485	0.3778
MS-DB	1.3175	0.1816	1.0204	0.1924	0.9410	0.1071	0.4593	0.0628
Thalamus	0.9022	0.2451	0.4653	0.0931	0.7509	0.1263	0.3354	0.1102
RSC	1.7979	0.4588	0.9879	0.3911	1.4492	0.3497	0.6619	0.2547
Vis Cortex	1.2750	0.7136	2.8280	1.5745	5.2217	1.6207	0.5301	0.2877
Aud Cortex	0.6859	0.4599	0.7486	0.5241	0.8048	0.2012	0.0672	0.0390
SS Cortex	0.0676	0.0329	0.0575	0.0416	0.0221	0.0078	0.0224	0.0123
TeA	1.1864	1.0377	0.3050	0.1541	0.3566	0.0686	0.0888	0.0291
Prh	0.4073	0.1505	0.1088	0.0256	0.2884	0.0872	0.1620	0.0475
Ect	0.2519	0.0940	0.0863	0.0268	0.2362	0.0678	0.1280	0.0474
LEC	0.4429	0.1457	0.3485	0.0905	0.2719	0.1078	0.3179	0.0902
MEC	0.7852	0.2759	0.4092	0.2281	0.5234	0.1567	0.5871	0.1493
PI Summary	WT Young		WT Middle		5xFAD Young		5xFAD Middle	
	Mean	SEM	Mean	SEM	Mean	SEM	Mean	SEM
CA1_py	58.4838	3.1812	64.8701	2.4048	63.0325	1.8142	51.0676	2.1452
CA1_or	1.9183	0.4506	2.6308	0.4665	1.3955	0.2988	2.0883	0.3278
CA1_rad	0.2115	0.0556	0.5114	0.0625	0.1582	0.0507	0.4526	0.0978
CA1_lmol	0.1877	0.0578	0.1572	0.0393	0.1127	0.0514	0.4002	0.1152
CA2_py	1.4048	0.1801	1.4068	0.2230	1.4031	0.1889	1.5151	0.2089
CA2_or	0.0518	0.0136	0.0575	0.0171	0.0980	0.0227	0.1640	0.0518
CA3_py	1.7384	0.9727	1.1501	0.6257	1.2584	0.7657	1.3853	1.0092
CA3_or	0.0716	0.0149	0.0992	0.0186	0.1258	0.0258	0.2486	0.0324
SUB	16.8789	1.8477	14.8686	1.5137	13.8588	1.4307	27.5509	1.5691
postSUB	1.7476	0.5280	1.5225	0.4565	2.1249	0.7269	3.0727	1.0010
MS-DB	2.2173	0.3269	2.1018	0.1580	1.4978	0.1909	1.6799	0.1509
Thalamus	1.7093	0.4501	1.0427	0.2103	1.1849	0.2234	1.1212	0.2969
RSC	2.8141	0.6319	1.7410	0.3970	2.1658	0.4382	2.2247	0.6888
Vis Cortex	1.9859	0.9604	4.1163	1.4331	7.6444	2.2371	2.2177	1.2674
Aud Cortex	0.6553	0.3533	0.9941	0.4759	1.2035	0.2885	0.2911	0.1738
SS Cortex	0.0920	0.0435	0.0767	0.0383	0.0343	0.0122	0.0864	0.0531
TeA	0.9889	0.7338	0.4625	0.1840	0.5486	0.1165	0.2889	0.0871
Prh	0.6574	0.2115	0.2642	0.0875	0.4744	0.1725	0.5506	0.1024
Ect	0.3258	0.0775	0.1735	0.0408	0.3472	0.0884	0.4090	0.1204
LEC	0.7472	0.2130	0.8340	0.2597	0.4807	0.2291	1.0881	0.2779
MEC	1.4215	0.5267	0.9189	0.5871	0.8505	0.2668	2.0971	0.5510
# of mice	8		10		10		12	
# of starters	95	20	101	17	65	15	132	17
# of total labeled neurons	5357	729	4218	546	4064	699	3739	509
Overall connectivity	69	11	51	8	67	3	29	2

The data summary of CSI and PI values for WT young, WT middle-age, 5xFAD young, and 5xFAD middle-age mice. Data are presented as mean ± SEM.

Table 3.4 Statistical comparisons of CSI and PI values

	Genotype Comparison				Age Comparison			
CSI Comparison	WT Young vs 5xFAD Young		WT Middle vs 5xFAD Middle		WT Young vs WT Middle		5xFAD Young vs 5xFAD Middle	
	p value	significance	p value	significance	p value	significance	p value	significance
CA1_py	0.35993		0.00012	***	0.31598		0.00001	****
CA1_or	0.36571		0.04461	*	0.57260		0.36571	
CA1_rad	0.40825		0.00878	**	0.00878	**	0.40825	
CA1_lmol	0.31424		0.31424		0.35993		0.31424	
CA2_py	0.76183		0.27076		0.27076		0.00056	***
CA2_or	0.45408		0.45408		0.57169		0.55594	
CA3_py	>0.999999		>0.999999		>0.999999		>0.999999	
CA3_or	0.44303		0.44303		0.96545		0.94545	
SUB	0.51479		0.46171		0.04662	*	0.46171	
postSUB	>0.999999		>0.999999		>0.999999		>0.999999	
MS-DB	0.12199		0.00333	**	0.02736	*	0.00403	**
Thalamus	0.82856		0.24026		0.24026		0.06760	
RSC	0.57260		0.57260		0.16628		0.04461	*
Vis Cortex	0.01289	*	0.01289	*	0.60088		0.00120	**
Aud Cortex	0.18736		0.01379	*	0.39469		0.00081	***
SS Cortex	0.66868		0.66868		0.66868		0.66868	
TeA	0.34562		0.45001		0.45976		0.00645	**
Prh	0.54433		0.58241		0.16084		0.16084	
Ect	0.69647		0.69647		0.17368		0.21440	
LEC	0.66668		0.71821		0.76183		0.71821	
MEC	0.58990		0.54856		0.54856		0.58990	
PI Comparison	WT Young vs 5xFAD Young		WT Middle vs 5xFAD Middle		WT Young vs WT Middle		5xFAD Young vs 5xFAD Middle	
	p value	significance	p value	significance	p value	significance	p value	significance
CA1_py	0.27428		0.00120	**	0.19428		0.00120	**
CA1_or	0.36571		0.45615		0.36571		0.36571	
CA1_rad	0.35993		0.35993		0.01791	*	0.01791	*
CA1_lmol	0.31424		0.02754	*	0.89675		0.01760	*
CA2_py	>0.999999		>0.999999		>0.999999		>0.999999	
CA2_or	0.34334		0.09909		0.96545		0.83628	
CA3_py	>0.999999		0.96312		0.96312		0.96312	
CA3_or	0.21034		0.00601	**	0.21034		0.01791	*
SUB	0.13480		0.00007	****	0.23699		0.00005	****
postSUB	0.82856		0.76347		0.76347		0.76347	
MS-DB	0.24582		0.24582		0.89675		0.60820	
Thalamus	0.71821		0.92287		0.71821		0.71821	
RSC	0.71986		0.82120		0.69126		0.82120	
Vis Cortex	0.01934	*	0.05676		0.19323		0.01374	*
Aud Cortex	0.18736		0.02664	*	0.30449		0.01324	*
SS Cortex	0.86935		0.86935		0.86935		0.86935	
TeA	0.40614		0.54325		>0.999999		0.26917	
Prh	0.69647		0.05508		0.24398		0.37725	
Ect	>0.999999		0.58069		0.48796		>0.999999	
LEC	0.39160		0.66201		>0.999999		0.11689	
MEC	0.47463		0.06760		0.31598		0.16084	

Statistical method: Wilcoxon rank sum test.
P values adjusted with False Discovery Rate (FDR) Benjamini-Hochberg approach (desired FDR = 0.05)
* p<0.05, ** p<0.01, *** p<0.001, **** p<0.0001

The data summary of CSI and PI value group-wise comparisons. The comparisons include WT young vs. 5xFAD young, WT middle-age vs. 5xFAD middle-age, WT young vs. WT middle-age, and 5xFAD young vs. 5xFAD middle-age group. Statistical significances are denoted by * $p \leq 0.05$, ** $p \leq 0.01$, *** $p \leq 0.001$, **** $p \leq 0.0001$.

Table 3.5 Data summary of sex-specific CSI and PI measurements

CSI summary	WT young male		WT young female		WT middle male		WT middle female		5xFAD young male		5xFAD young female		5xFAD middle male		5xFAD middle female	
	Mean	SEM	Mean	SEM	Mean	SEM	Mean	SEM	Mean	SEM	Mean	SEM	Mean	SEM	Mean	SEM
CA1_py	42.9091	12.2310	34.7270	5.2214	29.0351	5.1714	33.9649	7.5297	40.2835	3.2403	41.4797	3.6353	15.2042	2.3854	12.9402	1.5570
CA1_or	1.7879	0.8642	0.8493	0.1457	1.0370	0.2123	1.4113	0.3954	1.1376	0.2363	0.4597	0.0822	0.5438	0.1110	0.5866	0.1645
CA1_rad	0.1510	0.0211	0.0950	0.0247	0.2026	0.0374	0.2579	0.0434	0.1342	0.0473	0.0449	0.0150	0.0852	0.0161	0.1477	0.0528
CA1_lmol	0.1911	0.0949	0.0603	0.0142	0.0745	0.0211	0.0510	0.0215	0.0657	0.0411	0.0595	0.0188	0.0877	0.0203	0.1128	0.0440
CA2_py	0.9353	0.1983	0.7653	0.1075	0.7019	0.1284	0.7734	0.4535	1.0114	0.1015	0.6642	0.0812	0.3530	0.0887	0.4377	0.0617
CA2_or	0.0181	0.0090	0.0366	0.0136	0.0384	0.0102	0.0084	0.0045	0.0559	0.0182	0.0618	0.0195	0.0421	0.0202	0.0450	0.0183
CA3_py	2.4608	1.2414	0.1374	0.0819	0.3693	0.1916	0.4161	0.3432	1.1074	0.5873	0.0296	0.0124	0.1569	0.0470	0.4800	0.3989
CA3_or	0.0738	0.0251	0.0317	0.0102	0.0577	0.0027	0.0250	0.0104	0.0848	0.0141	0.0599	0.0265	0.0632	0.0190	0.0724	0.0147
SUB	10.6596	2.6834	9.8896	1.4870	7.7774	0.4238	5.2789	0.6037	7.6731	1.2193	10.5810	0.9464	8.2400	1.3706	6.9236	0.8505
postSUB	0.4306	0.0779	1.2640	0.3240	0.4970	0.2371	1.3884	0.8776	0.4543	0.2307	2.8238	0.8060	0.8778	0.1983	0.9990	0.6549
MS-DB	1.8243	0.3018	1.0134	0.0583	0.9049	0.0536	1.1360	0.3963	0.9502	0.1318	0.9271	0.2060	0.4702	0.0992	0.4516	0.0877
Thalamus	0.4501	0.1973	1.1735	0.3278	0.5409	0.1744	0.3896	0.0758	0.5719	0.1623	1.0193	0.1178	0.3824	0.0413	0.3018	0.1921
RSC	1.7087	0.9882	1.8514	0.5427	0.7237	0.2652	1.2522	0.7637	0.9900	0.2688	2.1380	0.6878	0.6291	0.0445	0.6853	0.4503
Vis Cortex	2.6864	2.6407	0.7104	0.3050	0.7550	0.2404	4.9011	2.9914	5.5455	2.4395	4.7361	2.1658	0.0374	0.0136	0.8820	0.4588
Aud Cortex	1.6675	1.0918	0.0970	0.0580	0.1509	0.0642	1.3464	1.0264	0.7917	0.2753	0.8244	0.3376	0.0025	0.0016	0.1134	0.0626
SS Cortex	0.1274	0.0787	0.0318	0.0178	0.0186	0.0080	0.0964	0.0835	0.0219	0.0123	0.0223	0.0085	0.0035	0.0015	0.0360	0.0200
TeA	2.8949	2.7756	0.1613	0.0565	0.0787	0.0336	0.5314	0.2831	0.3616	0.1036	0.3490	0.0919	0.0860	0.0532	0.0908	0.0362
Prh	0.7119	0.3397	0.2246	0.0810	0.1132	0.0169	0.1044	0.0515	0.2847	0.1224	0.2939	0.1397	0.2772	0.0937	0.0797	0.0145
Ect	0.4496	0.2008	0.1333	0.0572	0.0792	0.0275	0.0934	0.0496	0.2207	0.0981	0.2595	0.1004	0.2067	0.1016	0.0718	0.0295
LEC	0.6528	0.3537	0.3170	0.1063	0.4933	0.1562	0.2037	0.0447	0.2568	0.1801	0.2946	0.0762	0.5671	0.1518	0.1399	0.0435
MEC	0.5968	0.2774	0.8982	0.4260	0.6872	0.4344	0.1312	0.0821	0.2812	0.1586	0.8867	0.2191	0.9609	0.1825	0.3201	0.1603
PI summary	WT young male		WT young female		WT middle male		WT middle female		5xFAD young male		5xFAD young female		5xFAD middle male		5xFAD middle female	
	Mean	SEM	Mean	SEM	Mean	SEM	Mean	SEM	Mean	SEM	Mean	SEM	Mean	SEM	Mean	SEM
CA1_py	50.5757	3.2526	63.2287	3.1864	64.0740	3.4701	65.6662	3.6968	64.5390	2.7946	60.7729	1.5243	52.1118	2.6882	50.3218	3.2863
CA1_or	2.3875	1.1582	1.6367	0.3367	2.4741	0.6328	2.7875	0.7527	1.8629	0.3860	0.6946	0.1556	1.8186	0.2451	2.2809	0.5424
CA1_rad	0.2274	0.0908	0.2019	0.0783	0.4928	0.1191	0.5299	0.0565	0.2186	0.0754	0.0676	0.0226	0.3011	0.0575	0.5608	0.1543
CA1_lmol	0.2800	0.1309	0.1323	0.0466	0.1662	0.0338	0.1482	0.0760	0.1252	0.0860	0.0938	0.0330	0.2983	0.0621	0.4730	0.1943
CA2_py	1.4045	0.5303	1.4050	0.0804	1.5931	0.2552	1.2204	0.3758	1.6700	0.2483	1.0028	0.1566	1.1511	0.1526	1.7750	0.3148
CA2_or	0.0310	0.0165	0.0643	0.0183	0.0919	0.0244	0.0231	0.0113	0.0982	0.0328	0.0976	0.0345	0.1229	0.0385	0.1934	0.0859
CA3_py	4.0921	2.0561	0.3262	0.2263	0.9925	0.5877	1.3077	1.1849	2.0701	1.1955	0.0407	0.0156	0.4929	0.0803	2.0228	1.7423
CA3_or	0.0823	0.0157	0.0652	0.0228	0.1360	0.0123	0.0625	0.0269	0.1454	0.0319	0.0963	0.0441	0.1974	0.0311	0.2853	0.0480
SUB	15.2455	5.1588	17.8589	0.9671	18.1437	1.3884	11.5936	1.7380	12.4974	1.8416	15.9009	2.1347	27.9713	1.6107	27.2506	2.5429
postSUB	0.5361	0.0678	2.4744	0.6535	1.1785	0.6207	1.8664	0.7025	0.7697	0.3836	4.1576	1.1400	3.0415	0.5101	3.0950	1.7393
MS-DB	2.5588	0.7617	2.0124	0.3117	2.1252	0.2090	2.0784	0.2616	1.5778	0.2631	1.3778	0.3040	1.5772	0.0958	1.7532	0.2551
Thalamus	0.7584	0.3889	2.2798	0.5522	1.2775	0.3898	0.8079	0.1395	0.9689	0.3375	1.5089	0.1772	1.3694	0.1612	0.9439	0.5020
RSC	1.6603	0.4979	3.5065	0.8510	1.7324	0.6405	1.7496	0.5468	1.5832	0.3905	3.0396	0.7965	2.3727	0.4423	2.1190	1.1805
Vis Cortex	3.5469	9.5324	1.3614	0.6376	1.6289	0.4941	6.6038	2.4299	8.1577	3.3488	6.8743	3.0282	0.1208	0.0333	3.7154	2.0374
Aud Cortex	1.4570	0.7845	0.1743	0.1026	0.3035	0.1028	1.6846	0.8777	1.2092	0.3982	1.1950	0.4772	0.0066	0.0040	0.4943	0.2800
SS Cortex	0.1454	0.1078	0.0599	0.0334	0.0426	0.0202	0.1109	0.0749	0.0354	0.0195	0.0325	0.0129	0.0109	0.0046	0.1403	0.0878
TeA	2.1409	1.9823	0.2976	0.1020	0.1580	0.0598	0.7670	0.3200	0.5785	0.1838	0.5038	0.1275	0.2467	0.1613	0.3191	0.1053
Prh	1.0440	0.4758	0.4255	0.1465	0.2664	0.0435	0.2620	0.1804	0.5215	0.2787	0.4038	0.1621	0.8612	0.1434	0.3288	0.0591
Ect	0.4609	0.1409	0.2447	0.0804	0.1975	0.0720	0.1494	0.0450	0.3386	0.1355	0.3601	0.1123	0.5803	0.2180	0.2866	0.1301
LEC	0.9827	0.4826	0.6059	0.2094	1.2550	0.4542	0.4130	0.0931	0.5077	0.3894	0.4404	0.1166	1.9025	0.4318	0.5063	0.1363
MEC	1.0603	0.6549	1.6383	0.7854	1.6699	1.1236	0.1678	0.0815	0.5249	0.3304	1.3390	0.3586	3.4448	0.7696	1.1345	0.5491
# of mice	3		5		5		5		6		4		5		7	
# of starters	93	40	96	25	120	22	83	26	73	26	54	4	183	15	95	14
# of total labeled neurons	6173	1835	4867	564	5101	612	3336	759	4261	1187	3771	299	5366	411	2577	438
Overall connectivity	90	27	57	7	46	5	55	15	64	4	70	5	31	5	27	3

The data summary for sex-specific CSI and PI values of WT young, WT middle-age, 5xFAD young, and 5xFAD middle-age mice. Data are presented as mean ± SEM.

Table 3.6 Statistical comparisons of CSI and PI values between sexes

CSI comparison	WT young male vs WT young female		WT middle male vs WT middle female		5xFAD young male vs 5xFAD young female		5xFAD middle male vs 5xFAD middle female	
	p value	significance	p value	significance	p value	significance	p value	significance
CA1_py	0.7857		0.8413		>0.9999		0.4318	
CA1_or	0.3929		0.5476		0.0190	*	0.8763	
CA1_rad	0.2500		0.8413		0.2571		0.6755	
CA1_lmol	0.2500		0.3095		0.6095		0.8763	
CA2_py	0.2500		0.3095		0.0667		0.2677	
CA2_or	0.7857		0.0317	*	0.7095		0.6389	
CA3_py	0.1250		>0.9999		0.0381	*	0.4318	
CA3_or	0.2500		0.0079	**	0.5714		0.6389	
SUB	>0.9999		0.0317	*	0.1143		0.5030	
postSUB	0.0714		0.4206		0.0190	*	0.2020	
MS-DB	0.0357	*	0.3095		0.9143		0.8763	
Thalamus	0.1429		>0.9999		0.1143		0.0732	
RSC	0.5714		0.6905		0.1143		0.1490	
Vis Cortex	>0.9999		0.2222		0.7619		0.4318	
Aud Cortex	0.4464		0.0952		0.9413		0.0922	
SS Cortex	0.3750		>0.9999		0.8000		0.1263	
TeA	>0.9999		0.4206		0.9143		0.6755	
Prh	0.2500		0.4206		0.7619		0.0101	*
Ect	0.2500		>0.9999		0.7619		0.2020	
LEC	0.5714		0.2222		0.3238		0.0303	*
MEC	>0.9999		0.2222		0.0381	*	0.0303	*

PI comparison	WT young male vs WT young female		WT middle male vs WT middle female		5xFAD young male vs 5xFAD young female		5xFAD middle male vs 5xFAD middle female	
	p value	significance	p value	significance	p value	significance	p value	significance
CA1_py	0.0714		>0.9999		0.4762		0.8763	
CA1_or	>0.9999		0.8413		0.0381	*	0.8763	
CA1_rad	0.7857		0.6905		0.2571		0.4318	
CA1_lmol	0.3929		0.4206		0.6095		0.7551	
CA2_py	0.5714		0.5476		0.0381	*	0.2020	
CA2_or	0.3929		0.0556		>0.9999		0.6389	
CA3_py	0.2321		>0.9999		0.0667		0.3434	
CA3_or	>0.9999		0.0317	*	0.3524		0.3434	
SUB	0.5714		0.0317	*	0.2571		>0.9999	
postSUB	0.0357	*	0.4206		0.0381	*	0.2677	
MS-DB	0.5714		>0.9999		>0.9999		0.4318	
Thalamus	0.1429		0.6905		0.2571		0.1490	
RSC	0.3929		0.5476		0.1143		0.2677	
Vis Cortex	>0.9999		0.0556		>0.9999		0.4318	
Aud Cortex	0.4464		0.0952		>0.9999		0.0922	
SS Cortex	0.7857		>0.9999		0.8000		0.1263	
TeA	>0.9999		0.2222		0.9143		0.6755	
Prh	0.3929		0.1508		0.9143		0.0051	**
Ect	0.2500		0.6905		0.7619		0.3434	
LEC	0.5714		0.1508		0.2381		0.0303	*
MEC	>0.9999		0.2222		0.1714		0.0177	*

Statistical method: Wilcoxon rank sum test.
* p<0.05, ** p<0.01, *** p<0.001, **** p<0.0001

The data summary of CSI and PI values comparisons between sexes for WT young, middle-age, 5xFAD young, and 5xFAD middle-age mice. Statistical significances are denoted by * $p \leq 0.05$, ** $p \leq 0.01$, *** $p \leq 0.001$, **** $p \leq 0.0001$.

References

Barnes, L.L., Wilson, R.S., Bienias, J.L., Schneider, J.A., Evans, D.A., and Bennett, D.A. (2005). Sex differences in the clinical manifestations of Alzheimer disease pathology. Arch Gen Psychiatry *62*, 685-691.

Beier, K.T., Kim, C.K., Hoerbelt, P., Hung, L.W., Heifets, B.D., DeLoach, K.E., Mosca, T.J., Neuner, S., Deisseroth, K., Luo, L.*, et al.* (2017). Rabies screen reveals GPe control of cocaine-triggered plasticity. Nature *549*, 345-350.

Bohm, C., Peng, Y., Maier, N., Winterer, J., Poulet, J.F., Geiger, J.R., and Schmitz, D. (2015). Functional Diversity of Subicular Principal Cells during Hippocampal Ripples. The Journal of neuroscience : the official journal of the Society for Neuroscience *35*, 13608-13618.

Busche, M.A., Grienberger, C., Keskin, A.D., Song, B., Neumann, U., Staufenbiel, M., Forstl, H., and Konnerth, A. (2015). Decreased amyloid-beta and increased neuronal hyperactivity by immunotherapy in Alzheimer's models. Nat Neurosci *18*, 1725-1727.

Calvo, N., and Einstein, G. (2023). Steroid hormones: risk and resilience in women's Alzheimer disease. Front Aging Neurosci *15*, 1159435.

Carlesimo, G.A., Piras, F., Orfei, M.D., Iorio, M., Caltagirone, C., and Spalletta, G. (2015). Atrophy of presubiculum and subiculum is the earliest hippocampal anatomical marker of Alzheimer's disease. Alzheimers Dement (Amst) *1*, 24-32.

Eimer, W.A., and Vassar, R. (2013). Neuron loss in the 5XFAD mouse model of Alzheimer's disease correlates with intraneuronal Abeta42 accumulation and Caspase-3 activation. Mol Neurodegener *8*, 2.

Good, P.F., Alapat, D., Hsu, A., Chu, C., Perl, D., Wen, X., Burstein, D.E., and Kohtz, D.S. (2004). A role for semaphorin 3A signaling in the degeneration of hippocampal neurons during Alzheimer's disease. Journal of neurochemistry *91*, 716-736.

Harris, E., Witter, M.P., Weinstein, G., and Stewart, M. (2001). Intrinsic connectivity of the rat subiculum: I. Dendritic morphology and patterns of axonal arborization by pyramidal neurons. The Journal of comparative neurology *435*, 490-505.

Harris, S.S., Wolf, F., De Strooper, B., and Busche, M.A. (2020). Tipping the Scales: Peptide-Dependent Dysregulation of Neural Circuit Dynamics in Alzheimer's Disease. Neuron *107*, 417-435.

Iaccarino, H.F., Singer, A.C., Martorell, A.J., Rudenko, A., Gao, F., Gillingham, T.Z., Mathys, H., Seo, J., Kritskiy, O., Abdurrob, F.*, et al.* (2016). Gamma frequency entrainment attenuates amyloid load and modifies microglia. Nature *540*, 230-235.

Jawhar, S., Trawicka, A., Jenneckens, C., Bayer, T.A., and Wirths, O. (2012). Motor deficits, neuron loss, and reduced anxiety coinciding with axonal degeneration and intraneuronal Abeta aggregation in the 5XFAD mouse model of Alzheimer's disease. Neurobiol Aging *33*, 196 e129-140.

Jeon, S.G., Kim, Y.J., Kim, K.A., Mook-Jung, I., and Moon, M. (2018). Visualization of Altered Hippocampal Connectivity in an Animal Model of Alzheimer's Disease. Mol Neurobiol *55*, 7886-7899.

Kim, K., Miller, D., Sapienza, V., Chen, C.-M.J., Bai, C., Grundke-Iqbal, I., Currie, J., and Wisniewski, H. (1988). Production and characterization of monoclonal antibodies reactive to synthetic cerebrovascular amyloid peptide. Neurosci Res Commun *2*, 121-130.

Koran, M.E.I., Wagener, M., Hohman, T.J., and Alzheimer's Neuroimaging, I. (2017). Sex differences in the association between AD biomarkers and cognitive decline. Brain Imaging Behav *11*, 205-213.

Kosel, F., Torres Munoz, P., Yang, J.R., Wong, A.A., and Franklin, T.B. (2019). Age-related changes in social behaviours in the 5xFAD mouse model of Alzheimer's disease. Behav Brain Res *362*, 160-172.

Lin, X., Amalraj, M., Blanton, C., Avila, B., Holmes, T.C., Nitz, D.A., and Xu, X. (2021). Noncanonical projections to the hippocampal CA3 regulate spatial learning and memory by modulating the feedforward hippocampal trisynaptic pathway. PLoS Biol *19*, e3001127.
Mathys, H., Davila-Velderrain, J., Peng, Z., Gao, F., Mohammadi, S., Young, J.Z., Menon, M., He, L., Abdurrob, F., Jiang, X.*, et al.* (2019). Single-cell transcriptomic analysis of Alzheimer's disease. Nature *570*, 332-337.
Miyamichi, K., Shlomai-Fuchs, Y., Shu, M., Weissbourd, B.C., Luo, L., and Mizrahi, A. (2013). Dissecting local circuits: parvalbumin interneurons underlie broad feedback control of olfactory bulb output. Neuron *80*, 1232-1245.
Nebel, R.A., Aggarwal, N.T., Barnes, L.L., Gallagher, A., Goldstein, J.M., Kantarci, K., Mallampalli, M.P., Mormino, E.C., Scott, L., Yu, W.H.*, et al.* (2018). Understanding the impact of sex and gender in Alzheimer's disease: A call to action. Alzheimers Dement *14*, 1171-1183.
O'Mara, S. (2005). The subiculum: what it does, what it might do, and what neuroanatomy has yet to tell us. J Anat *207*, 271-282.
Oakley, H., Cole, S.L., Logan, S., Maus, E., Shao, P., Craft, J., Guillozet-Bongaarts, A., Ohno, M., Disterhoft, J., Van Eldik, L.*, et al.* (2006). Intraneuronal beta-amyloid aggregates, neurodegeneration, and neuron loss in transgenic mice with five familial Alzheimer's disease mutations: potential factors in amyloid plaque formation. J Neurosci *26*, 10129-10140.
Oh, S.W., Harris, J.A., Ng, L., Winslow, B., Cain, N., Mihalas, S., Wang, Q., Lau, C., Kuan, L., Henry, A.M.*, et al.* (2014). A mesoscale connectome of the mouse brain. Nature *508*, 207-214.
Paxinos, G.F., K. B. J. (2008). The Mouse Brain in Stereotaxic Coordinates (Academic Press).
Seshadri, S., Wolf, P.A., Beiser, A., Au, R., McNulty, K., White, R., and D'Agostino, R.B. (1997). Lifetime risk of dementia and Alzheimer's disease. The impact of mortality on risk estimates in the Framingham Study. Neurology *49*, 1498-1504.
Sun, Y., Jin, S., Lin, X., Chen, L., Qiao, X., Jiang, L., Zhou, P., Johnston, K.G., Golshani, P., Nie, Q.*, et al.* (2019). CA1-projecting subiculum neurons facilitate object-place learning. Nature neuroscience *22*, 1857-1870.
Sun, Y., Nguyen, A.Q., Nguyen, J.P., Le, L., Saur, D., Choi, J., Callaway, E.M., and Xu, X. (2014). Cell-type-specific circuit connectivity of hippocampal CA1 revealed through Cre-dependent rabies tracing. Cell reports *7*, 269-280.
Tao, S., Wang, Y., Peng, J., Zhao, Y., He, X., Yu, X., Liu, Q., Jin, S., and Xu, F. (2021). Whole-Brain Mapping the Direct Inputs of Dorsal and Ventral CA1 Projection Neurons. Front Neural Circuits *15*, 643230.
Winnubst, J., Bas, E., Ferreira, T.A., Wu, Z., Economo, M.N., Edson, P., Arthur, B.J., Bruns, C., Rokicki, K., Schauder, D.*, et al.* (2019). Reconstruction of 1,000 Projection Neurons Reveals New Cell Types and Organization of Long-Range Connectivity in the Mouse Brain. Cell *179*, 268-281 e213.
Xu, X., Holmes, T.C., Luo, M.H., Beier, K.T., Horwitz, G.D., Zhao, F., Zeng, W., Hui, M., Semler, B.L., and Sandri-Goldin, R.M. (2020). Viral Vectors for Neural Circuit Mapping and Recent Advances in Trans-synaptic Anterograde Tracers. Neuron *107*, 1029-1047.
Xu, X., Sun, Y., Holmes, T.C., and Lopez, A.J. (2016). Noncanonical connections between the subiculum and hippocampal CA1. J Comp Neurol *524*, 3666-3673.
Ye, Q., Gast, G., Su, X., Saito, T., Saido, T.C., Holmes, T.C., and Xu, X. (2022). Hippocampal neural circuit connectivity alterations in an Alzheimer's disease mouse model revealed by monosynaptic rabies virus tracing. Neurobiol Dis *172*, 105820.
Yu, Z., Guindani, M., Grieco, S.F., Chen, L., Holmes, T.C., and Xu, X. (2022). Beyond t test and ANOVA: applications of mixed-effects models for more rigorous statistical analysis in neuroscience research. Neuron *110*, 21-35.
Zhang, H., Chen, L., Johnston, K.G., Crapser, J., Green, K.N., Ha, N.M., Tenner, A.J., Holmes, T.C., Nitz, D.A., and Xu, X. (2023). Degenerate mapping of environmental location presages

deficits in object-location encoding and memory in the 5xFAD mouse model for Alzheimer's disease. Neurobiol Dis *176*, 105939.
Zhu, D., Montagne, A., and Zhao, Z. (2021). Alzheimer's pathogenic mechanisms and underlying sex difference. Cell Mol Life Sci *78*, 4907-4920.

Chapter 4: Summary and Conclusions

In this dissertation work, I review the advancement of neural circuit tracers in Chapter 1, and conduct a series of rabies tracing to map the neural circuit connections of hippocampal CA1 and SUB in AD mouse models for the studies reported in Chapters 2 and 3. My experimental findings reveal that compared to the age-matched control mice, the CA1 excitatory circuit connectivity is altered in AD model mice (Ye et al., 2022), with sex-specific characteristics which are an important feature of human AD. Specifically, in Chapter 2, we assessed the circuit connectivity in AD model mice - amyloid precursor protein knock-in mice (APP-KI) and their age-matched littermate controls at two life stages (3-4 vs. 10-11 months old) as AD is a progressive neurodegenerative disease. We quantitatively mapped the connectivity strengths of neural circuit inputs to hippocampal CA1 excitatory neurons from brain regions including hippocampal subregions, medial septum and diagonal band, subiculum, and entorhinal cortex, comparing different age groups and genotypes. We use a combination of AAV helper viruses for targeted gene expression in CA1 excitatory neurons. The AAV helper injections were followed by pseudotyped rabies virus injection. After extensive histological processing and data quantification, our results indicate that the connectivity of the CA1 circuit in the hippocampus is disrupted in AD model mice in an age-progressive manner. We find weaker extrinsic connectivity CA1 input strengths in AD model mice compared with control mice, including sex differences of reduced subiculum to CA1 inputs in aged female AD mice compared to aged male AD mice. Surprisingly, we discovered a connectivity pattern shift with an increased proportion of inputs from the CA3 region to CA1 excitatory neurons when comparing young and old AD model mice, as well as old wild-type mice and old AD model mice. These unexpected shifts in the proportion of CA3-CA1 inputs in this AD mouse model suggest the possibility that compensatory circuit increases may occur in response to connectivity losses elsewhere within the hippocampal circuits. This work sheds new light on the underlying neural circuit mechanisms of AD pathogenesis.

The SUB is among the earliest brain regions impacted by AD (Carlesimo et al., 2015; Good et al., 2004). In Chapter 3, we employ monosynaptic rabies tracing to map the synaptic circuit inputs to the dorsal subiculum (dSUB) excitatory neurons in the 5xFAD AD mouse model (Ye et al., 2024). To characterize how the circuits are altered in AD, we mapped synaptic circuit inputs to dorsal SUB in the 5xFAD AD mouse model. We quantitatively compare the circuit connectivity of SUB excitatory neurons across age-matched controls and 5xFAD mice of both genders at two ages. Input-mapped brain regions include hippocampal subregions (CA1, CA2, CA3), medial septum and diagonal band (MS-DB), retrosplenial cortex (RSC), SUB, post subiculum (postSUB), visual cortex (Vis), auditory cortex (Aud), somatosensory cortex (SS), entorhinal cortex (EC), thalamus, perirhinal cortex (Prh), ectorhinal cortex (Ect) and temporal association cortex (TeA).

We find striking sex- and age-dependent changes in connectivity strengths and patterns of SUB presynaptic inputs from hippocampal subregions and other brain regions in 5xFAD mice compared to control mice. In human patients, women are at a higher risk of developing AD than men due to a range of factors including longevity, hormonal level, genetics, inflammation, and various sociocultural factors (Nebel et al., 2018; Zhu et al., 2021). Although the precise mechanism underlying these sex differences remains unclear, research indicates that the association between AD pathology and clinical AD was substantially stronger in women than in men (Barnes et al., 2005). Our sex-specific comparison shows that there is a sex difference of reduced subiculum to CA1 inputs in aged female AD mice compared to aged male AD mice. Notably, we also identified significant sex-specific differences in SUB inputs within the 5xFAD mice, particularly in areas critical for learning and memory, such as CA1, CA2, CA3, postSUB, Prh, LEC and the MEC.

Intriguingly, our circuit mapping approach informs understudied aspects beyond learning and memory. My study reveals significant age-dependent alterations in visual cortical inputs to

the SUB. While visual function is not ordinarily considered defective in AD, our results show that young 5xFAD mice exhibit enhanced connectivity from the visual cortex to the SUB compared to WT mice, whereas in middle-aged 5xFAD mice this phenomenon was inversely shifted. This observation is in line with the growing understanding that AD initiates with neuronal hyperexcitability, which then gradually transitions to hypo-excitability in its advanced stages. While the visual cortex is traditionally overlooked in AD research, it is now being recognized for its potential role during disease progression. These specific connectivity changes reflect altered visual circuitry contributing to learning and memory deficits. Our circuit mapping approach informs understudied aspects beyond learning and memory.

In conclusion, my dissertation work supports a circuit-level perspective on AD disease mechanisms and demonstrates how neuronal circuit alterations can be unraveled in AD mouse models with new viral genetic tracing techniques. These advanced methods enable precise targeting of specific cell types and projection pathways. Our investigations have leveraged the monosynaptic rabies virus tracing to quantitatively map the input connections of hippocampal CA1 and SUB regions; both brain regions are critically impacted in AD. I believe that the newly developed technological and conceptual advances may represent the beginning of a new direction for large-scale neural circuit-based AD research.

References

Barnes, L.L., Wilson, R.S., Bienias, J.L., Schneider, J.A., Evans, D.A., and Bennett, D.A. (2005). Sex differences in the clinical manifestations of Alzheimer disease pathology. Arch Gen Psychiatry *62*, 685-691.

Carlesimo, G.A., Piras, F., Orfei, M.D., Iorio, M., Caltagirone, C., and Spalletta, G. (2015). Atrophy of presubiculum and subiculum is the earliest hippocampal anatomical marker of Alzheimer's disease. Alzheimers Dement (Amst) *1*, 24-32.

Good, P.F., Alapat, D., Hsu, A., Chu, C., Perl, D., Wen, X., Burstein, D.E., and Kohtz, D.S. (2004). A role for semaphorin 3A signaling in the degeneration of hippocampal neurons during Alzheimer's disease. J Neurochem *91*, 716-736.

Nebel, R.A., Aggarwal, N.T., Barnes, L.L., Gallagher, A., Goldstein, J.M., Kantarci, K., Mallampalli, M.P., Mormino, E.C., Scott, L., Yu, W.H.*, et al.* (2018). Understanding the impact of sex and gender in Alzheimer's disease: A call to action. Alzheimers Dement *14*, 1171-1183.

Ye, Q., Gast, G., Su, X., Saito, T., Saido, T.C., Holmes, T.C., and Xu, X. (2022). Hippocampal neural circuit connectivity alterations in an Alzheimer's disease mouse model revealed by monosynaptic rabies virus tracing. Neurobiol Dis *172*, 105820.

Ye, Q., Gast, G., Wilfley, E.G., Huynh, H., Hays, C., Holmes, T.C., and Xu, X. (2024). Monosynaptic rabies tracing reveals sex- and age-dependent dorsal subiculum connectivity alterations in an Alzheimer's disease mouse model. The Journal of neuroscience : the official journal of the Society for Neuroscience.

Zhu, D., Montagne, A., and Zhao, Z. (2021). Alzheimer's pathogenic mechanisms and underlying sex difference. Cell Mol Life Sci *78*, 4907-4920.